Exploring the Influence of pH and Metal Zinc(II) Ion Trends on Interactions Amongst Amyloid-β and Amylin Peptides

Oneeb Jilani

A thesis submitted for the degree of

Master of Philosophy

Cardiff University

12/2025

ACKNOWLEDGEMENTS

Firstly, I would like to express my gratitude to Dr. Jamie Platts for his patience, support, and advice for the duration of my master's degree. His knowledgeable guidance and mentorship have been imperative in allowing me to reach this stage of my research, and for that I am immensely grateful. I would also like to thank Thuraya Alhabradi, who made my transition into MPhil an easy venture and for her continued guidance during my first year. To Jiaming Chen, I thank you for supporting me as both a peer and a friend. Your continued friendship has made this year a joy.

I would also like to thank the ARCCA staff for access to the supercomputing facilities and their technical support. Special thanks to the people of the PGR and Chem-Safety Office for their insightful chats and for creating an inclusive, enjoyable environment for research. I must also thank Cardiff University for allowing me to pursue this chance to pursue my ideas in the form of my research and my thesis.

Finally, I must also acknowledge my father, Asim, and mother, Fariya, for encouraging me and giving me the push needed to pursue this degree. You have shaped my whole path to where I am today, and I cannot thank you enough. I dedicate this work to my grandfather, who provided the template of success for myself and my parents to pursue higher education. This work, as well as my entire education, would not have been a possible without them and for that I am eternally grateful.

Abstract

The tendency of Aβ to self-assemble into β-rich aggregates is central to the pathology of Alzheimer's disease. This thesis uses constant-pH molecular dynamics to investigate how protonation equilibria, electrostatics, and zinc coordination jointly influence the structure and oligomerization of Aβ40, amylin, and their mixed assemblies under near-physiological conditions at the nucleation stage. Testing upon a truncated Aβ16 fragment helped validate the implicit-solvent CpHMD approach and identified the pH conditions under which its behaviour best mimics that of full-length Aβ40. Extending the simulations to Aβ40 and amylin monomers at pH 6–8 showed that partial histidine protonation stabilises compact, β-enriched conformations in Aβ40, whereas amylin remains more conformationally flexible and predominantly helix/turn-rich, with both peptides retaining signatures of intrinsic disorder. Building upon this, large ensembles of dimers and trimers were generated for Aβ40 homomers - which consistently formed more β-structured and compact interfaces, and amylin homomers - which adopted semi-ordered but more flexible architectures. Mixed Aβ–amylin dimers adopted the structural patterns of the leading peptide i.e Aβ–led oligomers had greater β sheets and vice versa. The heterodimers produced cooperative but poor intermediates, in which amylin dampens excessive β-structuring by Aβ, whereas trimeric assemblies marked the first point at which consistent, aggregation-competent β-core architectures appeared, largely independent of initial peptide orientation. Finally, Zn(II) coordination was examined in Aβ40 homodimers – to validate native-like compactness and β-content of unprotonated structures, particularly near His13 and Aβ40–amylin heterodimers – to highlight changes in local protonation and charge distribution, weakening β-sheets and favouring more helical, moderately flexible conformations, particularly in dual-metal systems. These results indicate that early Aβ–amylin co-aggregation, and its modulation by Zn(II), is controlled by a subtle balance between protonation state, electrostatics, and metal coordination, providing atomistic insight into the earliest nucleation events that link Alzheimer's disease with metabolic dysfunction.

CONTENTS

Chapter 1: Introduction

1.1 Overview

The aim of this thesis is to investigate how pH levels affect the structure and aggregation capabilities of two peptides involved in Alzheimer's Disease (AD), Amyloid-β 40 (Aβ40) and amylin. Amylin proteins can form dimers with Aβ40 either through co-aggregation or cross-seeding mechanisms. Hence, the literature review in this chapter will be on three main areas of research; namely, the structural and pathological role of Aβ40 and amylin in AD, the influence of pH variance on peptide folding and the methodology by which to study it computationally, and the modulatory effects of Zn(II) ions on the structure and folding propensity of Aβ40 and amylin conformations. In summary, our study will use conventional molecular dynamics (MD) and quantitative, classical molecular simulation-based analyses to investigate how environmental factors modulate the aggregation propensity of the peptides, thereby contributing to their pathological role in Alzheimer's Disease.

1.2 Alzheimer's Disease

AD is the most common form of dementia, a progressive neurodegenerative disorder primarily affecting the elderly aged 65 and above, with over 900,000 cases every year globally (1–6). It is characterized by a gradual decline in memory, personality, cognitive functions and physical abilities (7,8), and a gradual increase of amyloid plaques and neurofibrillary tangles (hyperphosphorylated tau tangles) in the brain until a patient's death (9). It was first described by Alois Alzheimer in his 1907 article: "On an Unusual Illness of the Cerebral Cortex," from his 4.5-year observation of a 51-year-old dementia patient (4). Soon after, the link between Alzheimer's and amyloid-β protein (Aβ) was established in Masters *et al.*(10), which also led to subsequent analysis and discoveries regarding the aetiology of this disease. Though the causes are not clearly understood, several contributing factors are well-known, chief amongst them being age, due to an accumulation of cytotoxic forms of Aβ deposits over the course of a lifetime (12). Other factors include; high blood pressure, smoking (13–15), cholesterol (16,17), alcohol consumption (18) and genetic mutations in amyloid precursor proteins (APP), a type I transmembrane glycoprotein (19), which can also cause early onset AD. Additionally, obesity linked with a poor diet and diabetes (20–22) is known to increase the likelihood of AD, with

emerging evidence suggesting a close link between Alzheimer's and Type II diabetes mellitus (T2D).

Recent studies have demonstrated the involvement of amylin (also known as islet amyloid polypeptide, or amylin), a hormone typically found in the pancreas and bloodstream of T2D patients and known for its amyloidogenic properties, in the brain of AD patients. (23). The formation of toxic Aβ and its extracellular build-up is associated with cell death, as described in the amyloid hypothesis (24). There is reported evidence to suggest an association between the increase in amylin expression during AD, and the secretion of Aβ (25). Both proteins can readily misfold, engaging in cross-seeding and have shown to co-aggregate into toxic amyloid fibrils (26). The presence of amylin in the AD brain and its interaction with Aβ highlights a shared amyloidogenic pathway, suggesting that metabolic dysfunction, such as that seen in T2D, may contribute to AD pathogenesis.

1.3 Amyloid-β Cascade Hypothesis

First proposed in early 1990's, the amyloid cascade hypothesis is the current best model for molecular aetiology for AD. It postulates that the abnormal accumulation and aggregation of amyloid-β is an upstream trigger. This initiates a cascade of neurotoxic events, ultimately leading to synaptic dysfunction, neurodegeneration and clinical presentation of AD (27–29).

Aβ is a 39-43 residue amyloidogenic peptide, produced through proteolytic processing of APP, a neuronal type I transmembrane glycoprotein, with roles in synaptic plasticity, neural development, and metal ion homeostasis. APP can be processed through two main pathways: amyloidogenic and non-amyloidogenic. In the latter, α-secretase cleaves within the Aβ domain producing a membrane bound C-terminal fragment (CTF83). Further cleavage by γ-secretase on the CTF83 produces p3 fragments – truncated 17-40/42 residue forms of Aβ. In the former pathway, β-secretase and γ-secretase sequentially cleave the Aβ peptides producing first CTF99 and later full-length amyloid-β proteins, of which 40- or 42-residue lengths are the dominant species (30–32). While these structures are not toxic as monomers at levels ~0.1/~1 nM for Aβ42/Aβ40, elevation of these levels to tens of nanomolar greater and membrane-detachment of Aβ can lead to cytotoxicity which in turn can lead to AD.

The soluble Aβ40 is produced in greater abundance than Aβ42. However, Aβ42 displays a higher tendency for aggregation due to the hydrophobicity of its two terminal residues (Ile41 and Ala42) as highlighted in Figure 1.1. Aβ is amphiphilic; the first 16 residues make up the hydrophilic N-terminal region, while the later 21-30 residues make the central hydrophobic region. Metal ions like Zn(II) can modulate oligomerization by interacting with the N-terminal region and altering peptide solubility, cross-linking, and conformational states (33,34). It can alter the pathway of amyloid by inhibiting fibril growth and favouring oligomer accumulation. Meanwhile, the central region acts as the aggregation core, favouring hydrophobic collapse and β-rich fibril formation, displayed in Figure 1.1. Furthermore, high-resolution NMR and circular dichroism (CD) studies showcase how the monomeric Aβ exists not as a single structure but as a heterogeneous ensemble with ~5–20% α-helix content, 0–25% β-sheet content, and the remainder existing in random coils (35,36). Within this ensemble, the central hydrophobic region frequently adopts an extended 3_{10}-helix conformation. Aβ's helices and coils, due to their extended formations can rearrange into β-sheets for greater stability and allow aggregation with molecules and ions like amylin and Zn(II) respectively, as discussed further below.

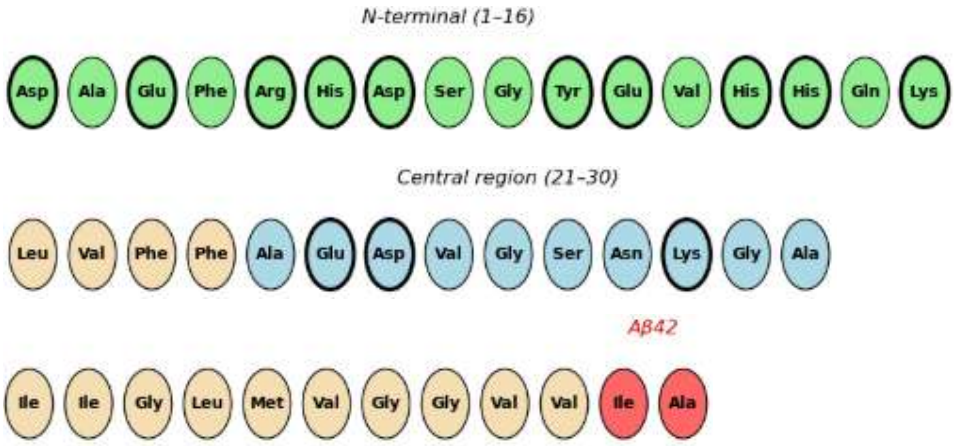

Figure 1.1. Amino acid sequence of Aβ40 separated into N-terminal and Central regions and C-terminal regions with the additive Aβ42 residues highlighted in red and titratable residues in bold outlines.

Although Alzheimer's disease pathology is often discussed in relation to hippocampal vulnerability, Aβ deposition is observed broadly across cortical regions. Aβ is particularly detected in environments rich in transition metal ions like zinc, iron

and copper. In AD, fast amyloid proliferation can quickly spread through the rest of the cerebral regions of the brain possibly contributing to progressive neuronal dysfunction and loss (37–42).

The amyloidogenic cascade highlights how accumulation of Aβ deposits is affected by the rate of nucleation of soluble oligomers. These can form proto-fibrils and interact with other oligomers to eventually mature into fibrils that can deposit extracellularly as insoluble protein plaques (10,43–47). Protofibrils can bind to oligomers and further increase the aggregation pathway producing mature fibrils. In parallel, the tauopathy pathway, shows intracellular accumulation of hyper-phosphorylated protein tau in neurofibrillary tangles (NFT), which are involved in intracellular transport and microtubule stability (48). In AD, Tau pathology can contribute to synaptic failure and neuronal death by destabilizing the microtubule network (40,49).

These two pathways are often described as synergistic. Aβ accumulation is associated with upstream oxidative stress, which may activate kinases and/or reduce phosphatase activity in ways that could contribute to tau hyperphosphorylation. In turn, tauopathy involves downstream proteins accompanying axonal transport impairment, including vesicle trafficking that carry APP or APP-processing enzymes, which may shift APP handling towards a more amyloidogenic processing (2,50). Tauopathy products are also linked with additional oxidative stress and cellular vulnerable, which could increase susceptibility to Aβ-mediated toxicity and potentially creating a reinforcing cycle that favours further Aβ aggregation. These pathways are highlighted in Figure 1.2.

Although the plaques are the most visible pathological hallmark of AD, the plaque burden tends to show only a weak correlation with cognitive decline in many studies (51,52). Some individuals can remain cognitively intact despite having high deposits of Aβ in the brain (53–55). By contrast, soluble cytotoxic Aβ oligomers are more consistently associated with synaptic dysfunction and cognitive impairment than fibrillar plaque load (56,57). These oligomers have been reported to disrupt synaptic plasticity, alter ion homeostasis and trigger or amplify inflammatory and oxidative stress responses in surrounding neurons (28,58–61).

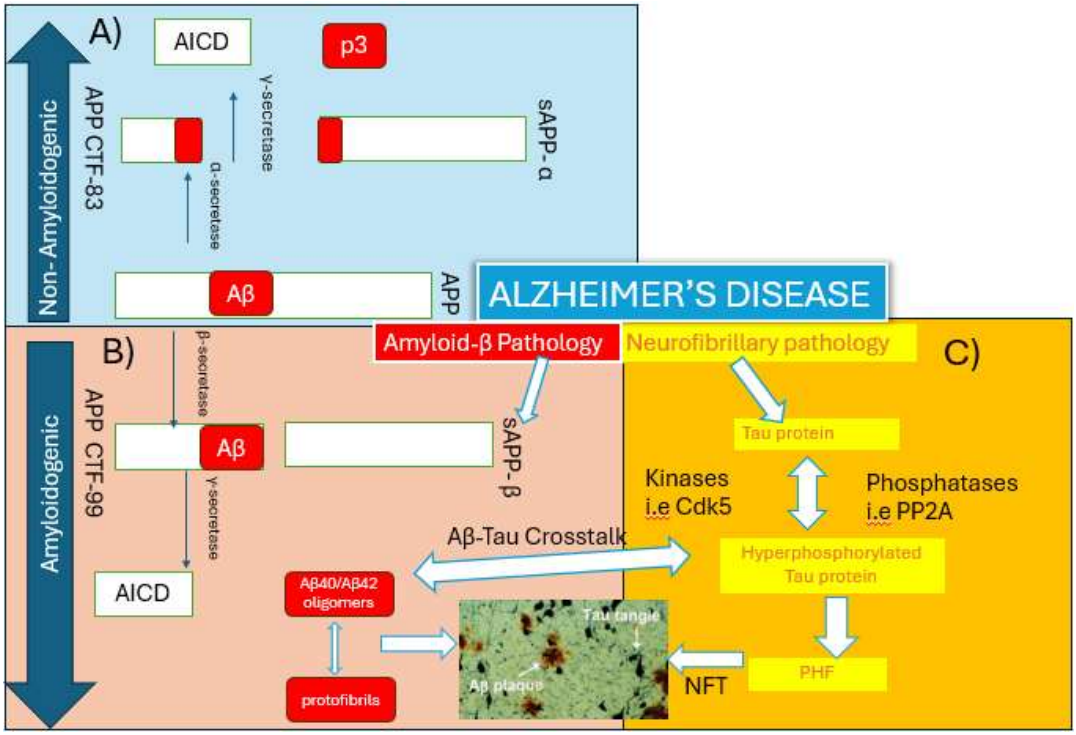

Figure 1.2 A representative diagram of **A-B)** cleavage dependant processing pathways of APP and **C)** Alzheimer's Disease pathology pathway for Neurofibrillary Tangles. Processing amyloid Precursor Protein (APP) by secretases can lead to the formation of Alzheimer's-associated Aβ peptides. **A)** In the non-amyloidogenic pathway, APP is cleaved by α- and γ-secretases leading to the genesis of p3 and APP Intracellular Domain (AICD). **B)** amyloidogenic pathway contributes to AD. APP is cleaved by β- and γ-secretases leading to the formation of Aβ peptides (40/42) and AICD. High enough concentration of Aβ either bound amongst themselves, with amylin, or with membranes may contribute to neurotoxicity associated with AD. **C)** In the tauopathy pathway, dysregulation of tau phosphorylation can lead to hyperphosphorylated tau mis-localizing and forming filamentous aggregate instead of stabilizing microtubules. These aggregates ultimately accumulate into neurofibrillary tangles (NFTs) and can interact with Aβ oligomers to exacerbate synaptic and memory dysfunction contributing to Alzheimer's Disease. APP, amyloid precursor protein; sAPPα, Soluble APP alpha; sAPPβ, Soluble APP beta; αCTF 83, Alpha C-terminal fragment 83; βCTF 99, Beta C-terminal fragment 99; AICD, APP intracellular domain. NFT; Neurofibrillary Tangles, CDK5; Cyclin-dependent kinase 5, PP2A; Protein Phosphatase 2A, PHF; Paired Helical Filaments.

The aggregational propensity of Aβ is closely linked to secondary structure transitions during self-association. In the initial stages, monomeric Aβ samples a largely disordered coil ensemble (62,63). A subset of these molecules adopts β-sheet conformations that can nucleate assembly, while other populations can form

less ordered, amorphous oligomeric species (64–66). The central aggregation hotspot can see the transient and pH dependant at Aspartate on position 23 – Lysine on position 28 (Asp23-Lys28) salt bridge help stabilize the turn/bend region (~23-29) which supports the hairpin topology that favours β-sheet alignment and supports inter-chain hydrogen bonding during nucleation. As fibrils elongate, cross-β structure increases and thioflavin T (ThT) fluorescence rises as a byproduct of Tht binding preferentially to β-sheet rich fibrillar grooves. This signal approaches a plateau once fibril growth slows or reactive monomers become depleted (36).

Beyond Aβ self-assembly, amyloid deposition in Alzheimer's disease may also be influenced by islet amyloid islet amyloid polypeptide, which aggregates in the pancreas of individuals with T2D. Increasing evidence suggests a cross-seeding mechanism, where amylin and Aβ –share partial sequence/structural homology – promote the formation of mixed amyloid aggregates (67). Amylin expression has also been detected in the brains of AD patients and experimental exposure of amylin to amyloid in neuronal cultures has indicated varying degrees of secretion in Aβ, indicating a possible bi-directional pathogenic relationship between metabolic dysfunction and amyloid pathology (68).

1.4 Amylin Oligomers

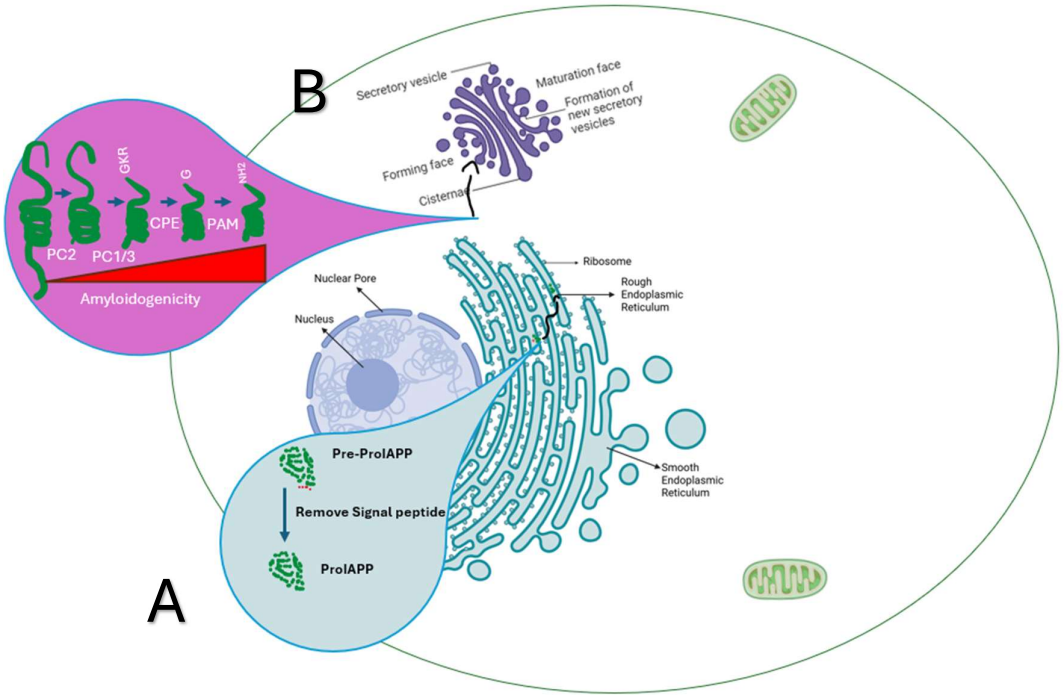

Figure 1.3 A representative diagram **(A-B)** of the human amylin (IAPP) biosynthesis and maturation pathway. **A)** Amylin is synthesized as an 89-residue preproIAPP containing a 20 residue N-terminal signal peptide. Co-translational translocation into the rough endoplasmic reticulum (RER) is followed by signal peptide cleavage, generating the 69-residue proIAPP. Disulfide bond formation between Cys2 and Cys7 occurs in the oxidizing ER environment. **B)** In acidified immature granules, proIAPP undergoes endoproteolytic cleavage at dibasic sites (Lys12′–Arg13′ and Lys52′–Arg53′) primarily by prohormone convertases PC2 and PC1/3. Carboxypeptidase E removes residual Lys–Arg motifs, yielding a Gly38-extended intermediate (amylin free acid). Finally, Peptidylglycine α-amidating monooxygenase (PAM) converts the C-terminal Gly38 intermediate into mature 37-residue, C-terminally amidated amylin (Tyr37–NH_2). Processing occurs via the same enzymatic machinery responsible for proinsulin maturation. PreproIAPP, prepro-islet amyloid polypeptide; proIAPP, pro-islet amyloid polypeptide; PC1/3 and PC2, prohormone convertases; CPE, carboxypeptidase E; PAM, peptidylglycine α-amidating monooxygenase; RER, rough endoplasmic reticulum.

Amylin is a 37-residue neuroendocrine hormone that, under normal physiological conditions, maintains glucose homeostasis and regulates metabolism. It is synthesized as an 89-residue preprohormone. First, the signal peptide is removed in the endoplasmic reticulum to produce proIAPP (69). ProIAPP is then processed in the Golgi by proprotein convertases (PC2 then PC1/3) and carboxypeptidase E (CPE) to yield mature amylin as illustrated in Figure 1.3 (70,71). The final peptide contains a disulfide bond between Cys2 and Cys7 and an amidated C-terminus (70,71). The prohormone amylin is packaged into secretory granules with insulin and is co-secreted after food intake. Together, insulin and amylin support glucose uptake in muscle and adipose tissue, reduce hepatic glucose output and supress nutrient-stimulated glucagon secretion (72). Physiologically, amylin also influences satiety, energy balance, and gastric emptying through its CNS receptors (73,74).

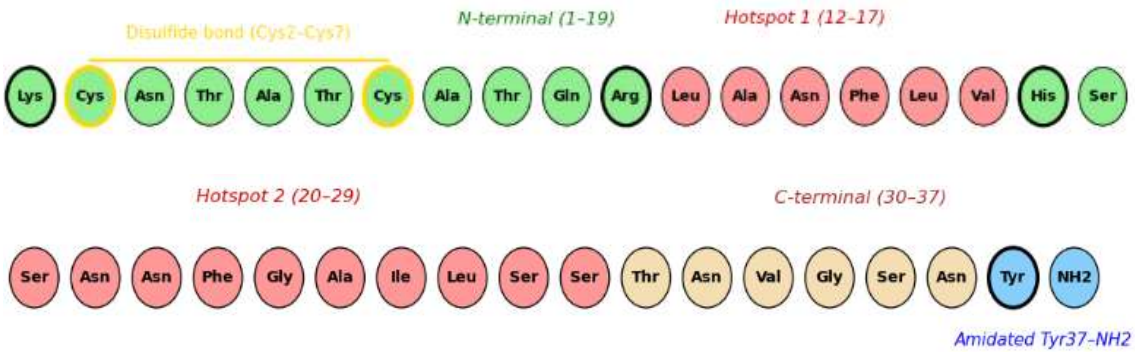

Figure 1.4 Amino acid sequence of human amylin separated into N-terminal and C-terminal regions with a highlighted disulphide bond, amyloidogenic residues in red, amidated C-terminal residues in blue and titratable residues in bold outlines.

Human amylin also has amyloidogenic 'hot spots' in its core at residues 12-17, 20-29, and hydrophobic residues like Phe23 and Ile26 that are associated with β-sheet formation and aggregation promotion (75), as noted in Figure 1.4. The strong amyloidogenicity of human amylin – compared to rodent amylin protein – may be attributed to the lack of stabilizing residues like proline as found in mice amylin proteins which are non-amyloidogenic (76-77). When bound in β-cell secretory granules aggregation is inhibited by the acidic pH of the environment, the presence of insulin, and its state as an intermediary prohormone. After secretion into the bloodstream, it is released as a mature hormone in near-neutral extracellular environments where it can more readily adopt amyloidogenic conformations (78).

In prediabetic and T2DM states, insulin resistance of cells drives hypersecretion, and amylin is secreted alongside it. The increased secretory demand stresses the β-cell processing pathway and can increase intracellular accumulation of proIAPP, which is more prone to misfolding and aggregation (79, 80). Over time, islet amyloid deposits form, impairing normal β-cell function and promoting β-cell loss through toxicity-associated apoptosis (81,82). The islet amyloid is therefore considered a characteristic pathological hallmark of T2DM (83).

Accumulating evidence over the past decade also implicates amylin aggregates in Alzheimer's disease. Notably, amylin is not only produced in the pancreas but can also easily pass the blood–brain barrier (84), where it's shown to directly interact with Aβ through cross-seeding mechanisms (85–87). This cross-amyloid interaction amplifies toxicity by reactive oxygen species production, membrane permeabilization etc. and provides a mechanistic basis for the epidemiological association between type 2 diabetes mellitus (T2DM) and AD. Consistent with this, studies have documented amylin deposition in the brain parenchyma and vasculature, as well as in mixed plaques containing Aβ, findings absent from healthy control tissue (31,88). Evidence from human amylin transgenic rat models further strengthens this connection, as these animals exhibit cerebral amyloid accumulation, neuroinflammatory responses, and cognitive or behavioural impairments (26,89). The coexistence of Aβ–amylin aggregates seen *in vivo* mirrors heterocomplexes is

predicted through sequence analysis and confirmed experimentally (90). Another point of similarity is found in their clearance: both peptides depend on insulin-degrading enzyme (IDE) (91) and neprilysin for extracellular proteolysis (92,93), while intracellularly they are targeted to lysosomal degradation via autophagy (94). Competition for these shared degradation pathways means that excess **amylin** secretion in T2DM can interfere with Aβ clearance, thereby intensifying AD-related pathology. Furthermore, like soluble Aβ, soluble amylin species in plasma are reduced in AD patients (95), potentially reflecting increased deposition in the brain or peripheral tissues, or alternatively decreased secretion linked to undiagnosed diabetes (96). Together, these findings position amylin not only as a hallmark of islet dysfunction but also as a peripheral driver of neurodegeneration, closely paralleling Aβ in aggregation, deposition, and impaired clearance.

1.5 Dimerization of Aβ and amylin

Much of the research has mostly focused on the monomeric “toxic” amyloidogenic peptides (soluble human amylin and Aβ42); however, growing evidence suggests that early oligomeric states including dimers, can themselves be measurably cytotoxic and biologically active. Although Aβ dimers are difficult to isolate due to their tendency to progress rapidly into larger oligomers, they are known to provide the initial parallel β-sheets structure and subsequent fibril nucleation (97,98). Similarly, the human amylin dimer, largely driven by the interactions between their hydrophobic cluster (20-29 residue segment), are thought to act as the central intermediates in the aggregation process. Both peptides appear to maintain a dynamic equilibrium between monomers, dimers, oligomers, and fibrils, with structural studies consistently revealing partial β-sheet content even at the dimer stage evidenced by the *in vivo* and *in vitro* studies (99,100).

For Aβ, dimerization and subsequent growth are driven by several interacting sequence elements rather than a single hotspot. The central hydrophobic cluster (Ala21–Ala30), additional contacts spanning LVFFA (17-21), the C-terminal hydrophobic stretch (31-42), and even the N-terminal metal-binding residues (Glu11, His13/14) can contribute to the stabilization of interchain packing and promote assembly (101-104). Structural studies using solid-state NMR highlight a difference between Aβ fibrils. The studies suggests that Aβ40 adopts an architecture built from dimeric units arranged in multi-layer β-sheets, where each monomer contributes two

β-strands segments (His13–Asp23 and Lys28–Val40) connected a turn that can be further stabilized by Asp23–Lys28 interactions. Internal contacts stabilize each molecular layer, while external contacts link adjacent sheets. Aβ42 shares broad architectural features but can adopt S-shaped or twisted β-sheet structures rather than U-shaped ones, and different polymorphs (tubular, hollow, helical β-sheets) through the transient α-sheet motifs, likely due to its additional Ile41 and Ala42 residues which enhance aggregation and toxicity (105–107).

The aggregation-prone segment of human amylin, thought to exist within the strongly conserved amyloidogenic region of 20–29 residues, is critical for fibril nucleation (108,109). Like Aβ, human amylin fibrils maintain a *β-strand – loop – β-strand* motif, in which residues 8–17 and 28–37 form β-strands flanking a loop at residues 18–27 (110,111). This arrangement provides the parallel β-sheets, stabilized by the aromatic residues such as F15 in the fibril core, F23 in the loop, and Y37 exposed in the C-terminus (112).

To reiterate, the human amylin and Aβ share substantial sequence and structural similarity (reported at ~50% overall, with the strongest homology in β-structure–forming regions), which helps explain why they can cross-assemble into heterodimers and higher hetero-oligomers (113). Although the precise morphology, size distribution, and neurotoxicity of Aβ–Amylin heterocomplexes remain incompletely understood, an understanding of their structure has been made using molecular dynamic (MD) simulations and crystallographic or spectroscopic approaches such as cryo-EM, solid-state NMR, and X-ray diffraction (114). The heterodimeric and oligomeric interactions arise early in the co-aggregation process and can be related to a few “hotspots” that drive their association. Though exact registries vary, multiple molecular dynamic studies have showcased that when bound in a heterodimer complex, Aβ residues 3-6 at the N-terminus, 15-22 within the central hydrophobic core, and 31-41 at the C-terminus display high β-sheet propensity, while the amylin aggregation-prone segments span the N-terminal region of residues 10-16 and central region with 20–29. It is within these regions that span of 5 or 6 residues facilitates hybrid strand-loop-strand complex formation, with inter-peptide hydrogen bonding locking the two chains into a cross-β–like architecture. Furthermore, there are indications of binding causing partial unfolding of the helical stretch encompassing Aβ residues 16–22, thereby exposing this core amyloidogenic

region and accelerating β-sheet conversion. Additional evidence points to membrane-associated interactions further stabilizing heterodimeric and oligomeric structures. Collectively, these findings suggest that the Aβ–human amylin heterodimer is stabilized by complementary contacts in both N- and C-terminal regions as well as by central hydrophobic motifs, adopting a β-strand–rich architecture that not only seeds cross-aggregation but also contributes to the elevated cytotoxicity observed in Alzheimer's disease and type 2 diabetes comorbidity (112).

1.6 pH Impact on amylin and amyloid β oligomers

The pH of an environment can dictate the ionization states of titratable residues, alter electrostatic interactions, and reshape protein conformational ensembles. While the interstitial fluid is typically close to neutral pH, processes associated with ageing, inflammation, and oxidative stress in AD have been linked to localized acidification as illustrated in Figure 1.5 (115, 116). The small pH changes, combined with the protonation equilibria of titratable residues in both amylin and Aβ, changes their aggregation propensity.

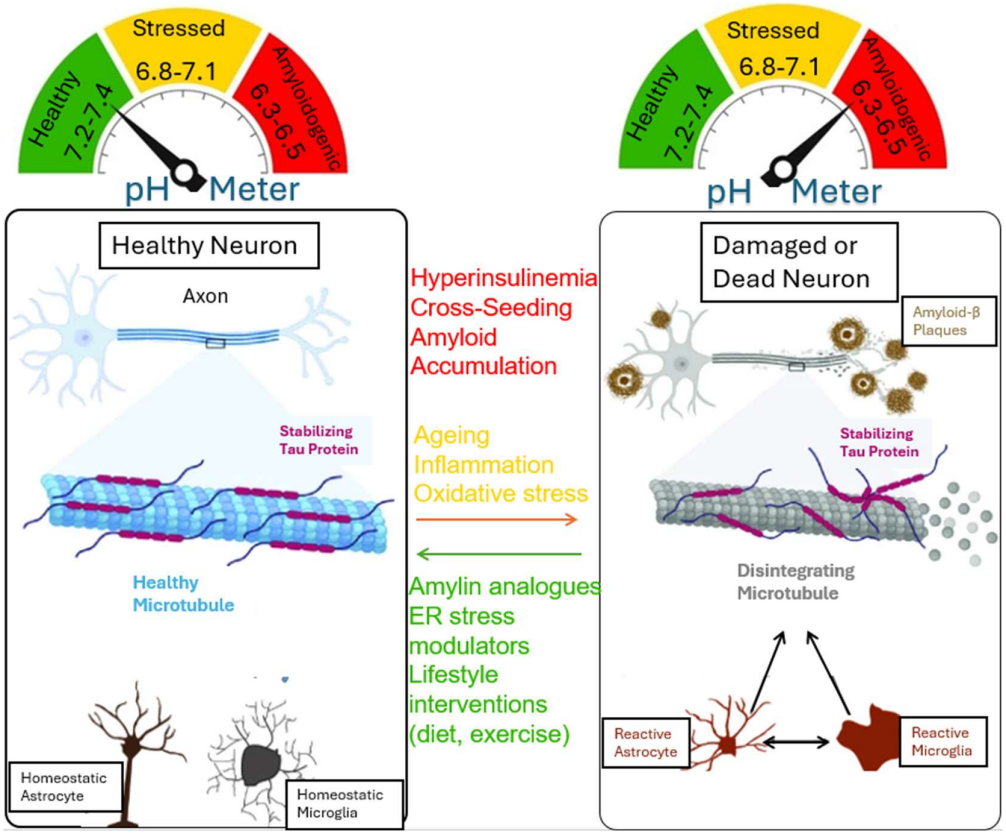

Figure 1.5 Schematic diagram of the pH impacting factors in Healthy vs. AD Brian. The factors are listed in various colours representative of the impact they have on the pH of the Brain.

For amylin, His18 is a key titratable residue within the amyloidogenic region and is widely considered an important contributor to pH-dependent behaviour. In acidic β-cell secretory granules (around pH 5.5), high Zn(II) concentration, insulin co-packaging, and the overall charge state of amylin are thought to disfavour β-sheet formation and reduce fibrillization, consistent with models where increased net positive charge enhances inter-monomer electrostatic repulsion and disrupts productive packing (117). Under near-neutral conditions, reduced protonation at His18 and shifts in net charge can lessen electrostatic penalties and change how Zn(II) coordinates the peptide; together this can make it easier for stabilizing intramolecular and interfacial contacts – such as hydrogen bonding and aromatic packing involving residues like Phe15 and Phe23 – to form, which is consistent with a greater tendency to progress toward β-structure in experimental and computational studies (56). Importantly, this should be framed as biasing the conformational ensemble and interaction landscape, rather than deterministically switching aggregation “on” or “off.”

For Aβ, the net charge near physiological pH is typically negative (often approximated as ~-3 for Aβ40), reflecting contributions from acidic residues (e.g., Asp1, Glu3, Asp7, Glu11, Glu22, Asp23) partially offset by basic residues (e.g., Arg5, Lys16, Lys28). The three histidines (His6, His13, His14) are of particular interest because modelling studies insinuate that their protonation states can change over the pH 6-8 window, and their microenvironment can shift their effective pKa (118,119). As a result, pH is expected to influence early association steps by altering charge distribution and the balance of salt-bridges, cation–π interactions, and solvation at the interface. Consistent with this, Tian *&* Viles report that the primary nucleation step is relatively pH-sensitive with a midpoint near pKa 6.8-7.0 – compatible with histidine protonation – whereas elongation and secondary nucleation are comparatively less sensitive. This implies that small decreases in local pH could shift the balance of nucleation pathways and impact downstream fibril morphology, rather than uniformly accelerating aggregation in all contexts.

Although there is experimental evidence for crosstalk between amylin and Aβ – including cross-seeding and mixed deposits in AD tissue – there is still limited mechanistic understanding of how pH shapes the earliest hetero-assembly events (69,120,121). One plausible hypothesis is that changes in local pH could create charge states that reduce solubility, alter interfacial complementarity, or increase exposure of aggregation-prone segments, thereby facilitating heterodimer formation under certain conditions; however, this remains to be tested directly. Overall, while individual pH-dependent behaviours of each peptide are increasingly well characterized, the first nucleation-stage steps of amylin-Aβ heterodimerization are not, and addressing this gap may clarify whether pH shifts tend to promote or suppress early cross-assembly and help interpret the epidemiological association between T2DM and AD.

1.7 Metal ions-peptide interaction in AD

1.7.1 Natural Metal

Transition metals like Zinc (Zn(II)), Copper (Cu), or Iron (Fe), play important roles in biological system, particularly through their involvement with proteins and enzymes. Under normal physiological conditions, these metals are tightly regulated; however, disruptions in the homeostasis of biological systems i.e. impaired amyloid precursor protein (APP) regulation, can disturb their concentrations and trigger harmful biological consequences. Copper and iron are particularly important because they are redox-active transition metals, capable of cycling between multiple oxidation states (122). While this property is essential in their roles of neuronal signalling, oxidative stress regulation or cell proliferation it becomes detrimental when they interact with the Aβ or amylin-Aβ heterocomplexes to promote hydroxyl radicals and other ROS that can damages lipids, DNA, and cellular structures (123–126).

In 1975, metals were first recognized to contribute to AD pathology. Lead was detected in the neurofibrillary tangles and senile plaques of the brains affected by AD. Lead itself is not a physiologically required metal: it is neurotoxic, capable of substituting for Ca(II) or Zn(II) in enzymes or proteins. The next metal found in 1981 by Burnet *et al.* to be associated with AD was Zn(II). Since then, aluminium, manganese, copper, and iron amongst others have been found related to either Aβ plaque formation or tau-related pathology. Substantial evidence supports the central

involvement of these transition metals in Alzheimer's disease (AD) (127,128). There is a correlation between their imbalance in the brain and neuronal damage. Another focus of this research would be on the transition metal Zn(II) because of its relative abundance, central involvement in synaptic signalling, and unique ability to drive Aβ aggregation without directly producing ROS unlike iron or copper (129–131).

1.7.1.1 Zn(II) Coordination Chemistry

Unlike iron or copper, Zn(II) is redox-inert, allowing it to perform structural and catalytic roles without directly generating ROS. Its chemical properties enable it to form stable coordination complexes with a variety of ligands, including amino acid side chains of peptides, nucleotides, and small organic molecules, adopting geometries like tetrahedral arrangements as seen in Figure 1.6. These complexes are essential for the function of hundreds of enzymes, transcription factors, signalling proteins, and regulating processes ranging from DNA synthesis to neurotransmission (132).

Zn(II) is highly concentrated in the hippocampus and cortex regions of the CNS where it is stored in synaptic vesicles and released during neuronal activity to modulate synaptic plasticity (133). However, dysregulation of Zn(II) homeostasis can contribute to Alzheimer's disease (AD): excessive build up can lead to Zn(II) ions binding to Aβ, promoting aggregation and plaque formation, while local deficiency at synapses impairs neurotransmission (134). Consequently, Zn(II)'s dual role as both a critical cofactor and a potential pathological driver makes it a central target for research into therapeutic strategies that aim to restore metal balance in neurodegenerative disease.

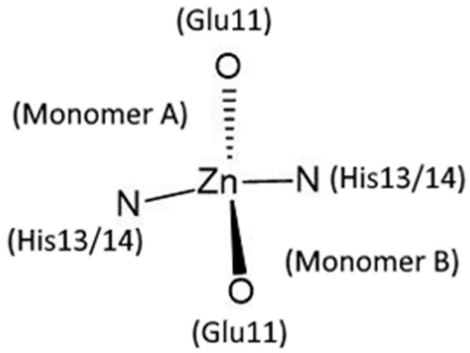

Figure 1.6 Bridging coordination mode of dimeric Zn-Aβ complexes.

1.7.1.2 Zn(II)-Aβ/Amylin Coordination Chemistry and Aggregation

Being a redox-inactive, closed-shell d^{10} transition metal, Zn(II) functions as a Lewis acid, forming stable coordination complexes without generating reactive oxygen species. In Alzheimer's disease, Zn(II) interacts with Aβ peptides in an approximately 1:1 stoichiometry, binding to residues in the N-terminal region (Aβ16) of the peptide, particularly from amongst Asp1, the three histidine (His6, His13, His14) and Glu11. Depending on pH, solvent and peptide conformation, residue such as Tyr10, the N-terminal amine, and the deprotonated amide of Arg5 can also be bound, as shown by NMR studies (135). For amylin, Zn(II) coordination mainly occurs at His18 in a 1:1 stoichiometry as well, and depending on the pH and conformation, with Lys1, Arg11, and Tyr37 (103,136). For both amylin and Aβ dimers, a single Zn(II) ion can bridge the histidine (or carboxylate) residues from two peptides, mediating peptide crosslinking in a 1:2 (metal:peptide) ratio, through residues such as Asp1, Glu11, and His13/14 for Aβ and His18 and Lys1 for amylin (118,137). The Zn(II) structure in Figure 1.6 shows how a coordinate may perform bridging in an Aβ dimer. Unlike copper or iron, whose binding can induce oxidative stress and form toxic fibrillar aggregates, Zn(II)'s interactions are structurally stabilizing and directly influence fibrillization. Zn(II) bridging the histidine residues between neighbouring peptides has been reported to be associated with both a prolonged lag phase and reduced β-sheet propagation, consistent with inhibited fibrillization, as well as increased cross-linking and a tendency toward formation of small oligomers and plaques, which are implicated in cytotoxicity (138–140). Particularly, Zn(II) may promote rapid oligomer cross-linking while being associated with stalling of ordered fibril elongation (off-pathway trapping). Zn(II) also modulates the secondary structure of Aβ, sometimes increasing α-helical content in monomers, or facilitating the α-helix to β-sheet transitions that promote fibrillogenesis. Beyond its role in pathology, Zn(II) is essential for neuronal function, regulating synaptic plasticity, enzyme activity, and signalling, yet its dysregulation – via plaque accumulation or local deficiency – can drive neurotoxicity, tau-phosphorylation, and neuroinflammation, highlighting its dual role and central importance in Aβ aggregation and Alzheimer's disease.

1.8 Computational Modelling of Aβ and Biomolecular Systems

Experimental studies indicate that Aβ and amylin are highly flexible, disorganized proteins with the ability to rapidly aggregate with one another and a propensity for

transitioning between oligomers. To study their chemistry and structural conformations in monomeric and dimeric forms, computational approaches like molecular dynamics (MD) simulations have been widely employed. This section reviews selected studies, highlighting key insights gained from these methods as well as their inherent limitations.

1.8.1 Molecular Modelling Methods

Molecular dynamics (MD) is used to study bioorganic systems, determining the movement of atoms over a time-dependent series, named a trajectory. It uses, amongst others, classical Molecular Mechanic (MM) methods to capture the trajectory and coordinates of the atomic structure at defined intervals. Each recorded structure is known as a frame, which can be plotted against the distance for classical descriptors to analyse the properties of the structure. Preferring these over the more accurate Quantum Mechanical (QM) analysis as it allows for faster simulations especially on structures as large as full-length Aβ. The work included within this thesis mainly considers only MM/MD methods with relevant studies reported below.

Berhanu *et al.* and Mehrazma & Rauk (68,141) provide evidence of the greater capabilities for the MM/MD approach on larger biomolecular systems such as the full length Aβ and amylin dimers over the QM methods, which explicitly account for electronic structure. The former presents the full-length amylin oligomer analysis while the latter looks at an Aβ dimer, reporting 9.5 μs worth of data, which is impractical to simulate with QM electronic-structure treatments as their sizes reach over the QM atom limit of ~500, up to ~1200 ensuring too great a computational cost compared to MM. Both studies converge on the conclusion that classical MM/MD approaches not only enable efficient simulation of amylin and amyloid dimers with statistically significant results but can also deliver structural and energetic insights at biologically relevant timescales.

Fan *et al.* (142) provides a strong computational basis for using molecular dynamics to investigate human amylin and Aβ heterodimers. The former shows the usage of all-atom discrete molecular dynamics (DMD) on mixtures of Aβ42 and human amylin, comparing Aβ aggregation events with cross-aggregation ones simulating heterodimer formation (143). The results suggest how the heterodimers are stabilized through the central hydrophobic regions of each component, with the

dimer formation being consistent with a lower free-energy barrier for β-sheet nucleation. However, using DMD limits the simulation to simple stepwise potentials that cannot fully capture fine energetic details (e.g., solvent effects, electrostatics, or subtle conformational energetics) that are accessible in continuous force-field based MD. Although examples of the heterodimer analysis under classical MD are sparse, the study by Su *et al.* (144,145) provides an investigation into human amylin and rat amylin ensembles using MD. It isolates the same “hotspot” of aggregation as the DMD simulation from the all-atom structural ensemble it generates, the hydrophobic core.

While explicit-solvent replica-exchange MD (REMD) may provide more exhaustive sampling of conformational space by running multiple temperature (or Hamiltonian) replicas and exchanging them to overcome energy barriers, as employed by Li *et al.* (146) to enhance sampling and avoid local minima Aβ–human amylin heterodimer simulations, conventional MD (cMD) still offers important advantages for studying these systems. REMD requires multiple replicas and significant computational resources, whereas cMD can provide longer continuous trajectories at physiological temperatures. By capturing continuous conformational transitions in a single trajectory, conventional MD can more accurately model the kinetics of heterodimer stabilization and the effects of solvent and interfacial interactions. Another drawback, like Hamiltonian exchange, is that the sampling can become biased by a single trajectory becoming trapped in a local minimum. To improve accuracy and confidence without the overhead computational cost of enhanced sampling, a triplicate method similar to Nasica-Laouze *et al.* (147) can be applied. Three independent replicates, under identical parameters but with different randomised initial velocities, sufficiently revealed the statistically reproducible structural ensembles. The study applied this triplicate methodology on Aβ oligomers simulations, enabling reliable averaging of classical descriptors like root-mean-square fluctuations (RMSF), radius of gyration (Rg), root-mean-square deviation (RMSD) distributions, and secondary-structure propensity across trajectories. The replicate approach suggested that certain structural features, such as β-strand formation in the hydrophobic core, consistently emerged regardless of starting velocities, while other peripheral regions displayed greater variability. This

demonstrated that replicates are essential for distinguishing between intrinsic flexibility and artefacts of trajectory initialization.

1.8.2 AMBER Forcefields and Constant-pH Molecular Dynamics

Building on these classical MD approaches, the choice of force field becomes critical for accurately modelling peptide dynamics. Considering that the focus of this research is on the effects of pH change on the structural conformations, AMBER ff10 is considered appropriate. AMBER ff10 is commonly adopted for peptide aggregation studies due to its balanced treatment of secondary-structure propensities and accurate parametrization of backbone dihedrals, providing a robust framework for modelling the conformational dynamics of full-length Aβ and amylin peptides (148,149). Swails *et al.* (150) demonstrates that AMBER ff10 can reliably reproduce the experimental pKa values of titratable residues in peptides, establishing their suitability for simulating amyloidogenic systems such as Aβ and human amylin. This is backed up by the Harris and Shen study (151), where they apply GPU-accelerated constant pH Molecular Dynamics (CpHMD) to amyloidogenic peptides, showing that shifts in the protonation of acidic residues such as Asp23 and Glu22 in Aβ were associated with changes in interchain salt-bridge formation and aggregation kinetics. This computational framework provides the new ability to probe effects of environmentally sensitive factors such as pH, making AMBER ff10 and the CpHMD a particularly valuable resource for studying the structural dynamics.

1.8.3 Modelling metal-Aβ and Related Biomolecular Systems

Strodel *et al.* (152) and Atrián-Blasco *et al.* (153) demonstrate how classical MM/MD simulations can be adapted to study transition-metal interactions in amyloidogenic peptides. They can display the preferred geometries of metals like Cu(II) or Zn(II) in non-bonded dummy-atom models when parameterized for MM forcefields without QM calculations; square-planar for the former and tetrahedral for the latter. It is important to note that, in this classical framework, coordination is represented through parameterized interactions that approximate geometry and energetics, but do not explicitly model electronic effects such as charge transfer or d-orbital bonding. These approaches accurately reproduced experimentally observed metal-binding behaviours, such as the lower affinity of Zn(II) for Aβ compared to Cu(II). The latter study focused on comparing the human amylin monomers and oligomers in explicit

and implicit solvents. Atrián-Blasco *et al.* explored metal binding in human amylin monomers and oligomers under different solvent treatments, demonstrating that solvent representation can influence metal-coordination geometry and affect structural features such as hydrogen-bonding networks. Their work also highlighted how Zn(II) can act as a structural modulator, stabilising loop regions and thereby altering aggregation pathways. These works illustrate how MM/MD-based methods can effectively capture transition-metal effects in amyloid systems while highlighting the role of solvent treatment in modulating peptide–metal interactions.

1.9 Research aims

The cooperation between Aβ and amylin at the initial nucleation stages of amyloid assembly is the central focus of this research, particularly where these early oligomeric events may contribute to Alzheimer's disease pathology. As discussed throughout this chapter, previous studies have characterised peptide behaviour under physiological conditions, under small (typically <0.5) pH deviations, and in the presence of metal ions within dimeric and higher-order complexes. Classical simulation approaches have been shown to be effective for modelling systems on the scale of Aβ peptides at a reasonable computational expense, even when the system size increases substantially for dimers, trimers, and mixed assemblies. However, the structural configurations adopted by Aβ and amylin at the earliest stages of nucleation – especially for cross-assemblies – remain comparatively poorly understood (154).

Accordingly, the main aim of this work is to use classical MD frameworks (including CpHMD where applicable) and practical sampling strategies to explore the structure and dynamical trends of amylin and Aβ40 in both self-assembly and cross-assembly, focusing on early oligomerisation steps such as dimerization and trimerization under physiologically relevant pH conditions. Aβ40 is selected over Aβ42 because it is the more abundant isoform in vivo (~80–90% of total Aβ), it is better represented in existing structural and biophysical datasets, and its slower aggregation kinetics make early-stage interfacial rearrangements and secondary-structure changes more tractable to simulate and interpret. Since both peptides contain titratable residues with pKa values that can place them near switching behaviour within physiological ranges, the pH-dependent structural dynamics are examined as a route to identify

subtle charge shifts that are consistent with altered compactness, aggregation competence, and secondary-structure preference during early nucleation.

A further aim is to evaluate how Zn(II) binding modulates these early assemblies. Zn(II) has been implicated as an important microenvironmental modulator in amyloid systems, and its interactions with Aβ and amylin are proposed to influence both association stability and the structural pathway of aggregation. By simulating peptide–metal complexes alongside metal-free controls, this work tests how Zn(II) affects flexibility, charge distribution, and secondary-structure outcomes in both homo- and hetero-assemblies under comparable conditions. Using a classical non-bonded metal model, further assessments were performed on whether Zn(II) can support persistent coordination to donor atoms from both chains – i.e., classical-coordination behaviour – thereby providing a plausible stabilisation mechanism for mixed early assemblies. Overall, the overarching aim of the work reported here is to generate mechanistic evidence for how pH and Zn(II) modulate early Aβ40–amylin oligomerisation, and to define testable conditions and interfacial behaviours that can inform future higher-fidelity simulations and experimental follow-up relevant to therapeutic strategies.

1.10 REFERENCES

1. Ballard C, Gauthier S, Corbett A, Brayne C, Aarsland D, Jones E. Alzheimer's disease. Lancet Lond Engl. 2011 Mar 19;377(9770):1019–31.

2. Hardy J. Has the amyloid cascade hypothesis for Alzheimer's disease been proved? Curr Alzheimer Res. 2006 Feb;3(1):71–3.

3. Alzheimer's Association [Internet]. [cited 2025 Sept 24]. What is Alzheimer's? Available from: https://www.alz.org/alzheimers-dementia/what-is-alzheimers

4. Stelzmann RA, Norman Schnitzlein H, Reed Murtagh F. An english translation of alzheimer's 1907 paper, "über eine eigenartige erkankung der hirnrinde". Clin Anat. 1995 Jan 1;8(6):429–31.

5. Rajan KB, Weuve J, Barnes LL, Wilson RS, Evans DA. Prevalence and incidence of clinically diagnosed Alzheimer's disease dementia from 1994 to 2012 in a population study. Alzheimers Dement J Alzheimers Assoc. 2019 Jan;15(1):1–7.

6. Tom SE, Hubbard RA, Crane PK, Haneuse SJ, Bowen J, McCormick WC, *et al.* Characterization of dementia and Alzheimer's disease in an older population: updated incidence and life expectancy with and without dementia. Am J Public Health. 2015 Feb;105(2):408–13.

7. Burns A, Byrne EJ, Maurer K. Alzheimer's disease. The Lancet. 2002 July 13;360(9327):163–5.

8. McKhann G, Drachman D, Folstein M, Katzman R, Price D, Stadlan EM. Clinical diagnosis of Alzheimer's disease: report of the NINCDS-ADRDA Work Group under the auspices of Department of Health and Human Services Task Force on Alzheimer's Disease. Neurology. 1984 July;34(7):939–44.

9. Plascencia-Villa G, Perry G. Neuropathologic Changes Provide Insights into Key Mechanisms of Alzheimer Disease and Related Dementia. Am J Pathol. 2022 Oct;192(10):1340–6.

10. Masters CL, Simms G, Weinman NA, Multhaup G, McDonald BL, Beyreuther K. Amyloid plaque core protein in Alzheimer disease and Down syndrome. Proc Natl Acad Sci U S A. 1985 June;82(12):4245–9.

11. Metal compounds as inhibitors of β-amyloid aggregation. Perspectives for an innovative metallotherapeutics on Alzheimer's disease. Coord Chem Rev. 2012 Oct 1;256(19–20):2357–66.

12. Blennow K, de Leon MJ, Zetterberg H. Alzheimer's disease. Lancet Lond Engl. 2006 July 29;368(9533):387–403.

13. Launer LJ, Ross GW, Petrovitch H, Masaki K, Foley D, White LR, *et al.* Midlife blood pressure and dementia: the Honolulu-Asia aging study. Neurobiol Aging. 2000;21(1):49–55.

14. Barnes DE, Yaffe K. The projected effect of risk factor reduction on Alzheimer's disease prevalence. Lancet Neurol. 2011 Sept;10(9):819–28.

15. Reitz C, den Heijer T, van Duijn C, Hofman A, Breteler MMB. Relation between smoking and risk of dementia and Alzheimer disease: the Rotterdam Study. Neurology. 2007 Sept 4;69(10):998–1005.

16. Notkola IL, Sulkava R, Pekkanen J, Erkinjuntti T, Ehnholm C, Kivinen P, *et al.* Serum total cholesterol, apolipoprotein E epsilon 4 allele, and Alzheimer's disease. Neuroepidemiology. 1998;17(1):14–20.

17. Soares HD, Sparks DL. Alzheimer's Disease. In: Topics in Medicinal Chemistry. Berlin, Heidelberg: Springer; 2007. p. 53–80.

18. Ruitenberg A, van Swieten JC, Witteman JCM, Mehta KM, van Duijn CM, Hofman A, *et al.* Alcohol consumption and risk of dementia: the Rotterdam Study. Lancet Lond Engl. 2002 Jan 26;359(9303):281–6.

19. LaFerla FM, Green KN, Oddo S. Intracellular amyloid-beta in Alzheimer's disease. Nat Rev Neurosci. 2007 July;8(7):499–509.

20. Gustafson D, Rothenberg E, Blennow K, Steen B, Skoog I. An 18-year follow-up of overweight and risk of Alzheimer disease. Arch Intern Med. 2003 July 14;163(13):1524–8.

21. Whitmer RA, Gunderson EP, Quesenberry CP, Zhou J, Yaffe K. Body mass index in midlife and risk of Alzheimer disease and vascular dementia. Curr Alzheimer Res. 2007 Apr;4(2):103–9.

22. International Genomics of Alzheimer's Disease Consortium (IGAP). Convergent genetic and expression data implicate immunity in Alzheimer's disease. Alzheimers Dement J Alzheimers Assoc. 2015 June;11(6):658–71.

23. Singh B, Parsaik AK, Mielke MM, Erwin PJ, Knopman DS, Petersen RC, *et al.* Association of mediterranean diet with mild cognitive impairment and Alzheimer's disease: a systematic review and meta-analysis. J Alzheimers Dis JAD. 2014;39(2):271–82.

24. Lu T, Pan Y, Kao SY, Li C, Kohane I, Chan J, *et al.* Gene regulation and DNA damage in the ageing human brain. Nature. 2004 June 24;429(6994):883–91.

25. Leibold N, Bain JR, Despa F. Type-2 Diabetes, Pancreatic amylin, and Neuronal Metabolic Remodeling in Alzheimer's Disease. Mol Nutr Food Res. 2024;68(13):2200405.

26. Horrell EL, Allsop B, Robinson A, Mann D, Unwin R, Cooper G, *et al.* P1-183: THE ROLE OF amylin IN ALZHEIMER'S DISEASE. Alzheimers Dement. 2018;14(7S_Part_6):P348–9.

27. Bharadwaj P, Wijesekara N, Liyanapathirana M, Newsholme P, Ittner L, Fraser P, *et al.* The Link between Type 2 Diabetes and Neurodegeneration: Roles for amyloid-β, amylin, and Tau Proteins. J Alzheimers Dis JAD. 2017;59(2):421–32.

28. Haass C, Selkoe DJ. Soluble protein oligomers in neurodegeneration: lessons from the Alzheimer's amyloid beta-peptide. Nat Rev Mol Cell Biol. 2007 Feb;8(2):101–12.

29. Kandimalla R, Reddy PH. Therapeutics of Neurotransmitters in Alzheimer's Disease. J Alzheimers Dis JAD. 2017;57(4):1049–69.

30. Kepp KP. Bioinorganic chemistry of Alzheimer's disease. Chem Rev. 2012 Oct 10;112(10):5193–239.

31. Moreno-Gonzalez I, Edwards Iii G, Salvadores N, Shahnawaz M, Diaz-Espinoza R, Soto C. Molecular interaction between type 2 diabetes and Alzheimer's disease through cross-seeding of protein misfolding. Mol Psychiatry. 2017 Sept;22(9):1327–34.

32. Walsh DM, Hartley DM, Kusumoto Y, Fezoui Y, Condron MM, Lomakin A, *et al. Amyloid* beta-protein fibrillogenesis. Structure and biological activity of protofibrillar intermediates. J Biol Chem. 1999 Sept 3;274(36):25945–52.

33. Hureau C, Faller P. Abeta-mediated ROS production by Cu ions: structural insights, mechanisms and relevance to Alzheimer's disease. Biochimie. 2009 Oct;91(10):1212–7.

34. Baumketner A, Bernstein SL, Wyttenbach T, Lazo ND, Teplow DB, Bowers MT, *et al.* Structure of the 21–30 fragment of amyloid β-protein. Protein Sci. 2006 June 1;15(6):1239–47.

35. Krone MG, Baumketner A, Bernstein SL, Wyttenbach T, Lazo ND, Teplow DB, *et al.* Effects of Familial Alzheimer's Disease Mutations on the Folding Nucleation of the amyloid β-Protein. J Mol Biol. 2008 Aug 1;381(1):221–8.

36. Lührs T, Ritter C, Adrian M, Riek-Loher D, Bohrmann B, Döbeli H, *et al.* 3D structure of Alzheimer's amyloid-beta(1-42) fibrils. Proc Natl Acad Sci U S A. 2005 Nov 29;102(48):17342–7.

37. Takeda T, Klimov DK. Side Chain Interactions Can Impede amyloid Fibril Growth: Replica Exchange Simulations of Aβ Peptide Mutant. J Phys Chem B. 2009 Sept 3;113(35):11848–57.

38. Maynard CJ, Bush AI, Masters CL, Cappai R, Li QX. Metals and amyloid-β in Alzheimer's disease. Int J Exp Pathol. 2005 June;86(3):147–59.

39. Yamada M. Cerebral amyloid angiopathy: an overview. Neuropathol Off J Jpn Soc Neuropathol. 2000 Mar;20(1):8–22.

40. Norfray JF, Provenzale JM. Alzheimer's disease: neuropathologic findings and recent advances in imaging. AJR Am J Roentgenol. 2004 Jan;182(1):3–13.

41. Karantzoulis S, Galvin JE. Distinguishing Alzheimer's disease from other major forms of dementia. Expert Rev Neurother. 2011 Nov;11(11):1579–91.

42. Mann DM. Pyramidal nerve cell loss in Alzheimer's disease. Neurodegener J Neurodegener Disord Neuroprotection Neuroregeneration. 1996 Dec;5(4):423–7.

43. Klein WL. Abeta toxicity in Alzheimer's disease: globular oligomers (ADDLs) as new vaccine and drug targets. Neurochem Int. 2002 Nov;41(5):345–52.

44. Ricciarelli R, Fedele E. The amyloid Cascade Hypothesis in Alzheimer's Disease: It's Time to Change Our Mind. Curr Neuropharmacol. 2017;15(6):926–35.

45. Lovestone S. Fleshing out the amyloid cascade hypothesis: the molecular biology of Alzheimer's disease. Dialogues Clin Neurosci [Internet]. 2000 June 30 [cited 2025 Sept 25]; Available from: https://www.tandfonline.com/doi/abs/10.31887/DCNS.2000.2.2/slovestone

46. Nagel-Steger L, Owen MC, Strodel B. An Account of amyloid Oligomers: Facts and Figures Obtained from Experiments and Simulations. ChemBioChem. 2016 Apr 15;17(8):657–76.

47. Baskakov IV. Branched chain mechanism of polymerization and ultrastructure of prion protein amyloid fibrils. FEBS J. 2007 Aug 1;274(15):3756–65.

48. Šarić A, Chebaro YC, Knowles TPJ, Frenkel D. Crucial role of nonspecific interactions in amyloid nucleation. Proc Natl Acad Sci U S A. 2014 Dec 16;111(50):17869–74.

49. Rogacheva MV, Bochenkova AV, Kuznetsova SA, Saparbaev MK, Nemukhin AV. Impact of pyrophosphate and O-ethyl-substituted pyrophosphate groups on DNA structure. J Phys Chem B. 2007 Jan 18;111(2):432–8.

50. Reddy PH. Abnormal tau, mitochondrial dysfunction, impaired axonal transport of mitochondria, and synaptic deprivation in Alzheimer's disease. Brain Res. 2011 Sept 30;1415:136–48.

51. Busche MA, Hyman BT. Synergy between amyloid-β and tau in Alzheimer's disease. Nat Neurosci. 2020 Oct;23(10):1183–93.

52. Teich AF, Arancio O. Is the amyloid Hypothesis of Alzheimer's disease therapeutically relevant? Biochem J. 2012 Sept 1;446(2):165–77.

53. Sorrentino P, Iuliano A, Polverino A, Jacini F, Sorrentino G. The dark sides of amyloid in Alzheimer's disease pathogenesis. FEBS Lett. 2014 Mar 3;588(5):641–52.

54. Aizenstein HJ, Nebes RD, Saxton JA, Price JC, Mathis CA, Tsopelas ND, *et al.* Frequent amyloid deposition without significant cognitive impairment among the elderly. Arch Neurol. 2008 Nov;65(11):1509–17.

55. Bouwman FH, Schoonenboom NSM, Verwey NA, van Elk EJ, Kok A, Blankenstein MA, *et al.* CSF biomarker levels in early and late onset Alzheimer's disease. Neurobiol Aging. 2009 Dec;30(12):1895–901.

56. Walsh DM, Klyubin I, Fadeeva JV, Cullen WK, Anwyl R, Wolfe MS, *et al.* Naturally secreted oligomers of amyloid beta protein potently inhibit hippocampal long-term potentiation in vivo. Nature. 2002 Apr 4;416(6880):535–9.

57. Jack CR, Knopman DS, Jagust WJ, Shaw LM, Aisen PS, Weiner MW, *et al.* Hypothetical model of dynamic biomarkers of the Alzheimer's pathological cascade. Lancet Neurol. 2010 Jan;9(1):119–28.

58. Cleary JP, Walsh DM, Hofmeister JJ, Shankar GM, Kuskowski MA, Selkoe DJ, *et al.* Natural oligomers of the amyloid-beta protein specifically disrupt cognitive function. Nat Neurosci. 2005 Jan;8(1):79–84.

59. Sengupta U, Nilson AN, Kayed R. The Role of amyloid-β Oligomers in Toxicity, Propagation, and Immunotherapy. EBioMedicine. 2016 Apr;6:42–9.

60. Hefti F, Goure WF, Jerecic J, Iverson KS, Walicke PA, Krafft GA. The case for soluble Aβ oligomers as a drug target in Alzheimer's disease. Trends Pharmacol Sci. 2013 May;34(5):261–6.

61. Glabe CG. Common mechanisms of amyloid oligomer pathogenesis in degenerative disease. Neurobiol Aging. 2006 Apr;27(4):570–5.

62. Vivekanandan S, Brender JR, Lee SY, Ramamoorthy A. A partially folded structure of amyloid-beta(1-40) in an aqueous environment. Biochem Biophys Res Commun. 2011 July 29;411(2):312–6.

63. Hung LW, Ciccotosto GD, Giannakis E, Tew DJ, Perez K, Masters CL, *et al.* *Amyloid*-β Peptide (Aβ) Neurotoxicity Is Modulated by the Rate of Peptide Aggregation: Aβ Dimers and Trimers Correlate with Neurotoxicity. J Neurosci. 2008 Nov 12;28(46):11950–8.

64. Somavarapu AK, Kepp KP. The Dependence of amyloid-β Dynamics on Protein Force Fields and Water Models. ChemPhysChem. 2015 Oct 1;16(15):3278–89.

65. Halverson K, Fraser PE, Kirschner DA, Lansbury PT. Molecular determinants of amyloid deposition in Alzheimer's disease: conformational studies of synthetic beta-protein fragments. Biochemistry. 1990 Mar 20;29(11):2639–44.

66. Schmechel A, Zentgraf H, Scheuermann S, Fritz G, Pipkorn R, Reed J, *et al.* Alzheimer β-Amyloid Homodimers Facilitate Aβ Fibrillization and the Generation of Conformational Antibodies *. J Biol Chem. 2003 Sept 12;278(37):35317–24.

67. Hatami A, Monjazeb S, Milton S, Glabe CG. Familial Alzheimer's Disease Mutations within the amyloid Precursor Protein Alter the Aggregation and Conformation of the amyloid-β Peptide. J Biol Chem. 2017 Feb 24;292(8):3172–85.

68. Berhanu WM, Yaşar F, Hansmann UHE. In silico cross seeding of Aβ and amylin fibril-like oligomers. ACS Chem Neurosci. 2013 Nov 20;4(11):1488–500.

69. Jackson K, Barisone GA, Diaz E, Jin L way, DeCarli C, Despa F. Amylin deposition in the brain: A second amyloid in Alzheimer disease? Ann Neurol. 2013 Oct;74(4):517–26.

70. Dai Z, Ben-Younis A, Vlachaki A, Raleigh D, Thalassinos K. Understanding the structural dynamics of human islet amyloid polypeptide: Advancements in and applications of ion-mobility mass spectrometry. Biophys Chem. 2024 Sept;312:107285.

71. Westermark P, Andersson A, Westermark GT. Islet amyloid polypeptide, islet amyloid, and diabetes mellitus. Physiol Rev. 2011 July;91(3):795–826.

72. Bower RL, Hay DL. Amylin structure–function relationships and receptor pharmacology: implications for amylin mimetic drug development. Br J Pharmacol. 2016 June;173(12):1883–98.

73. Akter R, Cao P, Noor H, Ridgway Z, Tu LH, Wang H, *et al.* Islet amyloid Polypeptide: Structure, Function, and Pathophysiology. J Diabetes Res. 2016;2016:2798269.

74. Zhang XX, Pan YH, Huang YM, Zhao HL. Neuroendocrine hormone amylin in diabetes. World J Diabetes. 2016 May 10;7(9):189–97.

75. Tilakaratne N, Christopoulos G, Zumpe ET, Foord SM, Sexton PM. Amylin receptor phenotypes derived from human calcitonin receptor/RAMP coexpression exhibit pharmacological differences dependent on receptor isoform and host cell environment. J Pharmacol Exp Ther. 2000 July;294(1):61–72.

76. Li X, Lao Z, Zou Y, Dong X, Li L, Wei G. Mechanistic Insights into the Co-Aggregation of Aβ and human amylin: An All-Atom Molecular Dynamic Study. J Phys Chem B. 2021 Mar 4;125(8):2050–60.

77. Mietlicki-Baase EG. Amylin in Alzheimer's disease: Pathological peptide or potential treatment? Neuropharmacology. 2018 July 1;136(Pt B):287–97.

78. Jha S, Snell JM, Sheftic SR, Patil SM, Daniels SB, Kolling FW, *et al.* pH dependence of amylin fibrillization. Biochemistry. 2014 Jan 21;53(2):300–10.

79. Ridgway Z, Zhang X, Wong AG, Abedini A, Schmidt AM, Raleigh DP. Analysis of the role of the conserved disulfide in amyloid formation by human IAPP in homogenous and heterogeneous environments. Biochemistry. 2018 May 29;57(21):3065–74.

80. Mulder H, Ahrén B, Sundler F. Islet amyloid polypeptide and insulin gene expression are regulated in parallel by glucose in vivo in rats. Am J Physiol. 1996 Dec;271(6 Pt 1):E1008-1014.

81. Paulsson JF, Andersson A, Westermark P, Westermark GT. Intracellular amyloid-like deposits contain unprocessed pro-islet amyloid polypeptide (proIAPP) in beta cells of transgenic mice overexpressing the gene for human IAPP and transplanted human islets. Diabetologia. 2006 June;49(6):1237–46.

82. Mukherjee A, Morales-Scheihing D, Salvadores N, Moreno-Gonzalez I, Gonzalez C, Taylor-Presse K, *et al.* Induction of IAPP amyloid deposition and associated diabetic abnormalities by a prion-like mechanism. J Exp Med. 2017 Aug 1;214(9):2591–610.

83. Raimundo AF, Ferreira S, Martins IC, Menezes R. Islet amyloid Polypeptide: A Partner in Crime With Aβ in the Pathology of Alzheimer's Disease. Front Mol

Neurosci [Internet]. 2020 Mar 20 [cited 2025 Sept 26];13. Available from: https://www.frontiersin.org/journals/molecular-neuroscience/articles/10.3389/fnmol.2020.00035/full

84. Bram Y, Frydman-Marom A, Yanai I, Gilead S, Shaltiel-Karyo R, Amdursky N, *et al.* Apoptosis induced by islet amyloid polypeptide soluble oligomers is neutralized by diabetes-associated specific antibodies. Sci Rep. 2014 Mar 4;4(1):4267.

85. Westermark P, Grimelius L. The pancreatic islet cells in insular amyloidosis in human diabetic and non-diabetic adults. Acta Pathol Microbiol Scand [A]. 1973 May;81(3):291–300.

86. Lutz TA, Meyer U. Amylin at the interface between metabolic and neurodegenerative disorders. Front Neurosci. 2015;9:216.

87. Banks WA, Kastin AJ, Maness LM, Huang W, Jaspan JB. Permeability of the blood-brain barrier to amylin. Life Sci. 1995;57(22):1993–2001.

88. Armiento V, Spanopoulou A, Kapurniotu A. Peptide-Based Molecular Strategies To Interfere with Protein Misfolding, Aggregation, and Cell Degeneration. Angew Chem Int Ed Engl. 2020 Feb 24;59(9):3372–84.

89. Fawver JN, Ghiwot Y, Koola C, Carrera W, Rodriguez-Rivera J, Hernandez C, *et al.* Islet amyloid polypeptide (IAPP): a second amyloid in Alzheimer's disease. Curr Alzheimer Res. 2014;11(10):928–40.

90. Jackson LA, Gurtman A, van Cleeff M, Jansen KU, Jayawardene D, Devlin C, *et al.* Immunogenicity and safety of a 13-valent pneumococcal conjugate vaccine compared to a 23-valent pneumococcal polysaccharide vaccine in pneumococcal vaccine-naive adults. Vaccine. 2013 Aug 2;31(35):3577–84.

91. Srodulski S, Sharma S, Bachstetter AB, Brelsfoard JM, Pascual C, Xie XS, *et al.* Neuroinflammation and neurologic deficits in diabetes linked to brain accumulation of amylin. Mol Neurodegener. 2014 Aug 22;9:30.

92. Kotiya D, Leibold N, Verma N, Jicha GA, Goldstein LB, Despa F. Rapid, scalable assay of amylin-β amyloid co-aggregation in brain tissue and blood. J Biol Chem. 2023 May;299(5):104682.

93. Kurochkin IV, Goto S. Alzheimer's beta-amyloid peptide specifically interacts with and is degraded by insulin degrading enzyme. FEBS Lett. 1994 May 23;345(1):33–7.

94. Guan H, Chow KM, Shah R, Rhodes CJ, Hersh LB. Degradation of Islet amyloid Polypeptide by Neprilysin. Diabetologia. 2012 Nov;55(11):2989–98.

95. Hama E, Shirotani K, Masumoto H, Sekine-Aizawa Y, Aizawa H, Saido TC. Clearance of extracellular and cell-associated amyloid beta peptide through viral expression of neprilysin in primary neurons. J Biochem (Tokyo). 2001 Dec;130(6):721–6.

96. Bharadwaj P, Solomon T, Sahoo BR, Ignasiak K, Gaskin S, Rowles J, *et al. Amylin* and beta amyloid proteins interact to form amorphous heterocomplexes with enhanced toxicity in neuronal cells. Sci Rep. 2020 June 25;10(1):10356.

97. Hartter E, Svoboda T, Ludvik B, Schuller M, Lell B, Kuenburg E, *et al.* Basal and stimulated plasma levels of pancreatic amylin indicate its co-secretion with insulin in humans. Diabetologia. 1991 Jan;34(1):52–4.

98. Adler BL, Yarchoan M, Hwang HM, Louneva N, Blair JA, Palm R, *et al.* Neuroprotective effects of the amylin analogue pramlintide on Alzheimer's disease pathogenesis and cognition. Neurobiol Aging. 2014 Apr;35(4):793–801.

99. Petkova AT, Yau WM, Tycko R. Experimental constraints on quaternary structure in Alzheimer's beta-amyloid fibrils. Biochemistry. 2006 Jan 17;45(2):498–512.

100. van Gestel J, de Leeuw SW. The Formation of Fibrils by Intertwining of Filaments: Model and Application to amyloid Aβ Protein. Biophys J. 2007 Feb 15;92(4):1157–63.

101. Garzon-Rodriguez W, Sepulveda-Becerra M, Milton S, Glabe CG. Soluble amyloid Abeta-(1-40) exists as a stable dimer at low concentrations. J Biol Chem. 1997 Aug 22;272(34):21037–44.

102. Qiang W, Yau WM, Lu JX, Collinge J, Tycko R. Structural Variation in amyloid-β Fibrils from Alzheimer's Disease Clinical Subtypes. Nature. 2017 Jan 12;541(7636):217–21.

103. Tsvetkov PO, Kulikova AA, Golovin AV, Tkachev YV, Archakov AI, Kozin SA, *et al.* Minimal Zn2+ Binding Site of amyloid-β. Biophys J. 2010 Nov 17;99(10):L84–6.

104. Blinov N, Khorvash M, Wishart DS, Cashman NR, Kovalenko A. ACS Publications. American Chemical Society; 2017 [cited 2025 Sept 26]. Initial Structural Models of the Aβ42 Dimer from Replica Exchange Molecular Dynamics Simulations. Available from: https://pubs.acs.org/doi/full/10.1021/acsomega.7b00805

105. Tycko R. Solid-state NMR studies of amyloid fibril structure. Annu Rev Phys Chem. 2011;62:279–99.

106. Côté S, Laghaei R, Derreumaux P, Mousseau N. ACS Publications. American Chemical Society; 2012 [cited 2025 Sept 26]. Distinct Dimerization for Various Alloforms of the amyloid-Beta Protein: Aβ1–40, Aβ1–42, and Aβ1–40(D23N). Available from: https://pubs.acs.org/doi/abs/10.1021/jp2126366

107. Miller Y, Ma B, Tsai CJ, Nussinov R. Hollow core of Alzheimer's Aβ42 amyloid observed by cryoEM is relevant at physiological pH. Proc Natl Acad Sci U S A. 2010 Aug 10;107(32):14128–33.

108. Paravastu AK, Leapman RD, Yau WM, Tycko R. Molecular structural basis for polymorphism in Alzheimer's beta-amyloid fibrils. Proc Natl Acad Sci U S A. 2008 Nov 25;105(47):18349–54.

109. Taylor AIP, Staniforth RA. General Principles Underpinning amyloid Structure. Front Neurosci [Internet]. 2022 June 2 [cited 2025 Sept 26];16. Available from: https://www.frontiersin.org/journals/neuroscience/articles/10.3389/fnins.2022.878869/full

110. Nilsson MR, Raleigh DP. Analysis of amylin cleavage products provides new insights into the amyloidogenic region of human amylin. J Mol Biol. 1999 Dec 17;294(5):1375–85.

111. Moriarty‡ DF, Daniel P. Raleigh* ‡. ACS Publications. American Chemical Society; 1999 [cited 2025 Sept 26]. Effects of Sequential Proline Substitutions on amyloid Formation by Human amylin20-29†. Available from: https://pubs.acs.org/doi/abs/10.1021/bi981658g

112. Wiltzius JJW, Sievers SA, Sawaya MR, Cascio D, Popov D, Riekel C, *et al.* Atomic structure of the cross-β spine of islet amyloid polypeptide (amylin). Protein Sci Publ Protein Soc. 2008 Sept;17(9):1467–74.

113. Röder C, Kupreichyk T, Gremer L, Schäfer LU, Pothula KR, Ravelli RBG, *et al.* Cryo-EM structure of islet amyloid polypeptide fibrils reveals similarities with amyloid-β fibrils. Nat Struct Mol Biol. 2020 July;27(7):660–7.

114. Andreetto E, Yan LM, Tatarek-Nossol M, Velkova A, Frank R, Kapurniotu A. Identification of hot regions of the Abeta-IAPP interaction interface as high-affinity binding sites in both cross- and self-association. Angew Chem Int Ed Engl. 2010 Apr 12;49(17):3081–5.

115. Seeliger J, Evers F, Jeworrek C, Kapoor S, Weise K, Andreetto E, *et al.* Cross-amyloid interaction of Aβ and IAPP at lipid membranes. Angew Chem Int Ed Engl. 2012 Jan 16;51(3):679–83.

116. Hu R, Zhang M, Chen H, Jiang B, Zheng J. Cross-Seeding Interaction between β-Amyloid and Human Islet amyloid Polypeptide. ACS Chem Neurosci. 2015 Oct 21;6(10):1759–68.

117. Bakou M, Hille K, Kracklauer M, Spanopoulou A, Frost CV, Malideli E, *et al.* Key aromatic/hydrophobic amino acids controlling a cross-amyloid peptide interaction versus amyloid self-assembly. J Biol Chem. 2017 Sept 1;292(35):14587–602.

118. Alghrably M, Czaban I, Jaremko Ł, Jaremko M. Interaction of amylin species with transition metals and membranes. J Inorg Biochem. 2019 Feb;191:69–76.

119. McCalpin SD, Khemtemourian L, Suladze S, Ivanova MI, Reif B, Ramamoorthy A. Zinc and pH modulate the ability of insulin to inhibit aggregation of islet amyloid polypeptide. Commun Biol. 2024 June 27;7(1):776.

120. Tian Y, Viles JH. pH Dependence of amyloid-β Fibril Assembly Kinetics: Unravelling the Microscopic Molecular Processes. Angew Chem Int Ed Engl. 2022 Nov 25;61(48):e202210675.

121. Noh D, Bower RL, Hay DL, Zhyvoloup A, Raleigh DP. Analysis of amylin Consensus Sequences Suggests that Human amylin is Not Optimized to Minimize

amyloid Formation and Provides Clues to Factors that Modulate amyloidogenicity. ACS Chem Biol. 2020 June 19;15(6):1408–16.

122. Oskarsson ME, Paulsson JF, Schultz SW, Ingelsson M, Westermark P, Westermark GT. In vivo seeding and cross-seeding of localized amyloidosis: a molecular link between type 2 diabetes and Alzheimer disease. Am J Pathol. 2015 Mar;185(3):834–46.

123. Tabner BJ, Mayes J, Allsop D. Hypothesis: Soluble Aβ Oligomers in Association with Redox-Active Metal Ions Are the Optimal Generators of Reactive Oxygen Species in Alzheimer's Disease. Int J Alzheimers Dis. 2010 Nov 14;2011:546380.

124. Cheignon C, Tomas M, Bonnefont-Rousselot D, Faller P, Hureau C, Collin F. Oxidative stress and the amyloid beta peptide in Alzheimer's disease. Redox Biol. 2017 Oct 18;14:450–64.

125. Nadal RC, Rigby SEJ, Viles JH. Amyloid β−Cu2+ Complexes in both Monomeric and Fibrillar Forms Do Not Generate H2O2 Catalytically but Quench Hydroxyl Radicals. Biochemistry. 2008 Nov 4;47(44):11653–64.

126. Allsop D, Mayes J, Moore S, Masad A, Tabner BJ. Metal-dependent generation of reactive oxygen species from amyloid proteins implicated in neurodegenerative disease. Biochem Soc Trans. 2008 Nov 19;36(6):1293–8.

127. Smith DG, Cappai R, Barnham KCAL. The redox chemistry of the Alzheimer's disease amyloid beta peptide. Biochim Biophys Acta. 2007 Aug;1768(8):1976–90.

128. Burnet FM. A POSSIBLE ROLE OF ZINC IN THE PATHOLOGY OF DEMENTIA. Orig Publ Vol 1 Issue 8213. 1981 Jan 24;317(8213):186–8.

129. Sunda AP, Sharma AK. Molecular Insights into Cu/Zn Metal Response to the amyloid β-Peptide (1–42). ACS Phys Chem Au. 2024 Jan 24;4(1):57–66.

130. Strozyk D, Launer LJ, Adlard PA, Cherny RA, Tsatsanis A, Volitakis I, *et al.* Zinc and Copper Modulate Alzheimer Aβ Levels in Human Cerebrospinal Fluid. Neurobiol Aging. 2009 July;30(7):1069–77.

131. Bush AI, Multhaup G, Moir RD, Williamson TG, Small DH, Rumble B, *et al.* A novel zinc(II) binding site modulates the function of the beta A4 amyloid protein precursor of Alzheimer's disease. J Biol Chem. 1993 Aug 5;268(22):16109–12.

132. Miller Y, Ma B, Nussinov R. Zinc ions promote Alzheimer Aβ aggregation via population shift of polymorphic states. Proc Natl Acad Sci. 2010 May 25;107(21):9490–5.

133. Lee MC, Yu WC, Shih YH, Chen CY, Guo ZH, Huang SJ, *et al.* Zinc ion rapidly induces toxic, off-pathway amyloid-β oligomers distinct from amyloid-β derived diffusible ligands in Alzheimer's disease. Sci Rep. 2018 Mar 19;8(1):4772.

134. Xu Y, Xiao G, Liu L, Lang M. Zinc transporters in Alzheimer's disease. Mol Brain. 2019 Dec 9;12(1):106.

135. Wang L, Yin YL, Liu XZ, Shen P, Zheng YG, Lan XR, *et al.* Current understanding of metal ions in the pathogenesis of Alzheimer's disease. Transl Neurodegener. 2020 Apr 3;9(1):10.

136. Gaggelli E, Janicka-Klos A, Jankowska E, Kozlowski H, Migliorini C, Molteni E, *et al.* NMR studies of the Zn2+ interactions with rat and human beta-amyloid (1-28) peptides in water-micelle environment. J Phys Chem B. 2008 Jan 10;112(1):100–9.

137. Rowińska-Żyrek M. Coordination of Zn2+ and Cu2+ to the membrane disrupting fragment of amylin. Dalton Trans. 2016 May 10;45(19):8099–106.

138. Streltsov VA, Titmuss SJ, Epa VC, Barnham KCAL, Masters CL, Varghese JN. The structure of the amyloid-beta peptide high-affinity copper II binding site in Alzheimer disease. Biophys J. 2008 Oct;95(7):3447–56.

139. Istrate AN, Kozin SA, Zhokhov SS, Mantsyzov AB, Kechko OI, Pastore A, *et al.* Interplay of histidine residues of the Alzheimer's disease Aβ peptide governs its Zn-induced oligomerization. Sci Rep. 2016 Feb 22;6(1):21734.

140. Xu L, Wang X, Wang X. Effects of Zn2+ binding on the structural and dynamic properties of amyloid β peptide associated with Alzheimer's disease: Asp1 or Glu11? ACS Chem Neurosci. 2013 Nov 20;4(11):1458–68.

141. Kechko OI, Adzhubei AA, Tolstova AP, Indeykina MI, Popov IA, Zhokhov SS, *et al.* Molecular Mechanism of Zinc-Dependent Oligomerization of Alzheimer's amyloid-β with Taiwan (D7H) Mutation. Int J Mol Sci. 2023 Jan;24(14):11241.

142. Fan X, Zhang X, Yan J, Xu H, Zhao W, Ding F, *et al.* Computational Investigation of Coaggregation and Cross-Seeding between Aβ and human amylin Underpinning the Cross-Talk in Alzheimer's Disease and Type 2 Diabetes. J Chem Inf Model. 2024 July 8;64(13):5303–16.

143. Li X, Lao Z, Zou Y, Dong X, Li L, Wei G. Mechanistic Insights into the Co-Aggregation of Aβ and human amylin: An All-Atom Molecular Dynamic Study. J Phys Chem B. 2021 Mar 4;125(8):2050–60.

144. Mehrazma B, Rauk A. Exploring amyloid-β Dimer Structure Using Molecular Dynamics Simulations. J Phys Chem A. 2019 June 6;123(22):4658–70.

145. Su X, Wang K, Liu N, Chen J, Li Y, Duan M. All-atom structure ensembles of islet amyloid polypeptides determined by enhanced sampling and experiment data restraints. Proteins Struct Funct Bioinforma. 2019;87(7):541–50.

146. Li X, Zhang Y, Yang Z, Zhang S, Zhang L. The Inhibition Effect of Epigallocatechin-3-Gallate on the Co-Aggregation of amyloid-β and Human Islet amyloid Polypeptide Revealed by Replica Exchange Molecular Dynamics Simulations. Int J Mol Sci. 2024 Jan 29;25(3):1636.

147. Nasica-Labouze J, Nguyen PH, Sterpone F, Berthoumieu O, Buchete NV, Coté S, *et al. Amyloid* β Protein and Alzheimer's Disease: When Computer Simulations Complement Experimental Studies. Chem Rev. 2015 May 13;115(9):3518–63.

148. Lopes PEM, Guvench O, MacKerell AD. Current Status of Protein Force Fields for Molecular Dynamics. Methods Mol Biol Clifton NJ. 2015;1215:47–71.

149. Cornell WD, Cieplak P, Bayly CI, Gould IR, Merz KM, Ferguson DM, *et al.* A Second Generation Force Field for the Simulation of Proteins, Nucleic Acids, and Organic Molecules. J Am Chem Soc. 1995 May 1;117(19):5179–97.

150. Swails JM, York DM, Roitberg AE. Constant pH Replica Exchange Molecular Dynamics in Explicit Solvent Using Discrete Protonation States: Implementation, Testing, and Validation. J Chem Theory Comput. 2014 Mar 11;10(3):1341–52.

151. Harris RC, Shen J. GPU-Accelerated Implementation of Continuous Constant pH Molecular Dynamics in Amber: pKa Predictions with Single-pH Simulations. J Chem Inf Model. 2019 Nov 25;59(11):4821–32.

152. Strodel B, Coskuner-Weber O. Transition Metal Ion Interactions with Disordered amyloid-β Peptides in the Pathogenesis of Alzheimer's Disease: Insights from Computational Chemistry Studies. J Chem Inf Model. 2019 May 28;59(5):1782–805.

153. Atrián-Blasco E, Gonzalez P, Santoro A, Alies B, Faller P, Hureau C. Cu and Zn coordination to amyloid peptides: From fascinating chemistry to debated pathological relevance. Coord Chem Rev. 2018 Sept 15;371:38–55.

154. Zhang X, Fu Z, Meng L, He M, Zhang Z. The Early Events That Initiate β-Amyloid Aggregation in Alzheimer's Disease. Front Aging Neurosci [Internet]. 2018;Volume 10-2018. Available from: https://www.frontiersin.org/journals/aging-neuroscience/articles/10.3389/fnagi.2018.00359

Chapter 2: Theory

2.0 Introduction

High level of theory on the chemistry and physics behind the known atomic behaviours can allow modelling of structures and energies of small molecules with relative accuracy, whereas monitoring larger systems containing hundreds of atoms requires more approximate methods. In this chapter, we will explore the theoretical basis behind the computational methods employed in this report, focusing on molecular mechanics and molecular dynamics (1–5).

2.1 Molecular Mechanics (MM)

Computational chemistry includes a range of approaches, but quantum mechanical (QM) methods—such as ab initio and semi-empirical calculations—are typically applied to relatively small systems because they treat electronic structure explicitly. This allows high accuracy for energies, geometries, and conformational preferences, but the computational cost increases steeply with system size. As a result, QM methods become impractical for large biomolecules, where the number of atoms (and therefore the accessible configurational space) is much greater and would require prohibitively long compute times. Molecular mechanics (MM) provides a cheaper alternative by modelling atoms as classical particles and estimating the potential energy from empirical force-field terms based on nuclear positions—using parameters for bonded interactions and non-bonded interactions—rather than calculating electronic structure directly.

2.1.1 Forcefield and Energies

An important concept in molecular mechanics is the use of force fields, whose central principle is transferability. For molecular mechanics to describe the energetics of a system, applying a force field is necessary, as it provides the mathematical framework for approximating the potential energy of a molecular system. It can be conceptualized via a Newtonian ball-and-spring model, where atoms are treated as point masses, “balls”, and the strain on them by the restoring forces of bonds act as spring resisting deformation in accordance with Hooke's law (6). Within this framework, the total energy of a molecule is expressed as the sum of bonded interactions (stretching, bending, torsion), which describe local vibrational and rotational motions as harmonic or periodic functions, and non-bonded

interactions (van der Waals and electrostatics) that account for longer-range attractive and repulsive forces, as presented in Equation 2.1.

$$E_{tot} = \underbrace{E_{stretch} + E_{bend} + E_{torsion}}_{\text{Bonded Terms}} + \underbrace{E_{vdW} + E_{electrostatic}}_{\text{Nonbonded Terms}}$$

Equation 2.1 Representation of the total molecular mechanics potential energy, specified for bonded and non-bonded energies. $E_{stretch}$ represents the energy function for bond stretching in the system, E_{bend} is for the energy needed to bend an angle, $E_{torsion}$ is the energy required for rotation around a bond, E_{vdW} and $E_{elctrostatic}$ corresponds to the non-bonding interactions; van der Waals and electrostatic energy contributions usually require the bulk of the computational power over the course of dynamics simulations to calculate.

These energies are represented by empirical functions that are derived from quantum chemical calculations of the Born–Oppenheimer potential energy surface (PES) with parameters optimized to reproduce structural and energetic properties observed experimentally in different geometries. The atomic and bond characteristics and parameters from other geometries are transferable because they are parameterized to replicate “ideal” values and remain consistent between similar bonds or functional groups. We can accurately compare these parameters by using the well-established experimental and computational data on biomolecules with similar atomic interactions because in simulations molecules will attempt to replicate ideal bond length and angles by adopting geometries and structures as similar as possible to these values. The forcefields are important to this function because they can describe the behaviours of atoms depending on their environment. For example, carbon atoms in C–H bonds can often be treated as having approximately constant properties, unless they have other atoms or functional groups nearby that can influence or modify the C-H bonds (7,8), allowing differences in hybridization, polarity, and bonding to be captured. This principle of transferability enables molecular mechanics to be broadly applied, from small organic molecules to large biomolecular systems, while retaining computational efficiency.

2.1.2 AMBER Forcefields and CpHMD

MM methods are most helpful for predicting properties for groups of molecules that contain many atoms because they often contain commonly found species like

hydrogen and nitrogen in peptide linkages. Since enough information is already available on those atoms—obtained from prior crystallised molecules or modelled at high-level QM—to perform calculations for their behaviour in simulations accurately. However, there is a shortage of parameters for specific molecules like synthetic compounds or metal-containing complexes. Regardless of this limitation, different families of force fields have been developed for various biomolecular systems, such as AMBER (9), CHARMM (2), GROMOS, OPLS (10), and UFF (11).

AMBER (Assisted Model Building with Energy Refinement) (12) is a software package that includes a suite of biomolecular forcefields. The AMBER package incorporates several tools that provide a unified workflow for parameterisation, MD simulation, and post-completion trajectory analysis, making it especially well-suited for modelling proteins, nucleic acids, and complex biomolecular assemblies. For the purpose of this research, the forcefield used is AMBERff10, offering an update to protein force field ff99SB, which was limited in accuracy regarding rotamer preferences, incorporating improved parameters for protein backbone torsion angles (ϕ and ψ) and refined side-chain torsions (13). This allows the ff10 forcefield to better capture secondary structure stability and folding dynamics in proteins. Unlike ff99SB, ff10 forcefield is also compatible with the constant pH molecular dynamics (CpHMD), capable of performing simulations with dynamic protonation states of titratable residues (e.g., Asp, Glu, His, Lys, and Cys) that standard MD assumes fixed. Here, ‘compatible’ refers to the fact that AMBER’s CpHMD framework has validated titration-state parameters and pKa calibration for ff10, whereas ff99SB is an older fixed-charge protein force field not typically benchmarked as the default for CpHMD workflows. This extends the accuracy of analyses performed from simulations where pH plays a central role and is achieved by coupling MD with Monte Carlo sampling of protonation states, guided by empirical pKa values and the electrostatic environment. Despite later AMBER force fields like ff14SB having since been developed with updated torsion parameters and a wider data set amongst other improvements, ff10 is used in this work for its reliability and historical consistency with earlier studies of amyloid–amylin dimers and CpHMD directed simulations (14).

2.1.3 Geometry Optimization and MD Calculations

In molecular mechanics, geometry optimisation plays a central role and involves computationally refining molecular structures until they reach stable, low-energy

conformations. This is important for the simplified force-field model to be able to reproduce molecular geometries that correspond to experimentally observable states. Optimized structures usually represent minima on potential energy surfaces (PES), which map the relationship between molecular conformations and their energies by plotting nuclear positions as a function of their associated energies, with variations in bond lengths, angles, and torsional angles across the surface (15). However, the local minimum does not necessarily mean the most stable configuration. Further conformational searches are required to explore multiple minima, which generates a more complete view of the PES and the accessible molecular geometries (6). In molecular mechanics, this broader sampling method improves the accuracy of structure-energy predictions and provides realistic starting points for molecular dynamics simulations. These stationary points, particularly minima, are determined computationally from the first derivative of the total energy function (Equation 2.1) with respect to nuclear coordinates.

Beyond static optimization, the deterministic method of MD simulations enables the study of molecular motion over time. MD follows Newton's second law, meaning that given the initial conditions, the positions of particles can be predicted at any time (t). Particle interactions can be expressed as potential energy (V) with the corresponding forces (F) obtained as its derivatives with respect to atomic positions (r), allowing trajectories to be generated by integrating the equations of motion and acceleration (16), as noted in Equation 2.2. By applying this framework iteratively across many time steps, MD generates trajectories that reveal the structural and dynamical evolution of molecular systems (8).

A) $$F = ma$$

B) $$F = -\left(\frac{\partial v}{\partial r}\right) = m\left(\frac{\partial^2 r}{\partial t^2}\right)$$

Equation 2.2 A) Newton's second law of motion describes how the force acting on a particle relates to its mass (*m*) and acceleration (*a*). **B)** The expression of force in terms of the surface potential energy connects the force to the derivative of the potential energy (*v*) with respect to atomic positions (*r*). This formulation is equivalent to the second derivative of position with respect to time, showing how trajectories in MD are obtained by integrating Newton's equations of motion.

2.1.4 Solvation of a System

To best replicate naturally existing conditions of biomolecules, a solvation model that encloses the solute in a 3-dimensional structure (i.e., a cube, octahedron, or sphere), of an explicitly defined solvent can be implemented into simulations. Rigid water models use electrostatic interactions based on Coulomb's Law, as well as repulsion and dispersion forces from the Lennard-Jones (LJ) potential mentioned earlier, to model water as a solvent for the system. TIP3P (transferable intermolecular potential with 3 points) and OPC (Optimal Point Charge) are such explicit solvation models that can be employed in the simulation of biomolecules. Since TIP3P is a 3-point model, it has partial charges located on three atomic centres – 1 Oxygen (O) and 2 Hydrogen (H) atoms, with its LJ interaction site on the oxygen. TIP3P is widely used for legacy force-field compatibility, though it shows measurable deviations from experiment in properties such as the dielectric constant and transport behaviour (17). By contrast, the OPC (Optimal Point Charge) method is constructed as a 4-point model, with three optimized charges (2 positive and 1 negative) and an LJ site (18). The LJ site and the negative charge are separated due to an introduction of an off-nucleus virtual or dummy "M" site, with the LJ interaction on the oxygen and charges distributed between the M site and the two hydrogens; this parametrization reproduces liquid-phase multipole moments and bulk properties (density, dielectric constant, hydration free energies) more accurately than TIP3P, at a slightly higher computational cost.

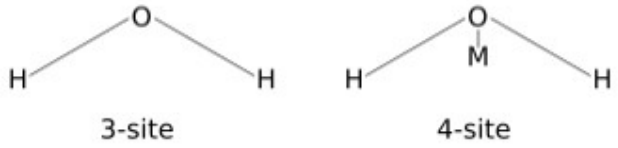

Figure 2.1 Illustration of 3-site (TIP3P) water model and a 4-site (OPC) water model.

While there are many benefits of running MM and MD calculations in explicit solvent, improved accuracy being chief amongst them, the downside is the greater computational cost for large molecules or dimer simulations which will increase depending on the level of solvation applied because the solvent must explore enough degrees of freedom for the results to be trustworthy. Additionally, explicit solvation has been shown to affect conformers of extended peptides studied via MD (19).

To reduce the computational cost, implicit solvent models can replace explicit solvent molecules by a dielectric medium that surrounds the cavity containing the solute. Implicit simulations approximate the effect of the solvent on the solute using a mathematical continuum model, rather than explicitly simulating individual solvent molecules as noted in Figure 2.2. Implicit models approximate the polar (electrostatic) component of solvation and add empirical terms for nonpolar contributions (20). The free energy of solvation of a given system can be expressed in terms of free energy changes as seen in Equation 2.3, including the energies associated with creating a cavity within the solvent, as well as electronic, dispersion and exchange interactions between solvent and solute.

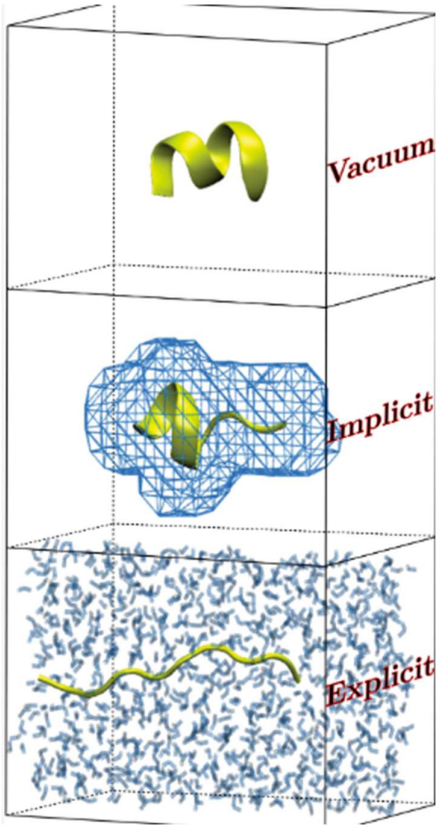

Figure 2.2 Comparisons between a peptide in a Vacuum, Implicit solvent model and Explicit solvent model. Reproduced from Bereau HR *et al*., PLUS ONE, 2015, licensed under CC BY 4.0 (46).

$$\Delta G_{solvation} = \Delta G_{cavity} + \Delta G_{electronic} + \Delta G_{dispersion} + \Delta G_{exchange}$$

Equation 2.3. Thermodynamic decomposition of solvation free energy ($\Delta G_{solvation}$) highlights how it is the sum of ΔG_{cavity} - the energy needed to push solvent molecules to make a cavity

for solutes; $\Delta G_{electronic}$ - the charge-solvent interactions or polarization energy; $\Delta G_{dispersion}$ - the attractive van der Waals interactions between solute and solvent; and $\Delta G_{exchange}$ - the short-range repulsive forces that prevent overlap of solute and solvent electron densities.

A widely used implicit approach for biomolecular simulations is the Generalized Born Surface Area (GBSA) family of methods (21–23). GBSA is an algorithm designed to approximate the electrostatic polarization (the $\Delta G_{electronic}$ term) using analytically convenient expressions that depend on effective Born radii, interatomic distances and atomic volumes; a surface-area term (SA) is commonly added to estimate nonpolar cavity/dispersion contributions. GBSA is computationally inexpensive and therefore well suited to rapid conformational sampling and MM/MD rescoring (e.g., MM/GBSA binding free-energy protocols). However, its accuracy depends strongly on parameter choices and the quality of the effective radii, and it can be less reliable for systems where long-range electrostatics, ion screening, or specific solvent-mediated interactions are important. In particular, because solvent is treated as a continuum rather than discrete water molecules, implicit models may over-stabilize charged contacts (e.g., salt bridges or metal–ligand interactions) and may not fully capture water-bridged hydrogen-bond networks or dielectric heterogeneity at binding interfaces, which can lead to over-binding or altered aggregation propensities in highly charged peptide systems. For constant-pH simulations in AMBER22, maintaining a stable pH-dependent electrostatic environment also requires careful selection of the GB model and associated settings, as these choices directly influence the protonation equilibria and the balance between electrostatic and nonpolar contributions.

2.1.5 Advantages and Disadvantages of MM

Molecular mechanics is a widely used approach for modelling large bioinorganic systems. An advantage of MM is that it is significantly faster than quantum mechanical (QM) methods because it avoids explicitly treating electronic motion, lowering computational expense. Additionally, force fields rely on the transferability of parameters: atoms are grouped into atom types defined by their local bonding environment, so parameters fitted once for common functional groups (e.g., peptide amide bonds, methyl groups, aromatic rings) can be reused across many different molecules. This is what allows previously studied structures and validated parameter sets to be applied to new but chemically similar biomolecules, providing a practical

starting point for simulations—while also highlighting why unusual chemistries such as metal coordination often require specialized parameterization. Despite these advantages, MM also has several limitations. One major limitation is that its accuracy is heavily dependent on the availability of experimental or high-level theoretical data, and simulations can be biased based on the choice of initial geometry, *e.g.* a structure initialized in a square planar configuration may maintain this geometry even if experimental evidence suggests a tetrahedral preference. MM calculations are also limited in which force fields they can use for specific molecules under study ; no single force field is universally applicable (24,25). MM is also generally unsuitable for modelling chemical reactions involving bond formation or breaking, as the methods are limited to nuclear descriptors of ground-state systems; although specialized approaches such as ReaxFF and the Empirical Valence Bond methods exist, QM methods remain preferred for such reactive interactions (26). Finally, systems containing transition metals pose their own challenges, such as d-orbital interactions not being typically accounted for in conventional forcefields, introducing further complexity into MM simulations.

2.1.6 Modelling Transition-metal (Zn(II)) Complexes using MM

Modelling transition metals is complicated and requires many parameters to achieve accurate FF parameterisation. The more complicated shapes of d-orbitals (and even f-orbitals) lead to more complex modes of bonding and geometries, especially when considering their variable oxidation states. Electronic spin can be collectively described as either high- or low-spin states with different properties but at relatively similar energies. Jahn-Teller distortions add to the difficulty in modelling these structures using classical methods, and these factors make the transferability of bond parameters less feasible than for organic structures (31). Yet this does not preclude the use of classical bonded models for sampling, particularly when the coordination environment remains intact and long-timescale conformational dynamics are of interest. A further advantage in this research is that the singular metal to be analysed, Zn(II), does not have the ligand field and spin-state complications, nor does it undergo Jahn–Teller distortions as other transition metals due to its closed d^{10} configuration. It has also been extensively parameterized for classical simulations due to its preference for stable tetrahedral/octahedral

coordination geometries and has a fixed oxidation state of +2, so there is enough data to ensure reliability in the results (27–29).

2.2 Fundamentals of Molecular Dynamics

MD simulations propagate atomic motion by numerically solving Newton's equations of motion under the forces defined by the molecular mechanics potential, over a time-dependent series to find accessible structures at a given temperature. It provides a viable method for simulating large-scale biological interactions, i.e. dissociation/association and protein folding, in addition to local interactions and movements of individual atoms or sidechains. The scope to simulate varying sized structures *via* MD allows study of macroscopic systems at a molecular level. From the first MD simulation, performed by Alder *&* Wainwright (30,31) to the breakthrough that allowed Stillinger *&* Rahman (32) to model liquid water and McCammon *et al.* (33) to carry out the first protein simulation on Bovine Pancreatic Trypsin Inhibitor, molecular dynamics has rapidly evolved into a powerful tool for studying complex molecular systems.

MD is particularly valuable for conformational analysis, enabling efficient screening of candidate structures prior to experimental validation. When combined with MM energy evaluations, MD can probe biomolecular processes such as protein folding at reduced computational cost relative to quantum methods. System complexity scales with size, as non-linear molecules possess 3*N*-6 degrees of freedom (where N is the number of atoms) (6,15,34,35). Conformational sampling strategies include random perturbation of Cartesian coordinates or rotation of torsional angles.

2.2.1 Equations of Motion and Numerical Integration

MD describes the trajectory of particles and the forces acting upon them under time progression by using Newton's equations of motion as seen in Equation 2.4. Because these equations cannot be solved analytically for complex systems, numerical integration schemes such as the Verlet algorithm and its variants are employed to discretize time into finite steps, and to predict new atom positions and velocities at the end of each step (36). This allows MD to predict the coordinates and velocities of molecules either before or after the relative starting point.

$$F_i(t) = m_i \frac{d^2 r_i(t)}{dt^2}$$

Equation 2.4 Newton's equation of motion for a particle i, where i is the atom, $r_i(t)$ is the position vectors of $x_i(t)$, $y_i(t)$, and $z_i(t)$ for the particle i, m_i is the mass of the particle in motion, F_i, is the force acting on particle i, and t corresponds to the time across which the particle is simulated.

2.2.2 Evolution of Time-Series and Conformational Ensembles

At each point in a simulation, the multi-dimensional representation of the momentum and the position of each particle is described by phase space. The phase space of a single particle, μ-space, is 6-dimensional (3 coordinates and 3 momenta) and is defined relative to their positions to others. The phase space of the entire system is referred to as Γ-space and is constructed as the direct product of all individual μ-spaces. To ensure sufficient exploration of the conformational space, a suitable timestep integration is selected during setup. The timestep integration is based on the mobility of a system and vibrational energies of the flexible structures present. Smaller timesteps may increase the accuracy of the simulation, but it will also limit the sampling ability of the simulation because the phase space will not be explored at relevant timescale because far more steps would be required. Meanwhile, larger timesteps would resolve this at the cost of unstable trajectories due to high-energy interactions between particles causing unresolved high-frequency vibrations.

Usually, initial velocities are assigned from the Maxwell–Boltzmann distribution, which specifies the equilibrium distribution of particle velocities at a given temperature. In practice, each Cartesian component of an atom's velocity (vx, vy, vz) is drawn from a Gaussian (normal) distribution with mean zero and a variance that depends on the atom's mass and the target temperature, so heavier atoms are initialized with lower typical speeds than lighter atoms. This enforces equipartition at the start: on average, each translational degree of freedom contributes $\frac{1}{2}k_BT$ to the kinetic energy, and the total kinetic energy across the system corresponds to the desired temperature T. After assignment, most MD engines also apply a centre-of-mass momentum removal step, so the net linear momentum of the system is ~0, preventing unphysical drift of the entire simulation box; some protocols also rescale velocities, so the instantaneous kinetic temperature matches the target temperature

exactly. Because MD time evolution is deterministic for a fixed force field and integration scheme, changing the random seed used for this Maxwell–Boltzmann velocity draw is the standard way to generate independent replicas: even with identical coordinates, different initial momenta lead the system to explore different dynamical pathways and can improve ensemble sampling. Finally, the simulations must be equilibrated; the initial section of a trajectory is strongly influenced by the starting coordinates and velocity assignment and is therefore discarded. Post-trajectory analysis can be used to identify when key observables have stabilized before collecting meaningful data. Alternatively, the endpoint of an equilibrated run can be used to start subsequent simulations to reduce bias from the initial geometry, provided those follow-on runs are treated as continuations rather than statistically independent replicates (37–39).

During MD, the sequence of structures sampled, as denoted in the output trajectory and coordinate files, can be considered as a thermodynamic ensemble. The modelling procedure is typically performed under specific thermodynamic conditions defined by statistical ensembles, in which key variables such as temperature (T), pressure (P), volume (V), or energy (IeI) are maintained (40). For example, in canonical ensemble (NVT), the number of atoms, volume, and temperature remain constant, while in microcanonical ensembles (NVE) the total system energy is conserved but the temperature fluctuates in accordance with the system evolution over the given timescale.

$$p_i = \frac{1}{Z} \exp\left(-\frac{\varepsilon_i}{k_B T}\right)$$

Equation 2.5 Probability equation for state of energy (εi) a system occupies using the Boltzmann distribution, where T is temperature, k_B is the Boltzmann constant, and Z is the partition function.

Equation 2.5 highlights how lower-energy states are more frequently sampled than higher-energy ones. At physiological temperature (310 K), the distribution governs the likelihood of visiting high-energy intermediates and transition states. According to the ergodic hypothesis, shown in Equation 2.6, time averages can approximate ensemble averages if sampling is sufficient; in practice, achieving adequate sampling can be challenging for biomolecules due to kinetic trapping.

:

$$\langle A \rangle_{ensemble} = \langle A \rangle_{time}$$

Equation 2.6 Equation Representing ergodic hypothesis. A time average of a system's quantity of a particle (energy/pressure/density/charge) over a long enough time will be equal to the average of all ensembles/energy of that system at the same time.

In practice, however, MD simulations involve far fewer particles than experimental systems. Yet, with adequate sampling, statistically meaningful averages can still be obtained; however, there is debate over what is “sufficient sampling” (41).

2.2.3 Limitations of MD

By using molecular mechanics (MM) for energy evaluation, calculations are generally rapid, and parameterisation of drugs, cofactors, metal centres *etc.* extends its applicability to complex systems. Compared with quantum mechanical (QM) methods, MD using forcefields is far less computationally demanding and can therefore be applied to larger systems and longer timescales. However, MD also has important limitations. While simulations for larger structures and longer timescales are computationally cheap compared to QM, an increase in system size or simulation time can still cause computational costs to become significant. While MD provides a powerful means of sampling ensembles under controlled thermodynamic conditions, its accuracy is constrained by its reliance on the approximations from the parameters provided by the empirical force field methods. These approximations can limit the reliability of the results, particularly when modelling systems with complex interactions beyond the scope of the chosen force field. Another challenge is conformational sampling: MD explores the potential energy surface through time-dependent evolution, but the transitions between local minima can become hindered when the energy barriers separating them are higher than the thermal energy defined at the simulation temperature. Thus, the system lacks sufficient energy to explore new conformational space and instead becomes confined within that energy basin, producing repeated sampling of similar structures over extended timescales (42). In principle, sufficiently long simulations would overcome these barriers, but such timescales are unrealistic for the biomolecular systems. Increasing the temperature can provide additional energy to accelerate barrier crossing, but this can distort the conformational ensemble by overpopulating non-physiological states. A

more controlled alternative is to use replica-exchange methods (e.g., temperature REMD or solute tempering/REST2), where higher-temperature (or selectively "heated") replicas help the system cross barriers while exchanges allow sampling at the target temperature. Another route is metadynamics, which applies a history-dependent bias along chosen collective variables to accelerate transitions between metastable states and recover the underlying free-energy surface. Both approaches can reduce trapping in local minima more effectively than simple heating, but they add computational cost and require careful choices of replica setup or collective variables and reweighting.

2.2.4 Introduction to MM-GBSA

MM-GBSA (Molecular Mechanics Generalized Born Surface Area) is a computational method widely used to estimate binding free energies (ΔG_{bind}) of ligands bound to biomolecular receptors, though it can also be applied to larger intermolecular recognition problems. Using the expressions from Srinivasan *et al.* and Kollman *et al.* (43,44), Equation 2.7 illustrates how MM-GBSA approximates the binding free energy in aqueous solution ($\Delta G_{bind,aq}$).

$$\Delta G_{bind,aq} = \Delta H - T\Delta S \approx \Delta E_{MM} + \Delta G_{solv} - T\Delta S$$

Equation 2.7. Gibbs free energy for aqueous solution estimation equation. The total free energy of binding ($\Delta G_{bind,aq}$) is approximated by the sum of the molecular mechanics energy change (ΔE_{MM}) and the solvation free energy change (ΔG_{solv}), minus the entropic contribution ($T\Delta S$). ΔE_{MM} accounts for covalent, electrostatic, and van der Waals interactions, while ΔG_{solv} includes both polar and non-polar solvation effects. The entropic term reflects the loss of conformational, rotational, translational, and other degrees of freedom upon binding. Together, these terms provide an efficient framework for approximating ligand–receptor binding affinities.

The components presented in Equation 2.7 are computed *via* ensemble averaging over many snapshots drawn from molecular dynamics simulations. The solvation term is handled implicitly, and in MM-GBSA, this is achieved using Generalized Born (GB) models, which offer a computationally less expensive but still reliable alternative to the Poisson–Boltzmann (PB) approach (45). In this work, MM-GBSA will be applied to estimate the binding free energies of Aβ and amylin complexes,

providing insight into how pH effects influence early nucleation and aggregation processes relevant to Alzheimer’s disease.

2.3 REFERENCES

1. Atavin EG, Mastryukov VS, Allinger NL, Almenningen A, Seip R. Molecular structure of cyclododecane, C12H24, as determined by electron diffraction and molecular mechanics. J Mol Struct. 1989 Sept 1;212:87–95.

2. Brooks BR, Bruccoleri RE, Olafson BD, States DJ, Swaminathan S, Karplus M. CHARMM: A program for macromolecular energy, minimization, and dynamics calculations. J Comput Chem. 1983;4(2):187–217.

3. Weiner PK, Kollman PA. AMBER: Assisted model building with energy refinement. A general program for modeling molecules and their interactions. J Comput Chem. 1981;2(3):287–303.

4. Weiner SJ, Kollman PA, Nguyen DT, Case DA. An all atom force field for simulations of proteins and nucleic acids. J Comput Chem. 1986;7(2):230–52.

5. Mayo SL, Olafson BD, Goddard WA. DREIDING: a generic force field for molecular simulations. J Phys Chem. 1990 Dec 1;94(26):8897–909.

6. Jensen F. Introduction to Computational Chemistry. Newark: Wiley; 2017. 662 p.

7. Levitt M. Molecular dynamics of native protein. I. Computer simulation of trajectories. J Mol Biol. 1983 Aug 15;168(3):595–617.

8. Karplus M, Petsko GA. Molecular dynamics simulations in biology. Nature. 1990 Oct;347(6294):631–9.

9. AMBER, a package of computer programs for applying molecular mechanics, normal mode analysis, molecular dynamics and free energy calculations to simulate the structural and energetic properties of molecules. Comput Phys Commun. 1995 Sept 2;91(1–3):1–41.

10. Jorgensen WL, Tirado-Rives J. ACS Publications. American Chemical Society; 1988 [cited 2025 Sept 27]. The OPLS [optimized potentials for liquid simulations] potential functions for proteins, energy minimizations for crystals of cyclic peptides and crambin. Available from: https://pubs.acs.org/doi/abs/10.1021/ja00214a001

11. Rappe AK, Casewit CJ, Colwell KS, III WAG, Skiff WM. ACS Publications. American Chemical Society; 2002 [cited 2025 Sept 27]. UFF, a full periodic table force field for molecular mechanics and molecular dynamics simulations. Available from: https://pubs.acs.org/doi/abs/10.1021/ja00051a040

12. Case DA, Cheatham III TE, Darden T, Gohlke H, Luo R, Merz Jr. KM, *et al.* The Amber biomolecular simulation programs. J Comput Chem. 2005 Dec 1;26(16):1668–88.

13. Swails JM, York DM, Roitberg AE. Constant pH Replica Exchange Molecular Dynamics in Explicit Solvent Using Discrete Protonation States: Implementation, Testing, and Validation. J Chem Theory Comput. 2014 Mar 11;10(3):1341–52.

14. Maier JA, Martinez C, Kasavajhala K, Wickstrom L, Hauser KE, Simmerling C. ACS Publications. American Chemical Society; 2015 [cited 2025 Sept 27]. ff14SB: Improving the Accuracy of Protein Side Chain and Backbone Parameters from ff99SB. Available from: https://pubs.acs.org/doi/full/10.1021/acs.jctc.5b00255

15. Leach AR. Molecular Modelling: Principles and Applications. Pearson Education; 2001. 788 p.

16. Frenkel D, Smit B, Ratner MA. Understanding Molecular Simulation: From Algorithms to Applications. Phys Today. 1997 July 1;50(7):66–66.

17. Jorgensen WL, Chandrasekhar J, Madura JD, Impey RW, Klein ML. Comparison of simple potential functions for simulating liquid water. J Chem Phys. 1983 July 15;79(2):926–35.

18. Izadi S, Anandakrishnan R, Onufriev AV. Building Water Models: A Different Approach. J Phys Chem Lett. 2014 Nov 6;5(21):3863–71.

19. Florová P, Sklenovský P, Banáš P, Otyepka M. Explicit Water Models Affect the Specific Solvation and Dynamics of Unfolded Peptides While the Conformational Behavior and Flexibility of Folded Peptides Remain Intact. J Chem Theory Comput. 2010 Nov 9;6(11):3569–79.

20. Genheden S, Ryde U. The MM/PBSA and MM/GBSA methods to estimate ligand-binding affinities. Expert Opin Drug Discov. 2015 May;10(5):449–61.

21. Onufriev AV, Case DA. Generalized Born Implicit Solvent Models for Biomolecules. Annu Rev Biophys. 2019 May 6;48:275–96.

22. Hawkins GD, Cramer CJ, Truhlar DG. Pairwise solute descreening of solute charges from a dielectric medium. Chem Phys Lett. 1995 Nov 17;246(1):122–9.

23. Still WC, Tempczyk A, Hawley RC, Hendrickson T. Semianalytical treatment of solvation for molecular mechanics and dynamics. J Am Chem Soc. 1990 Aug 1;112(16):6127–9.

24. Marshall GR. Limiting Assumptions in Molecular Modeling: Electrostatics. J Comput Aided Mol Des. 2013 Feb;27(2):107–14.

25. Li P, Merz KM. Metal Ion Modeling Using Classical Mechanics. Chem Rev. 2017 Feb 8;117(3):1564–686.

26. Pang YP, Xu K, Yazal JE, Prendergas FG. Successful molecular dynamics simulation of the zinc-bound farnesyltransferase using the cationic dummy atom approach. Protein Sci Publ Protein Soc. 2000 Oct;9(10):1857–65.

27. Yu Z, Li P, Merz KM. Extended Zinc AMBER Force Field (EZAFF). J Chem Theory Comput. 2018 Jan 9;14(1):242–54.

28. Peters MB, Yang Y, Wang B, Füsti-Molnár L, Weaver MN, Merz KM. Structural Survey of Zinc Containing Proteins and the Development of the Zinc AMBER Force Field (ZAFF). J Chem Theory Comput. 2010 Sept 14;6(9):2935–47.

29. Bazayeva M, Giachetti A, Pagliai M, Rosato A. A Comparison of Bonded and Nonbonded Zinc(II) Force Fields with NMR Data. Int J Mol Sci. 2023 Jan;24(6):5440.

30. Alder BJ, Wainwright TE. Studies in Molecular Dynamics. I. General Method. J Chem Phys. 1959 Aug 1;31(2):459–66.

31. Ise N, Sogami IS, editors. Phase Transitions by Computer Simulation. In: Structure Formation in Solution: Ionic Polymers and Colloidal Particles [Internet]. Berlin, Heidelberg: Springer; 2005 [cited 2025 Sept 27]. p. 297–322. Available from: https://doi.org/10.1007/3-540-27715-3_8

32. Stillinger FH, Rahman A. Improved simulation of liquid water by molecular dynamics. J Chem Phys. 1974 Feb 15;60(4):1545–57.

33. McCammon JA, Gelin BR, Karplus M. Dynamics of folded proteins. Nature. 1977 June 16;267(5612):585–90.

34. Adcock SA, McCammon JA. Molecular dynamics: survey of methods for simulating the activity of proteins. Chem Rev. 2006 May;106(5):1589–615.

35. Hollingsworth SA, Dror RO. Molecular Dynamics Simulation for All. Neuron. 2018 Sept 19;99(6):1129–43.

36. Allen MP, Tildesley DJ. Computer Simulation of Liquids [Internet]. Oxford University Press; 2017 [cited 2025 Sept 27]. Available from: https://doi.org/10.1093/oso/9780198803195.001.0001

37. Chodera JD. A simple method for automated equilibration detection in molecular simulations. J Chem Theory Comput. 2016 Apr 12;12(4):1799–805.

38. Gallo MT, Grant BJ, Teodoro ML, Melton J, Cieplak P, Phillips GN, *et al.* Novel procedure for thermal equilibration in molecular dynamics simulation. Mol Simul. 2009 Apr 1;35(5):349–57.

39. Wieczorek G, Niedzialek D. Molecular Dynamics. In: Encyclopedia of Life Sciences [Internet]. 2020 [cited 2025 Sept 27]. p. 1–18. Available from: https://doi.org/10.1002/9780470015902.a0003048.pub3

40. Durrant JD, McCammon JA. Molecular dynamics simulations and drug discovery. BMC Biol. 2011 Oct 28;9(1):71.

41. Simányi N. Conditional proof of the Boltzmann-Sinai ergodic hypothesis. Invent Math. 2009 Aug 1;177(2):381–413.

42. Poddar S, Eul J, Patzel V. Homologous SV40 RNA trans-splicing: Special case or prime example of viral RNA trans-splicing? Comput Struct Biotechnol J. 2014 June;10(16):51–7.

43. Cheatham TE, Srinivasan J, Case DA, Kollman PA. Molecular dynamics and continuum solvent studies of the stability of polyG-polyC and polyA-polyT DNA duplexes in solution. J Biomol Struct Dyn. 1998 Oct;16(2):265–80.

44. Kollman PA, Massova I, Reyes C, Kuhn B, Huo S, Chong L, *et al.* Calculating structures and free energies of complex molecules: combining molecular mechanics and continuum models. Acc Chem Res. 2000 Dec;33(12):889–97.

45. Wang C, Greene D, Xiao L, Qi R, Luo R. Recent Developments and Applications of the MMPBSA Method. Front Mol Biosci. 2017;4:87.

46. Bureau HR, Merz DR Jr, Hershkovits E, Quirk S, Hernandez R (2015) Constrained Unfolding of a Helical Peptide: Implicit versus Explicit Solvents. PLOS ONE 10(5): e0127034.

Chapter 3: Establishing Simulation Parameters for Amyloid-β

3.1 Introduction

Chapter one highlighted pH's role as a critical modulator of amyloid and amylin peptide behaviour in the Alzheimer's disease hypothesis. Small deviations in pH alter the protonation states of titratable residues like histidine (His), lysine (Lys), aspartate (Asp), and glutamate (Glu), which, in turn, alter the electrostatic balance, hydrogen bonding, and secondary structure of amyloid peptides (1). Most titratable residues in Aβ fall within the N-terminal region (residues 1–16) making it particularly sensitive to pH changes and strongly influencing the earliest nucleation steps of fibrillization. Furthermore, because its interactions are simpler compared to the full peptide—where C-terminal hydrophobic interactions can obscure protonation-driven effects—this truncated sequence is chosen as the starting point of this investigation. Previous studies generally kept a narrow range of pH for exploring the effects on amyloid or amylin peptide's structures in relation to their functions (2,3). However, in this work simulations of Aβ16 over a pH range of 1 to 10 will be performed through CpHMD, comparing overall structural stability, molecular compactness, and secondary structure transitions using classical (RMSD, Rg, SASA, SecStruct) analytical parameters from AMBER (4). This initial comparative framework will then be extended to Aβ40 and full-length amylin over a more physiologically relevant range of pH 4–9, bridging the works of prior studies like Jha S *et al. (2014)* and Tarus *et al. (2006*) into one coherent pipeline highlighting the trends across the pH span.

Varying pH alters intramolecular hydrogen bonding, salt bridges, and solvent interactions, thereby driving transitions between α- or 3_{10}-helical conformations and β-sheet-rich structures associated with nucleation and fibril growth (1,2). Using conventional MD, which directly integrates Newton's equations of motion on the unmodified potential energy surface, a physically faithful representation of peptide motions can be reproduced and can provide atomistic insights into how environmental protonation states influence aggregation propensity and potential cross-aggregation between amylin and Aβ without requiring reweighting procedures (5–7).

To further refine these simulations, both implicit and explicit model simulations are employed at neutral pH. Lang *et al.* highlight the limitations of GB models in their ability to accurately capture solvent-solute hydrogen-bonding and long-range electrostatics (8). Implicit solvent models enable efficient sampling across large ensembles by approximating solvent effects through continuum representations, while explicit solvent models represent individual water molecules, capture solvation dynamics, and peptide-solvent patterns with higher accuracy, though at a substantially greater computational cost (9). By applying both approaches in parallel, a framework for accurately and efficiently evaluating structural heterogeneity and solvent treatment on pH-dependent Aβ16 can be established. Computational studies have suggested that N-termini of Aβ peptides can be effective models for making inferences about interactions and structures of full-length Aβ (10,11). This study provides the basis for determining which solvent model is most appropriate for future CpHMD studies.

3.2 Computational Method

Using the AMBER22 package, an Aβ16 system was set up with appropriate protonation states for physiological pH to investigate the changes in titratable residues like ASP, GLU, HIS, and LYS. The AMBER ff10 forcefield parameter set was used for all these experiments to model the standard amino acid residues, a C-terminal cap (NME) – an amide that effectively mimics a peptide bond, making the terminal environment more like an internal residue, and a positively charged N-terminus (N) to mimic realistic models of parent proteins. The aforementioned titratable residues were also protonated to prepare them for protonation analysis.

A)

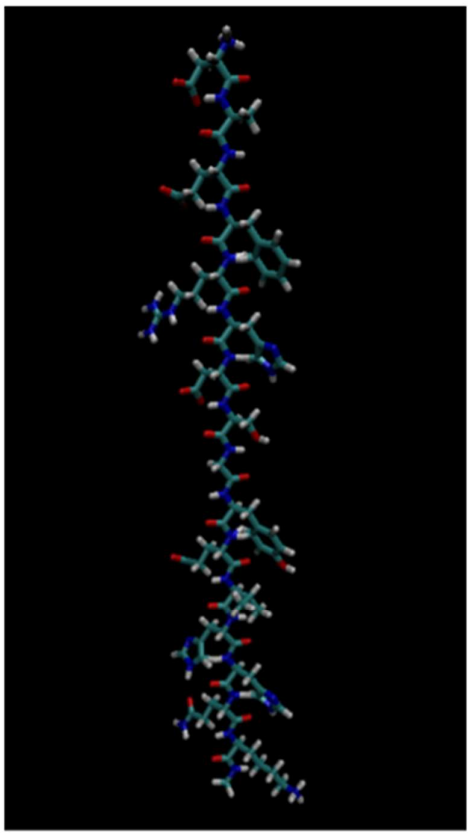

B) NASP ALA GLU PHE ARG HIS ASP SER GLY TYR GLU VAL HIS HIS GLN LYS NME

Figure 3.1. Starting structure of Aβ16, **A)** VMD visualization**. B)** written sequence with titratable residues shown in red.

The constructed peptide in the implicit model was duplicated for an explicit solvent model as well, with an OPC water box chosen for its improvements over TIP3P/4P in reproducing water's dielectric properties and structure, shaped as a truncated octahedron for greater solvent volume efficiency and more uniform isotropic solvation best suited to misfolded, fibrillar Aβ16 structures. Neutralizing and buffering Na/Cl ions were also added to prevent unrealistic charge buildup and to better approximate cellular conditions. These peptides are minimized, heated, and subjected to CpHMD at pH 7 for comparison (similar to the Harris and Shen *et al.* 2019 study).

The molecular dynamics simulation was carried out using the Generalized Born solvation model (igb=2) applied to all topology and coordinate files generated from LEaP with random seed for initial velocities drawn from the Maxwell-Boltzmann distribution at 300 K (ig=-1) (12–16). The SHAKE algorithm (6) was used to constrain

all covalent bonds involving hydrogen atoms, allowing the use of a 2-fs integration timestep. This timestep was chosen to remove high-frequency bond vibrations and works well with the SHAKE algorithm (17). Electrostatic interactions were neglected beyond a cut-off of 999 Å to remove any truncation for CpHMD impacts and a Langevin thermostat was used for stability of the system at 300 K temperature, with all simulations running in the NVT ensemble (fixed temperature). This approach has been reported to enhance conformational sampling of flexible systems in implicit solvent with results comparable to that in explicit solvent (10) as evidenced in Table 3.1. Both simulations were subjected to an initial 20 ns runtime at pH 7 for comparison and later extended to 100 ns to reach a state of pseudo-equilibration with enough simulation space to gain statistically significant data. Block analysis and plateauing of quantitative trajectory metrics like root-mean-square deviation (RMSD) and radius of gyration (Rg) allow determination of the equilibration states and appropriate runtimes, while also providing insight into structural stability and significance to the data acquired. Additional analyses were also pursued to compare titration statistics *via* Cpinutil.py, determine secondary structure (SecStruct) balance *via* CPPTRAJ (18), or highlight structures visually through VMD 1.9.3 (19) as illustrated in Figure 3.3. Through these standard descriptors the effects of pH 7 on the structure, flexibility, and compactness of Aβ16 was investigated. The comparison suggested no significant deviations between implicit and explicit results; thus, the implicit model and the same trajectory analysis were reused for pH 1 to 10 as presented in Tables 1.2 and Figures 3.6-3.8.

After confirming that the peptide at pH 1–3, 9, and 10 showed no realistically relevant comparative data, being almost fully protonated or deprotonated, the following experiments were more focused. Expanding from these results, a comparison experiment was conducted between Aβ40 and amylin peptide at an overall more focused range of pH 4 to 9. To begin, a fully extended geometry of the Aβ40 sequence was created in LEAP, with a carboxyl group at the C-terminus and a positively charged N-terminal (NASP). For amylin, a disulfide bond between Cys2 and Cys7 was included to preserve its native constraint, and the C-terminus was amidated ($–CONH_2$) to remove the negative charge of a free carboxylate, matching the physiological form of the peptide. The N-terminus was kept positively charged to reflect experimentally relevant charge states (Figure 3.2).

After five sequential 20 ns simulations produced a 100 ns run with RMSD and Rg analysis within acceptable values of 5–6 Å, as understood when compared to previous studies (1,20), a further 5 sequential runs of 100 ns totalling 500 ns were performed for pH 7, to start, providing ample conformational space for system pseudo-equilibration. Despite successfully analysing radius of gyration and secondary structure analysis, the titration statistics were incomplete due to partial frame analysis from equilibrated 500 ns. This is likely linked to an incompatibility between constant pH utility (cphstats) and restarting simulations using the pmemd MD engine in AMBER. To amend this technical error, the simulation was repeated for 250 ns in triplicates with random initial velocity running parallel at pH 7 to start. After the RMSD graph showed a convergence, therefore validating the data, the rising phases (50 ns) were removed from each simulation to allow for system stabilization and the plateaued phases (200 ns) were combined, providing a 600 ns range for quantitative analysis including Rg, SecStruct, clustering and titration curves. All analysed data trends, shown in Tables 3.4–3.7 and Figure 3.9-3.14, were consistent with the previous 100 ns experiment, which validated this approach and allowed repetitive comparative analysis for the newly established pH range.

Aβ40

N-ASP ALA GLU PHE ARG HIS ASP SER GLY TYR GLU VAL HIS HIS GLN LYS LEU VAL PHE PHE ALA GLU ASP VAL GLY SER ASN LYS GLY ALA ILE ILE GLY LEU MET VAL GLY GLY VAL VAL

Amylin-37

N-LYS CYX ASN THR ALA THR CYX ALA THR GLN ARG LEU ALA ASN PHE LEU VAL HIS SER SER ASN ASN PHE GLY ALA ILE LEU SER SER THR ASN VAL GLY SER ASN THR TYR-NHE

Figure 3.2. Starting structure of Aβ40 and amylin-37. Titratable residues shown in red and terminal modifications shown in blue.

3.3 Results and Discussion

Root-mean-square displacement of all backbone atoms relative to starting structure was used as the primary measure of equilibration. Expanding from the topic above, the implicit and explicit model comparisons were subjected to 100 ns simulation runtimes with the first 40 ns taken as pre-equilibration phase due to greater

fluctuations from the explicit model. The implicit simulations performed across the range of pH 1 to 10 were also selected for analysis past 40 ns. The more focused pH range that sees a comparison of full-length amylin and Aβ40 across pH 4-8, was analysed past the 50 ns equilibration point. The analysis reported for them is taken from data extracted from frames after these equilibration points.

3.3.1 Comparisons of Aβ16 in Implicit and Explicit Models

The comparative analysis of explicit and implicit CpHMD simulations of Aβ16 at pH 7 shows reliability for implicit solvation to replace explicit. As shown in Figure 3.3, the end-frame visualizations from both simulations exhibit highly similar conformations. Figure 3.4 and Table 3.1 further highlight their similarities with RMSD profiles largely overlapping, and their fluctuations confined to the range of 4–6 Å and their average Rg values differing by only ~0.3 Å. Together, these results suggest that the structural and dynamic properties of $A\beta_{16}$ are negligibly affected by the choice of solvent model, supporting the reliability of implicit solvation as a computationally efficient alternative to explicit CpHMD simulations under these conditions.

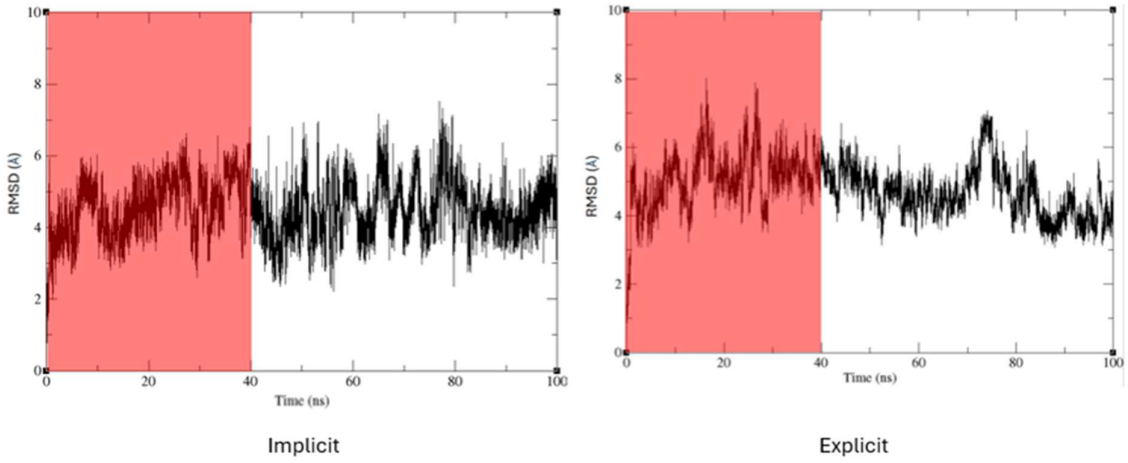

Figure 3.3. RMSD plots from implicit and explicit models across 100ns. Red background denotes the pre-equilibration data that was discarded and white background is the equilibrated data used for subsequent analysis.

	Implicit			Explicit		
pH value	**Rg (Avg)**	**Rg (min)**	**Rg (max)**	**Rg (Avg)**	**Rg (min)**	**Rg (max)**
pH 7	9.13 ± 1.3	7.1	14.6	9.43 ± 1.4	7.4	15.2

Table 3.1. Rate of gyration values of Aβ16 structure at pH 7.

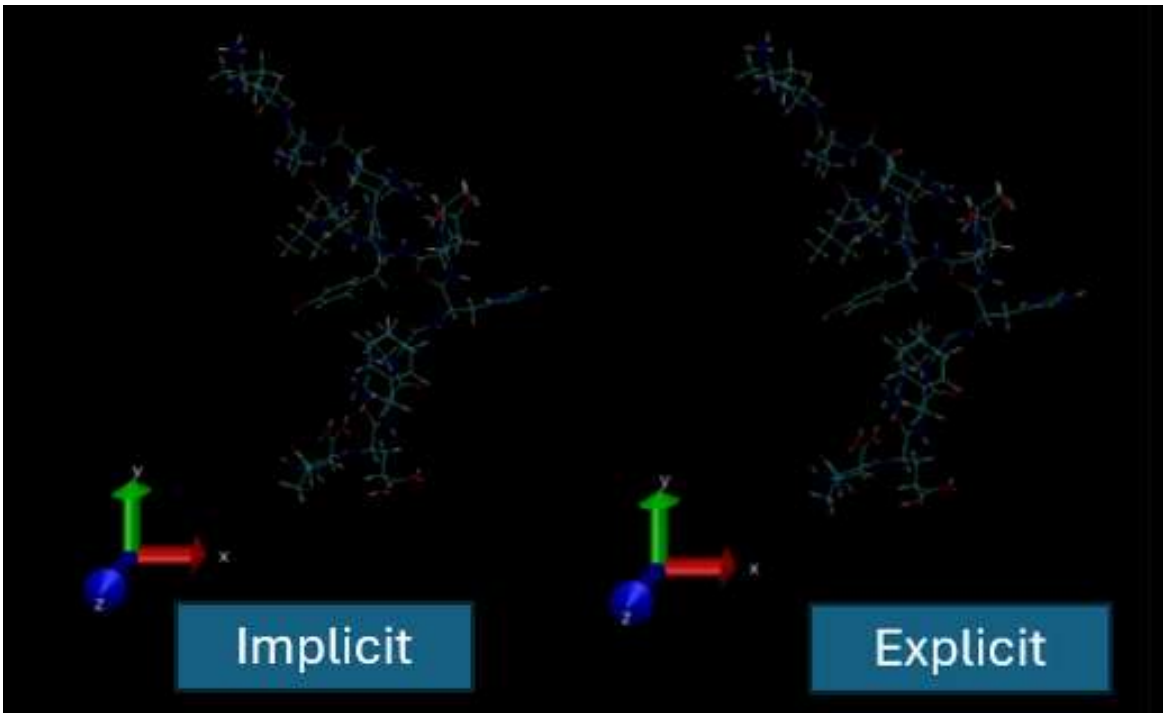

Figure 3.4. VMD visualization of end frame structures of *Aβ16* after 100 ns, in implicit and explicit models.

The titration-trajectory graphs in Figure 3.5 further highlight the consistency between implicit and explicit simulations. Both models show dynamic protonation behaviour for histidine residues over the 60 ns runtime, with implicit simulations exhibiting protonation probability fluctuations of 0.2 Å, while explicit simulations display slightly wider fluctuations of approximately 0.3 Å over the span of post-equilibrated 60 ns. Aspartate and glutamate residues in the explicit model also fluctuate modestly; however, their median protonation probabilities remain below 0.1, indicating that these variations are negligible. The comparatively greater dynamic behavior for the three histidine residues suggests they are more involved in pH-sensitive interactions, which may be crucial for understanding functional mechanisms in proteins. Given that the explicit simulations reproduced these results at roughly fifteen times the computational cost of the implicit model, all subsequent simulations were performed using the more computationally efficient implicit approach.

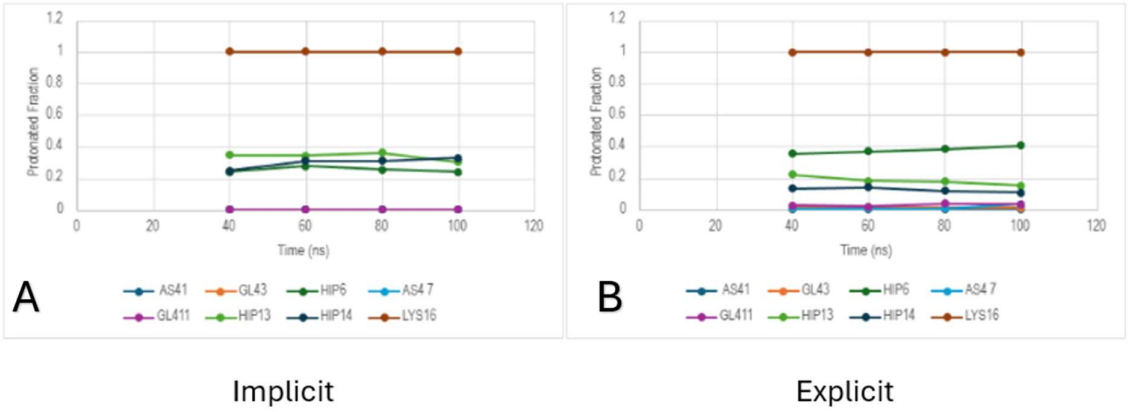

Figure 3.5. Protonated fraction vs. time graphs for Implicit (A) and Explicit (B).

3.3.2 Comparisons of Aβ16 Structural Stability and Conformational Dynamics in pH 1 to 10

Backbone RMSD relative to an initial minimized structure over a combined 100 ns of CpHMD simulation displays reaching a plateau after initial rise at 5 ns in Figure 3.6. Closer inspection indicates that the peptide experiences greater and more frequent transitions at pH 2, varying between approx. 4 and 10 Å. Similarly frequent transitions also appear at pH 1, 3, and 9, with RMSD values fluctuate between approximately 3–9 Å, whereas near-neutral pH values 5–8 display more restrained fluctuations of 4.5–7 Å, indicating greater structural stability. Consistent with these observations, mean Rg values in Table 3.2 reveals the most flexible structures appear only in pH 1-3 and 9, with Rg means ranging from 9.4-11.9 Å and pH 2 showing the largest value of 11.9 Å likely due to its transient variance at 60 ns indicating greater structural drift. The associated standard deviations reinforce this: pH 2 also shows the largest spread (±1.8 Å), indicating a highly heterogeneous ensemble that frequently switches between compact and extended states, while the smaller SDs at near-neutral pH (e.g., pH 6 and 8 at ±0.8 Å) reflect tighter clustering around the mean and more reproducible compactness. Meanwhile, neutral pH values of 5-8 yield slightly more compact structures with their Rg values ranging within 8.8-9.1 Å, though the still greater values are likely due to the lack of C-terminal hydrophobic regions directing the peptide towards a collapsed β-rich structure. These results suggest a clear correlation between pH and peptide stability, with extreme acidic or basic environments promoting structural flexibility and near-neutral pH favouring a compact and stable conformation of Aβ16.

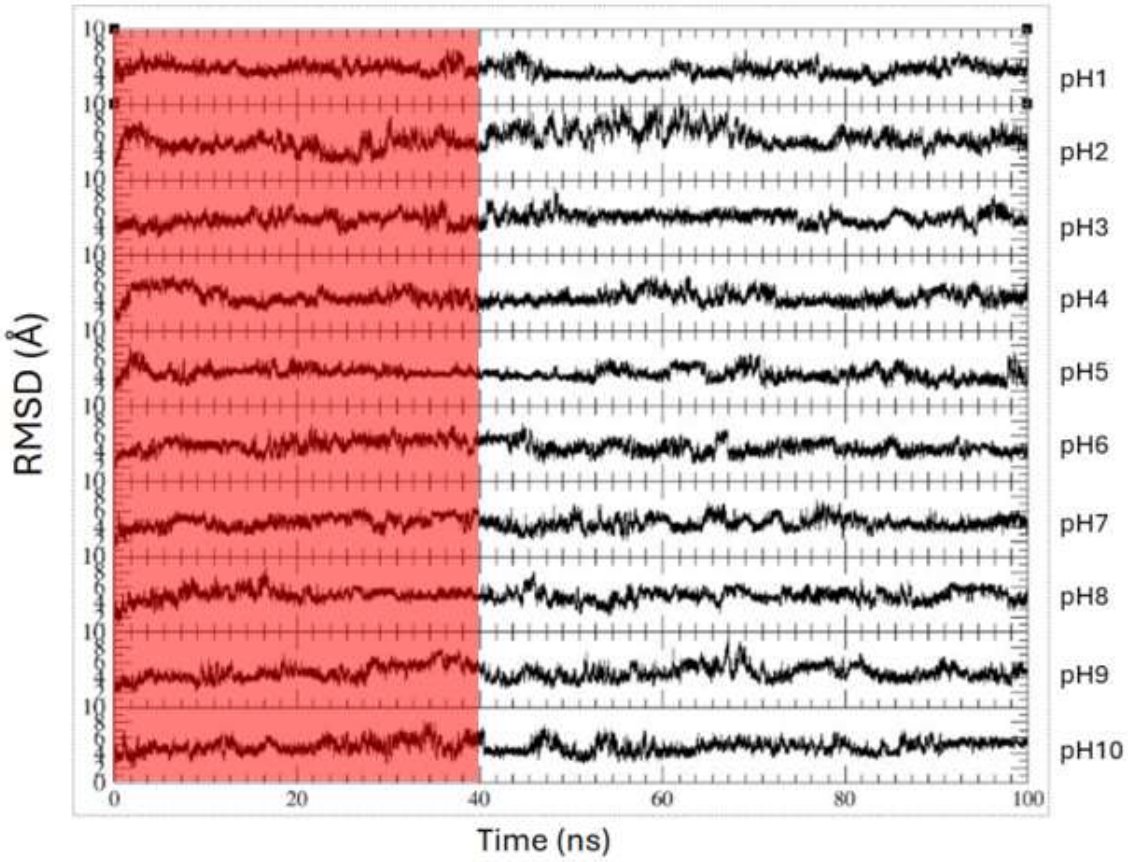

Figure 3.6. Backbone RMSD of free Aβ16 across 100 ns and 1-10 pH environments. Red background denotes the pre-equilibration data.

Table 3.2 Statistical data for Rg (Å) of CpHMD 100 ns simulations.

pH value	Rg (Avg)	Rg (SD)
pH1	9.4	1.1
pH2	11.9	1.8
pH3	10.1	1.1
pH4	9.1	1.1
pH5	8.8	1.0
pH6	8.8	0.8
pH7	9.1	1.3
pH8	8.5	0.8
pH9	9.4	1.4

pH10	9.0	1.3

Secondary structural analysis of Aβ16 reveals a predominance of helical conformations (α-helix and 3_{10}-helix) with minimal β-sheet content. The C-terminal capped residues exhibit a reduced propensity to maintain α-helical structure relative to residues 3–6 and 9–14. Under both strongly acidic conditions of pH 1-3 and basic conditions of pH 8-10, the peptide is largely unstructured, predominated by turn and bend motifs. Highly acidic environments result in most titratable residues having a net positive charge and strong electrostatic repulsion between neighbouring residues, destabilizing intra-peptide hydrogen bonding and preventing more stable structured motifs from arising. Stability is assessed by lower RMSD and Rg fluctuations (SD values) and persistence of same values across different blocks in the same simulation which has not been reported due to efficiency (showcasing the equilibrated values that persist within the SD range is considered appropriate enough). Conversely, under highly basic environments acidic residues become deprotonated, and the peptide carries a net negative charge which also causes electrostatic repulsions among the charged side chains and disrupts the stabilizing salt bridges, again promoting flexibility and unstructured conformations. Moderately acidic to neutral conditions like pH 4–7 show increased helical content, with peaks around residues Glu3, Glu11, and His13–14, suggesting that partial deprotonation stabilizes local helical motifs. The trends of each group are captured in Figure 3.7 and may differ from full-length Aβ peptides, which often display higher β-sheet propensity, particularly in the C-terminal region, as the additional residues provide longer-range interactions and hydrophobic contacts that facilitate β-strand formation. Consequently, while Aβ16 captures the pH-sensitive dynamics of the N-terminal region, its conformational landscape is inherently more helical and less β-rich than the full-length peptide, highlighting the importance of sequence context and length in determining amyloidogenic potential.

Trends of clustering analysis presented in Table 3.3 also reinforce the observations from SecStruct, RMSD, and Rg analysis. Highly populated clusters of Aβ16 from the previous 100 ns runs propagate 21-28% sizes at pH 4-7 with pH 7 being the most populated indicating a uniform single-basin ensemble, which corresponds to low

RMSD and Rg values and the more ordered secondary structures indicating presence of stable peptide.

In contrast, peptides in extreme acidic or basic conditions like pH 2 that exhibits some of the larger RMSD and Rg values with minimal secondary structure, also forms the least populated cluster <20%, reflecting a preference for highly flexible, unstructured states, consistent with greater conformational heterogeneity. This convergence of clustering, RMSD, Rg, and secondary structure trends strengthens confidence in the validity of the observed pH-dependent conformational behaviour of Aβ16.

Table 3.3 Highest proportion of population cluster for Aβ16 per pH value.

pH value	Population size (%)
pH1	16
pH2	14
pH3	19
pH4	23
pH5	21
pH6	25
pH7	28
pH8	16
pH9	24
pH10	17

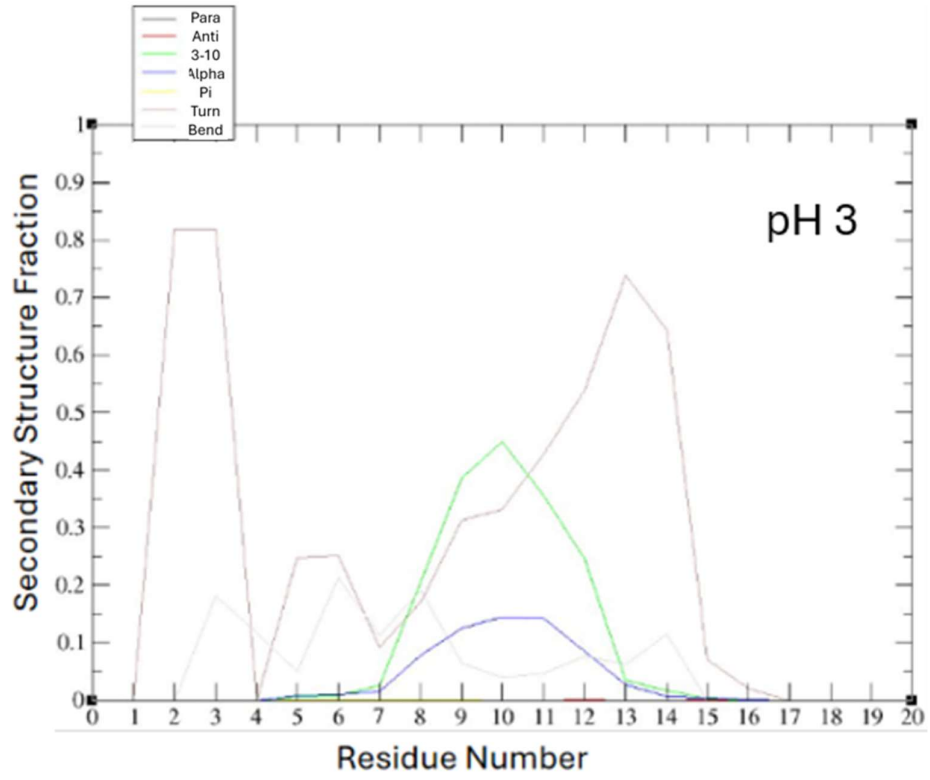
Para
Anti
3-10
Alpha
Pi
Turn
Bend
pH 3
Secondary Structure Fraction
Residue Number

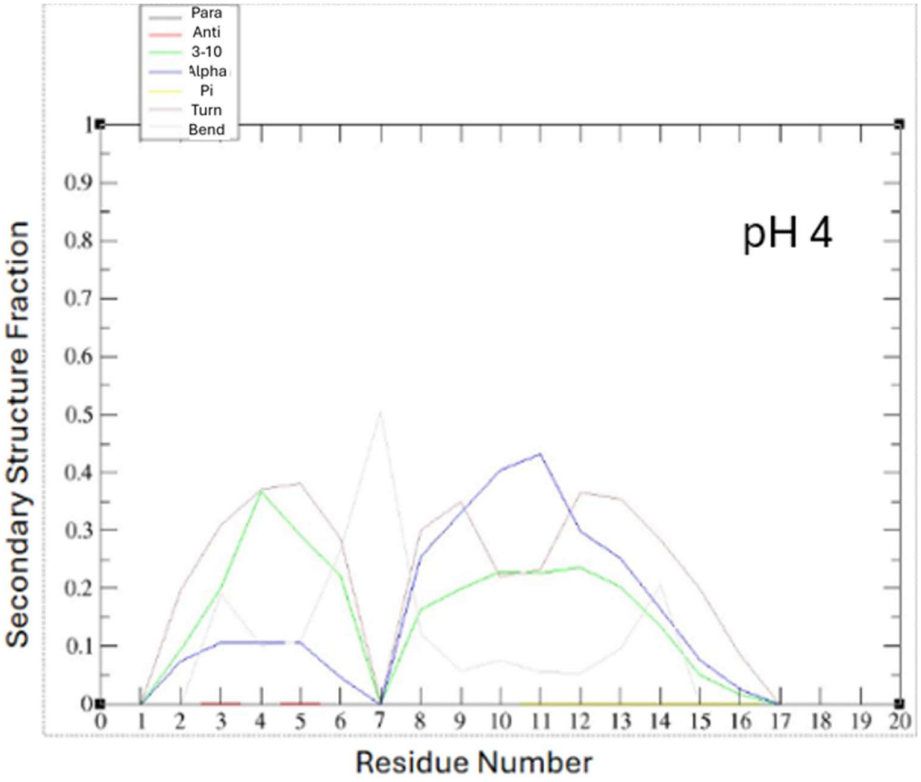
Para
Anti
3-10
Alpha
Pi
Turn
Bend
pH 4
Secondary Structure Fraction
Residue Number

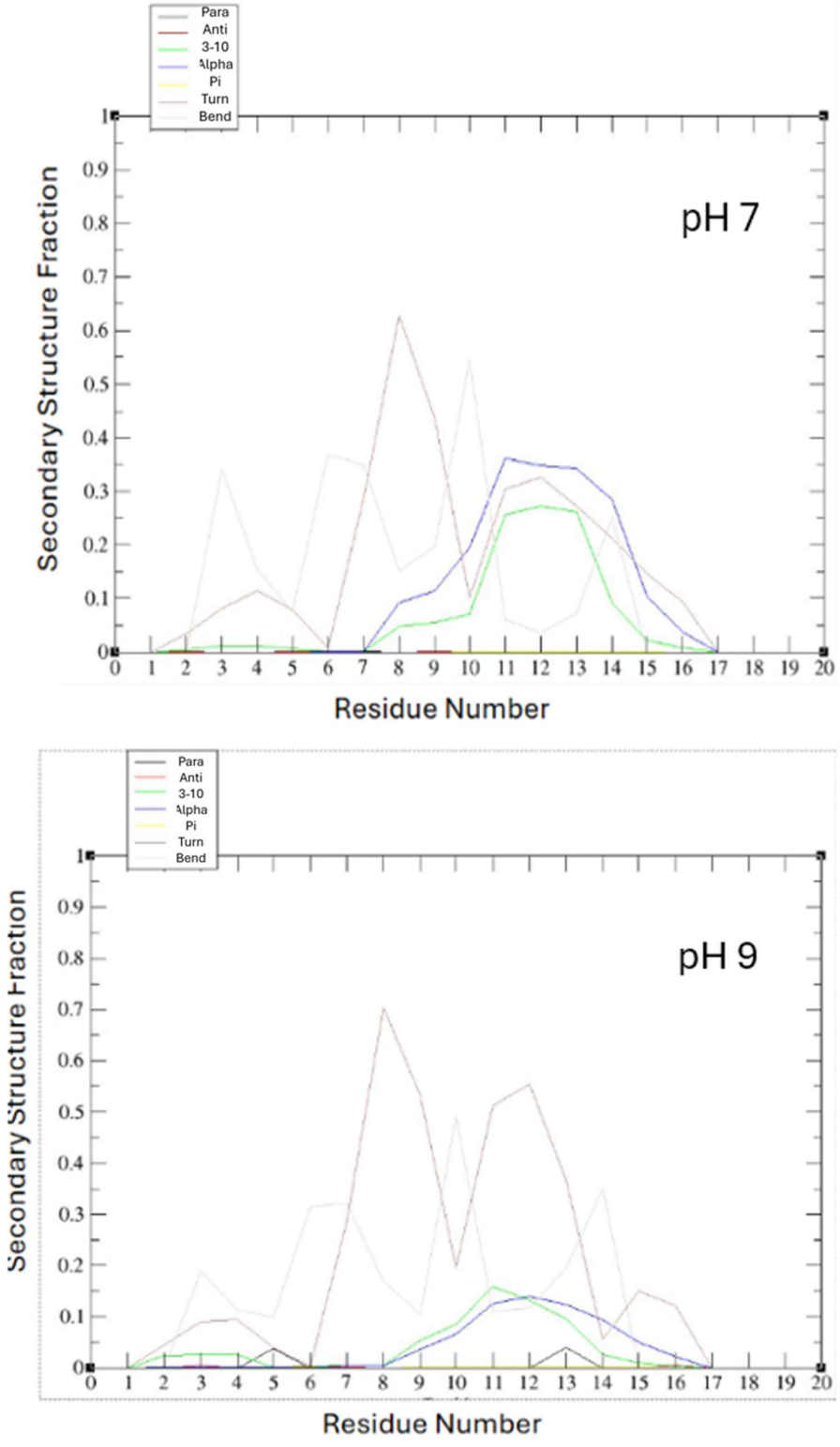

Figure 3.7. Residue-wise secondary structure content of pH 3, 4, 7 and 9. With representations of α-helix (blue), 3,10-helix (green), π-π stacking (yellow), turns (brown), bends (grey), anti-parallel conformation (red), Parallel conformation (black) in Aβ16.

Further analysis of the titratable residues across the pH 1-10 ranges in Figure 3.8 indicates that the isoelectric point of histidine lies near pH 7, identifying it, among those titrated, as the primary residue likely to participate in dynamic interactions under physiological conditions. The observed minor deviations in titration behaviour are consistent with the inherently stochastic nature of CpHMD sampling, particularly given that the analysis is only for 60 ns following 40 ns of system equilibration (consistent conditions for all simulation with Aβ16). These small fluctuations are therefore expected and do not undermine the validity of the results; rather, they reinforce confidence in the robustness of the simulation, demonstrating that the peptide's dynamic protonation behaviour is realistically captured within the constrained sampling window.

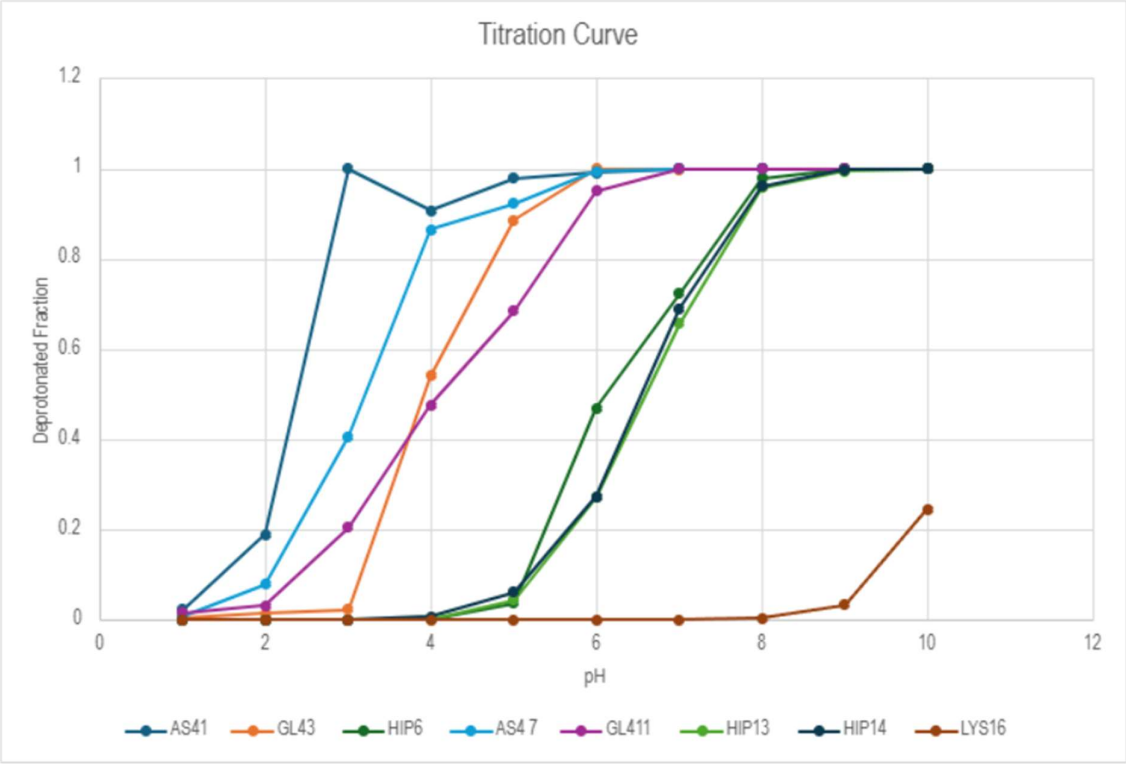

Figure 3.8. Titration curve for protonated Aβ16 residues aspartates in position 1 and 7, glutamate in position 3 and 11, histidine in position 6, 13, 14 and lysine in position 16.

3.3.3 Structural and Conformational Comparisons Between Amylin and Aβ40

The consistency observed in previous statistical parameters provides strong confidence in the validity of the Aβ16 simulations. The RMSD profiles aligned with

Rg trends, supported by SecStruct and Clustering assignments and titration statistics provide a mutually supportive framework of validation across independent measures. This convergence of metrics demonstrates that the structural interpretations are not artifacts of a single analytical approach but are instead robust across different modes of analysis. Building on this confidence, the same suite of analyses was extended to simulations of full-length Aβ40 and amylin sequences, evaluated under a more focused pH range 4 to 9 to probe physiologically relevant environments with higher resolution.

The RMSD graphs in Figure 3.9 highlight that most structures deviate within a 3-5 Å range post-equilibration. The higher pH environments like 7 or 8 see greater conformational changes at 7-17 Å and 8-16 Å across the triplicates (Run 1-3). Meanwhile pH 6 only had a large transient fluctuation of 12 Å near the equilibration point. Similarly transient peaks appear at 200 ns for pH 7 and 8 of 17 Å and 15 Å, respectively. Fortunately, all systems return to stable conformations by 225 ns and maintain compactness until the simulation endpoint, providing confidence in the analysis of data without the need for further simulations that might be required to explore any lingering changes.

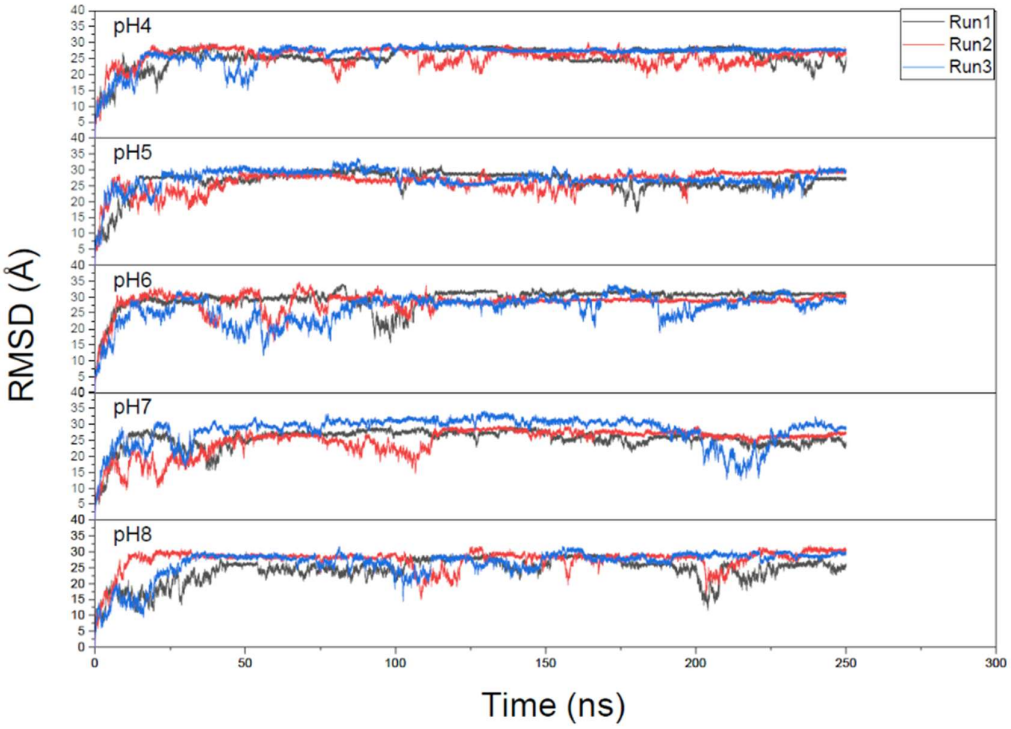

Figure 3.9. RMSD graphs shows convergence between three runs equilibrated at 50 ns in Aβ40 protein as a function of pH 4-8.

In summary, Aβ40 of pH 5 exhibited the least flexible conformation across all simulation runtimes, while displaying the greatest degree of conformational variability in pH 7 and 8. Despite these differences, all trajectories converge to comparable displacement values from their equilibration points after approximately 50 ns, indicating key points such as the observed conformations likely represent stable structural states in conformational space under the tested conditions; and the simulations are reproducible across independent runs. The enhanced stability at pH 5 may be attributed to favourable protonation equilibria at histidine and acidic residues that stabilize hydrogen bonding and reduce long-range electrostatic repulsion, while the increased flexibility at pH 7–8 reflects the near-neutral protonation state that maximizes conformational freedom and allows broader sampling of alternative states. Notably, this flexibility under near-physiological conditions is particularly relevant, as the extracellular environment of the brain maintains a pH of 7.2–7.4, suggesting that Aβ40 may adopt highly dynamic ensembles *in vivo* that facilitate transitions toward aggregation-prone conformations if the electrostatic contributions of histidines are reduced when they're deprotonated as expected at that pH level.

A similar convergence is noted in the amylin RMSD profiles at Figure 3.10, particularly at pH 7, where all trajectories converge to a common plateau band of 20-25 Å by 230 ns and remain in it until the end of the simulation. While amylin is inherently a more flexible peptide, the convergence across replicates highlights that the conformational ensembles at each pH are reproducible and not artifacts of stochastic noise. Notably, simulations of pH 5, 6, and 9 exhibit the largest differences between local maxima and minima (troughs and crests on the graph), with deviations of up to 5 Å by 250 ns, indicating greater conformational plasticity under these conditions. This enhanced flexibility may be associated with the charge-state changes (protonation/deprotonation) that can disrupt salt bridges and H-bond networks.

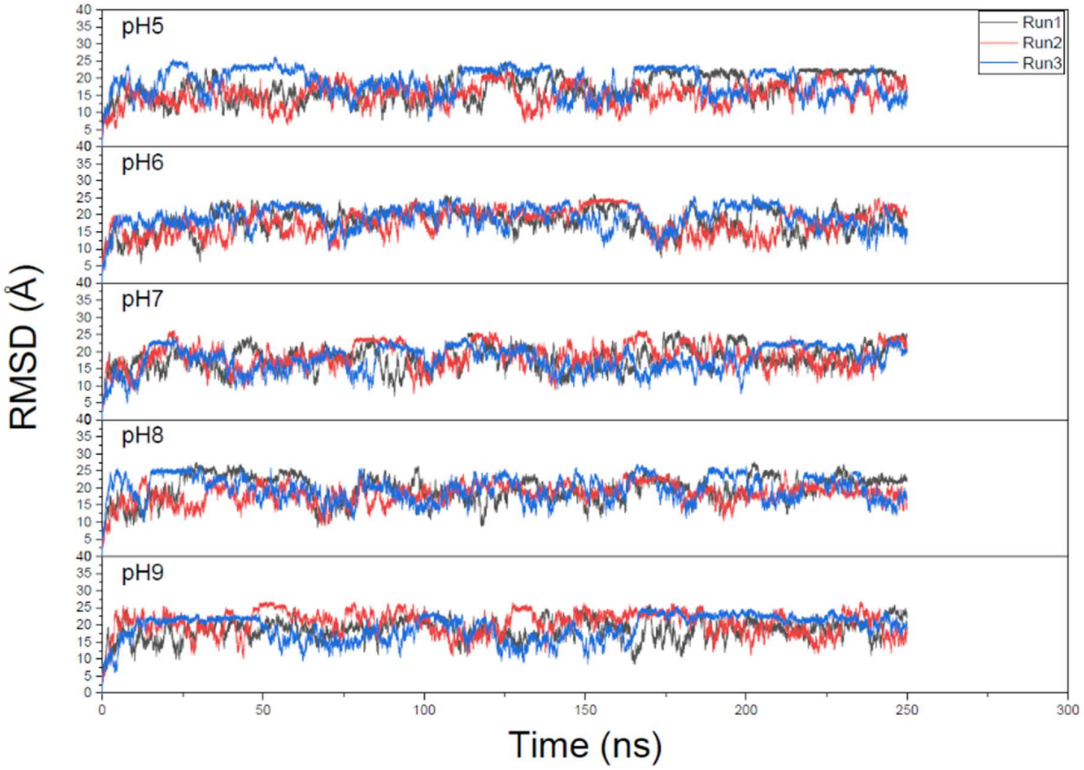

Figure 3.10. RMSD graphs of triplicate amylin protein simulations equilibrated at 50 ns for pH 5-9.

Because Aβ40 and amylin have different titration-sensitive residues and physiologically relevant charge states, Aβ40 was simulated across pH 4-8 range to capture the onset of acidic destabilization around its N-terminal titratable and amylin across pH 5–9 to span the His18-driven near-neutral transition and the slightly basic regime where its charge/compactness changes most. A direct comparison of the peptide graphs shows that, despite the presence of more persistent transient states in Aβ40, its conformations ultimately equilibrate into more compact and less flexible structures. By contrast, amylin remains consistently displaced within a broader 15–25 Å range, reflecting its higher intrinsic flexibility and reduced structural constraints compared to Aβ40. Importantly, this relative rigidity of Aβ40 under certain pH conditions may favour nucleation-prone conformations, consistent with its role in amyloid plaque formation in Alzheimer's disease, whereas higher flexibility can hinder the persistence of aggregation-competent structures.

Table 3.4 reports post-equilibration Rg values, indicating molecular size and compactness. These results show that on average most Aβ40 peptides have relatively extended conformations. The more acidic environments produce more

extended conformations, as noted by the increase in size of the peptide from an Rg mean of 11.6 at pH 7 to 12.2 at pH 5. However, this trend lies within the relatively large standard deviation range of 1.5–1.8 Å with a difference <1.0 Å, overlapping mean differences across pH conditions that may explain the peptide in pH 4 and pH 8 having a relatively compact structure than expected. This is further supported by the minima and maxima values, which demonstrate that at all pH conditions Aβ40 consistently samples compact states around ~9.0 Å, while the upper bounds extend comparably across conditions (up to 19.7–24.6 Å). Thus, the unexpectedly lower mean Rg at pH 4 does not represent a fundamental structural deviation but rather reflects the natural overlap in accessible conformational space across protonation states. These Rg values further suggest that Aβ40 does not undergo significant global size rearrangements in those environments, which is consistent with its RMSD profiles where trajectories converge to comparable displacement values after 50.0 ns regardless of pH. The limited pH sensitivity is likely due to stabilizing hydrophobic contacts and residues prone to β-strand motifs, which act as structural anchors and buffer the influence of protonation changes at the more flexible N-terminal residues. Thus, both Rg and RMSD indicate that Aβ40 remains relatively compact and structurally stable, with pH primarily modulating local rather than global conformational dynamics.

Contrastingly, amylin exhibits consistently larger Rg values than Aβ40 in Table 3.5, reflecting its greater intrinsic flexibility. Its standard deviations are also higher at ~2.3 Å with a >0.3 Å difference, producing considerable overlap with Aβ40 values and suggesting that amylin can transiently adopt sizes comparable to Aβ40 despite its more expanded average ensemble. This agrees with RMSD results, where amylin maintains higher displacement values (10.0–15.0 Å) compared to Aβ40, indicating persistent conformational variability. Both modelling datasets show that amylin's structural compactness and flexibility is maintained across pH values, though with subtly greater compaction at higher or more basic pH environments as exemplified by the 13.1 Å at pH 5 decreasing to 12.9 Å at pH 9. The most compact amylin ensemble arises at pH 9, while pH 7 corresponds to the least compact state (13.2 Å), mirroring RMSD profiles where neutral conditions allow the greatest conformational freedom. Together, Rg and RMSD reinforce that amylin samples a broader conformational space than Aβ40, reflecting reduced structural constraints and a

higher degree of flexibility, while also suggesting that pH does not dramatically alter overall peptide size but instead modulates local stability and transitions between compact and extended states. These findings align with known aggregation environments: mildly acidic conditions such as endosomes or lysosomes for Aβ in Alzheimer's disease, and similar protonation-driven compaction pathways in amylin linked to type 2 diabetes. With regards to their roles in AD, the contrasting data suggest that amylin could enhance the Aβ40 ability to, besides favouring rigid nucleation-prone conformations, adapt towards more flexible structures that can bind other Aβ or amylin molecules, facilitating cross-amyloid or self-associative interactions that promote mixed aggregate formation.

When considered together, these complementary properties may further explain the dynamic of their cooperative relationship during co-aggregation. In this framework, Aβ40 not only suggests a greater propensity to form compact β-strand conformations but also exhibits a clearer pH-dependent shift in global compactness, becoming more expanded under mildly acidic conditions and more compact toward neutral–slightly basic conditions. This sensitivity suggests pH can bias Aβ40 toward more nucleation-prone conformers, allowing it to act as a structural initiator by providing rigid nucleation sites that stabilize early aggregates. Meanwhile, amylin maintains a broader conformational ensemble with only subtle changes in overall size across pH, indicating that it remains a flexible "shapeshifter" that can transiently associate with Aβ nuclei across conditions. By occupying flexible interface regions, amylin may introduce conformational heterogeneity and alter fibril morphology – potentially slowing or redirecting elongation – while still strengthening the growing assembly by forming mixed contacts with the Aβ scaffold. This may increase aggregate stability and resistance to dissociation by embedding dynamic amylin residues into otherwise rigid β-structured Aβ40 frameworks. This process aligns with experimental evidence of cross-seeding, where one amyloidogenic protein accelerates fibril formation of another, and suggests that mixed aggregates may be structurally distinct, potentially explaining differences in toxicity or resistance to clearance mechanisms observed in mixed amyloid pathologies.

Table 3.4: Statistical data for Rg (Å) of Aβ40 protein in CpHMD 600 ns simulations.

pH value	Rg (Avg)	Rg (SD)	Min	Max

4	11.4	1.6	9.2	19.7
5	12.2	1.8	9.4	19.7
6	12.0	1.7	9.6	24.6
7	11.6	1.7	9.2	22.9
8	11.4	1.6	9.3	22.1

Table 3.5: Statistical data for Rg (Å) of amylin protein in CpHMD 600 ns simulations.

pH value	Rg (Avg)	Rg (SD)	Min	Max
5	13.1	2.3	9.1	23.7
6	12.9	2.2	9.1	23.4
7	13.2	2.3	8.9	23.5
8	13.1	2.2	8.8	22.6
9	12.9	2.1	8.9	21.8

The sampling methods used in the Rg analysis above were further extended to probe the effects of pH variance on secondary structure content, as noted in Tables 1.6 and 1.7. Both Aβ40 and amylin are dominated by irregular motifs, with turns and bends comprising 37–43% in Aβ40 and 42–45% in amylin, and coils accounting for 31–34% and 30–34%, respectively. In contrast, ordered motifs contribute less: helical content ranges from 17–24% in Aβ40 and 19–25% in amylin, while β-strand conformations remain minimal, though slightly higher in Aβ40 (5–12%) compared to amylin (0.4–3%). Closer examination of the pH-dependent distributions reveals distinct behaviours in the two peptides. In Aβ40, β-strand formation peaks at pH 5 (11.6%) and helix content maximizes at pH 6 (23.3%), with pH 7 showing the highest combined helix + strand content (31.2%). This pattern is consistent with the stabilizing influence of partial protonation at near-neutral pH, which reduces electrostatic disorder and promotes the formation of β/helix motifs linked to aggregation in Alzheimer's pathology. Amylin, by contrast, exhibits consistently low β-strand content across all conditions, with its secondary structure dominated by helices and turns. Its highest helix fraction occurs at pH 6 (24.5%), paralleling Aβ40, but this drops sharply by pH 9, where coils and turns make up most of the ensemble. This shift reflects the greater hydrophilic content and loop flexibility of amylin, which

favour solvent-exposed, dynamic conformations over aggregation-competent β-structures. Aβ40 demonstrates local stabilization of β/helix motifs under near-neutral conditions that may seed aggregation, whereas amylin retains higher conformational plasticity, favouring transient, non-β structures that are less directly amyloidogenic. These profiles indicate that both peptides remain highly flexible across pH values, consistent with their elevated RMSD fluctuations and broad Rg distributions. The predominance of turns and coils highlights a lack of stable secondary structure, a feature characteristic of intrinsically disordered proteins. Taken alongside RMSD and Rg, which reinforces the reliability of the observed ensembles, the SecStruct results suggest that while both Aβ40 and amylin fluctuate between loosely compact and extended states depending on protonation conditions, their conformational instability across pH ranges provides a structural basis for aggregation-relevant behaviour.

Table 3.6. Percentage of Aβ40 classified as helical, strand, Turns/bends or Other across pH 4-8.

pH value	Helices (pi/alpha/3-10)	β-Strands (anti-/parallel)	Turns/Bends	Coil
4	19.9	5.1	42.3	32.7
5	17.5	11.6	38.6	32.3
6	23.3	4.9	39.7	32.1
7	21.6	9.6	37.4	31.4
8	17.4	9.1	39.1	34.4

Table 3.7. Percentage of amylin classified as helical, strand, Turns/bends or Other across pH 5-9.

pH value	Helix (pi/alpha/3-10)	Strand (anti-/parallel)	Turn/Bend	Coil
5	24.2	0.4	41.9	33.5
6	24.5	0.8	44.2	30.5

7	23.2	1.4	42.7	32.7
8	19.8	2.9	45.2	32.1
9	19.0	2.0	45.0	34.0

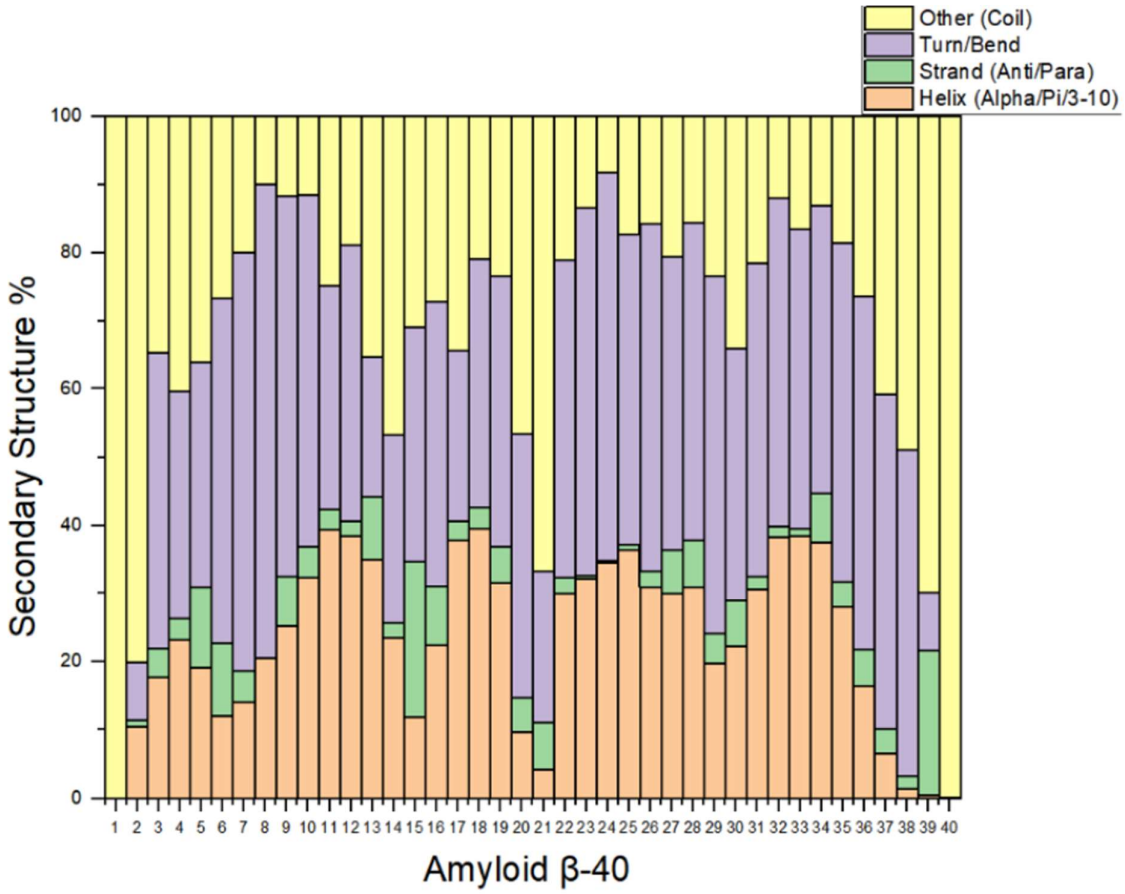

Figure 3.11. Secondary structure percentages by residue (%) for Aβ40 of the combined trajectories of each run for pH 6.

Although both proteins adopt broadly similar proportions of secondary structure elements overall, the distribution of those conformations differs substantially. A closer look at the residue-specific structural trends for Aβ40 and amylin at pH 6 as illustrated in Figures 3.11 and 3.12 would not only add clarity to our previous analysis but also provide visual comparisons between the concerned peptides. This pH was chosen for analysis because the observed structural content in its highest

cluster populations, as noted in the appendices Figure A1, resembles most closely to the data provided in these graphs.

For Aβ40, the secondary structure is characterized by a predominance of coil content at the termini and within the central region of the peptide at residues 20–21. This localized high coil content may be attributed to the multiple aromatic residues such as phenylalanine, which increases aggregation by promoting hydrophobic stacking in the core. The remainder of the sequence is dominated by turns and bends (residues 3–19 and 22–36), interspersed with small stretches of helices (α, 3_{10}, or π) and sparse β-strand content. The highest strand content appears near residue 39, consistent with the enrichment of nonpolar residues such as valine at the C-terminus, a region with well-documented involvement in β-sheet formation and amyloid fibril nucleation. This pattern underscores the role of the C-terminal region as a key structural determinant in AD-associated amyloid aggregation.

Amylin exhibits similar structural trends as noted in the Aβ40 plot, with the coil propensity being largely confined to the termini and turns and bends content dominating N-terminal (residues 3–5) and C-terminal regions (residues 17–34). However, it is in the central region where the differences with Aβ40 become apparent. There is no pronounced turn/bend minimum or large coil content around residues 18-22, comparable to what's seen in with Aβ40. Its helical conformations are also more localised, showing high propensity in two regions at 6-16 and 24-27; meanwhile, the β-strand content is nearly absent. This lack of strand formation may reflect the presence of a stabilizing disulfide bond, which imposes conformational rigidity and limits strand pairing, thereby biasing the ensemble toward helices and flexible turn/bend motifs. The relatively higher helical content in amylin is also consistent with the more distributed positioning of hydrophobic residues (e.g., alanine, valine, tyrosine, phenylalanine), which reduces clustering and diminishes the driving force for extended β-aggregation. Contrastingly, the prevalence of hydrophilic residues such as serine and threonine in turn/bend regions enables favourable hydrogen bonding with solvent, stabilizing flexible conformations. This may explain why, at higher pH values (7–9), amylin shifts further toward coil and turn content, with helices diminishing as electrostatic changes destabilize ordered motifs. Taken together, these residue-specific trends suggest that while Aβ40 is structurally predisposed to forming β-aggregation-prone motifs under near-neutral conditions,

amylin maintains a highly flexible, helix- and turn-rich ensemble that may resist persistent β-sheet assembly but could modulate aggregation pathways through transient interactions, highlighting distinct but potentially complementary roles in amyloid formation.

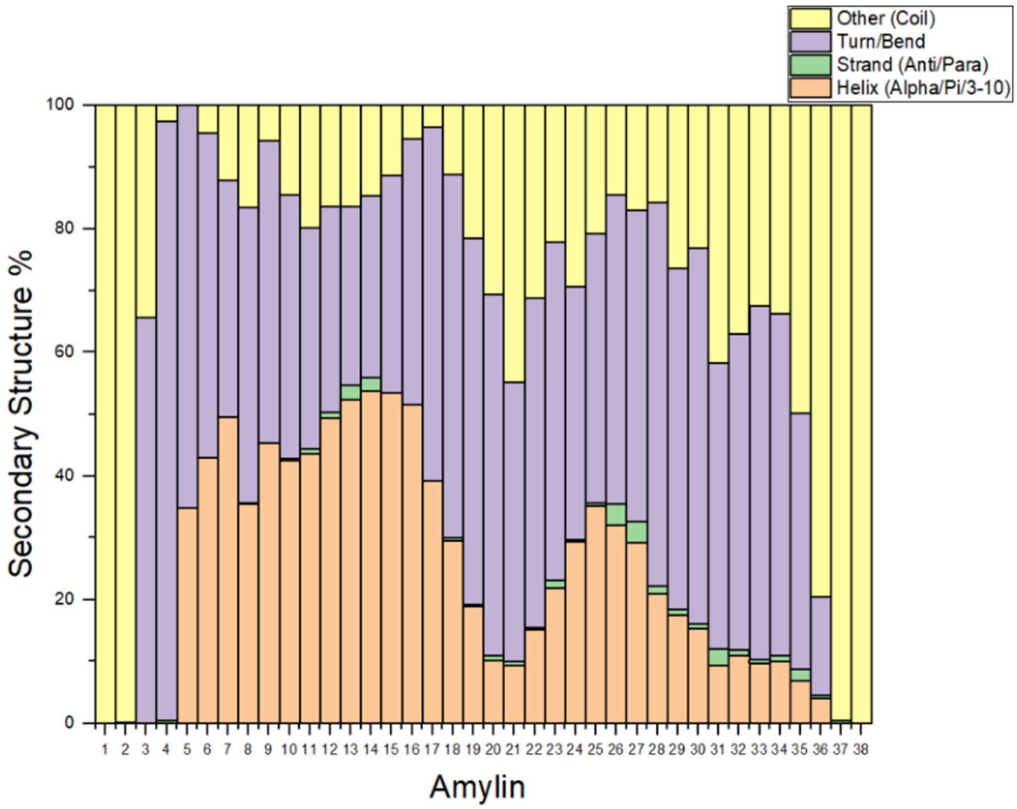

Figure 3.12. Secondary structure percentages by residue (%) for amylin of the combined trajectories of each run for pH 6.

The titratable residues in each simulation were analysed for their fractional deprotonation states, with results plotted in Figure 3.13, alongside an average of those all values across the 600 ns trajectories to illustrate overall trends. These data highlight the dynamic involvement of histidine residues around neutral pH, with isoelectric points between 6.4 and 6.8 for His6, His13, and His14 in Aβ40, and 6.4 for His18 in amylin, suggesting that protonation changes in these residues can locally modulate electrostatic interactions and hydrogen bonding. This may also explain how more stable conformations of helices and β-strand content are observed transiently in Aβ40 near pH 6-7, with His residues being partially protonated and thus potentially stabilizing the nucleation-prone motifs. Here, more stable is defined by the persistence of the secondary structures throughout the simulation and pH data sets.

In contrast, strongly acidic residues like aspartate and glutamate, or basic residues such as lysine, remain largely protonated or deprotonated across the simulated pH range, contributing less to dynamic structural variability. Amylin deprotonation states presented in Figure 3.14 correlates to the earlier findings, showing titration curves that rise from rise sharply from pH 5 to 7 before plateauing near complete deprotonation above pH 8, confirming the expected behaviour of the residues and the reliability of the simulation data. The similarity of replicate trajectories further supports convergence, where only minor deviations occur in the midpoint transitions among the runs. The differences in fractional deprotonation across pH conditions correlate with subtle conformational changes, particularly in regions enriched with His residues, suggesting that the pH-dependent protonation of these side chains may fine-tune the balance between flexible coil/turn regions and more ordered helices or β-strands. This interplay provides a mechanistic explanation for the observed pH sensitivity of Aβ40 secondary structure, whereas amylin, with fewer β-strand-prone residues and more localized helices, exhibits smaller structural shifts despite similar protonation dynamics, highlighting the role of sequence-specific context in modulating peptide flexibility and aggregation propensity.

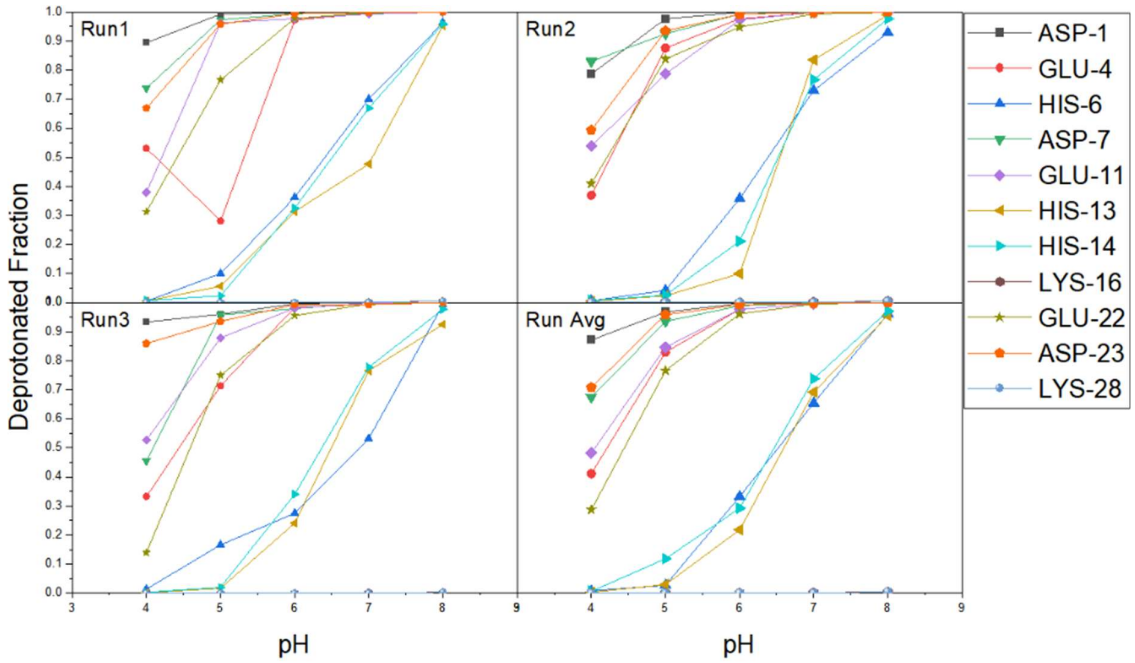

Figure 3.13. Deprotonated fraction vs. pH graphs for Runs 1-3 and their average for Aβ40.

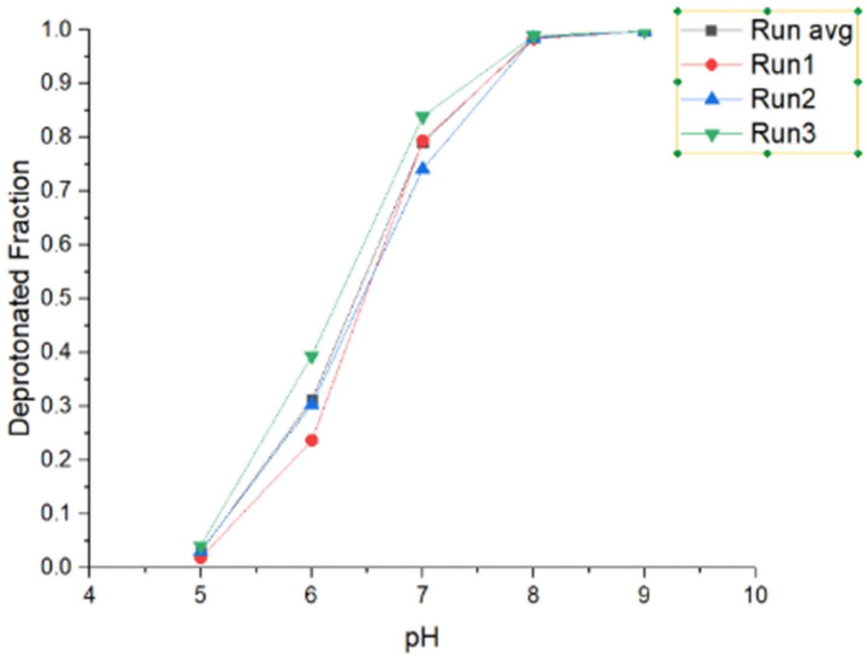

Figure 3.14. Deprotonated fraction vs. pH graph for runs 1-3 and their average for histidine in amylin protein.

3.4 Conclusion

Comparative simulations of $A\beta_{16}$ in explicit and implicit solvent environments establish the reliability of the implicit solvation model, as evidenced by near-identical RMSD, Rg, and protonation profiles (~±2.0). Subsequent CpHMD runs across pH 1–10 supported the methodological and analytical parameters for use more focused pH-dependent simulations since the extreme protonation states at very low or high pH destabilized the amyloid's ordered secondary structure, leading to increased flexibility and loss of compactness.

Simulations carried out under near-neutral pH conditions (pH 4–8) favour compact structural parameters and organized secondary structures, suggesting that partial protonation of histidine residues may stabilize intra-peptide hydrogen bonding and salt-bridge formation, a trend consistent with experimental reports on amyloid nucleation. In comparison the amylin peptide at similar pH range (5-9) remained more conformationally plastic, exhibiting broader RMSD fluctuations and larger Rg values. Despite these differences, both peptides shared a predominance of coil, turn, and bend structures, indicative of their intrinsically disordered nature. Notably, Aβ40 demonstrated an increase in β-strand content near pH 5–7, supporting its propensity

toward aggregation-prone conformations; whereas amylin favoured helical and turn-rich motifs, with minimal β-structure formation even under conditions conducive to aggregation.

Applying titration analysis on histidine residues (His6/13/14) in Aβ40 and (His18) in amylin, suggested them as critical modulators of pH-dependent stability. Their protonation values and isoelectric points ranging from pKa 5-7 collectively imply that Aβ40 may achieve structural stability and aggregation readiness under near-neutral pH, whereas amylin retains flexibility that may allow it to transiently interact with Aβ nuclei, stabilizing or disrupting fibril elongation through conformational adaptability. Although these studies were limited to monomeric and homodimer systems, the data suggest that CpHMD can effectively capture protonation-dependent structural transitions that underpin aggregation. Further work extending to heterodimeric and oligomeric simulations could provide deeper insights into the mechanistic interplay between Aβ and amylin in cross-seeding and its implications for amyloid co-pathologies.

3.5 References

1. Albrahadi T, Hureau C, Platts JA. Constant pH Molecular Dynamics Simulation of pH Effects on amyloid-β Structure, Dynamics, and Metal-Binding. Chem Weinh Bergstr Ger. 2025 June 17;31(34):e202500547.

2. Xie L, Lockhart C, Bowers SR, Klimov DK, Jafri MS. Structural Analysis of amylin and amyloid β Peptide Signaling in Alzheimer's Disease. Biomolecules. 2025 Jan 9;15(1):89.

3. Brännström K, Islam T, Sandblad L, Olofsson A. The role of histidines in amyloid β fibril assembly. FEBS Lett. 2017 Apr;591(8):1167–75.

4. CPPTRAJ cookbook – AMBER-hub [Internet]. [cited 2025 Sept 29]. Available from: https://amberhub.chpc.utah.edu/cpptraj-cookbook/

5. Sgourakis NG, Yan Y, McCallum S, Wang C, Garcia AE. The Alzheimer's peptides Aβ40 and 42 adopt distinct conformations in water: A combined MD / NMR study. J Mol Biol. 2007 May 18;368(5):1448–57.

6. Nasica-Labouze J, Nguyen PH, Sterpone F, Berthoumieu O, Buchete NV, Coté S, *et al. Amyloid* β Protein and Alzheimer's Disease: When Computer Simulations Complement Experimental Studies. Chem Rev. 2015 May 13;115(9):3518–63.

7. Ball KA, Phillips AH, Nerenberg PS, Fawzi NL, Wemmer DE, Head-Gordon T. Homogeneous and heterogeneous tertiary structure ensembles of amyloid-β peptides. Biochemistry. 2011 Sept 6;50(35):7612–28.

8. Lang EJM, Baker EG, Woolfson DN, Mulholland AJ. Generalized Born Implicit Solvent Models Do Not Reproduce Secondary Structures of De Novo Designed Glu/Lys Peptides. J Chem Theory Comput. 2022 July 12;18(7):4070–6.

9. Han W, Schulten K. Further optimization of a hybrid united-atom and coarse-grained force field for folding simulations: Improved backbone hydration and interactions between charged side chains. J Chem Theory Comput. 2012 Nov 13;8(11):4413–24.

10. Anandakrishnan R, Drozdetski A, Walker RC, Onufriev AV. Speed of conformational change: comparing explicit and implicit solvent molecular dynamics simulations. Biophys J. 2015 Mar 10;108(5):1153–64.

11. Dobrev P, Vemulapalli SPB, Nath N, Griesinger C, Grubmüller H. Probing the Accuracy of Explicit Solvent Constant pH Molecular Dynamics Simulations for Peptides. J Chem Theory Comput. 2020 Apr 14;16(4):2561–9.

12. Chen J, Brooks CL, Khandogin J. Recent advances in implicit solvent based methods for biomolecular simulations. Curr Opin Struct Biol. 2008 Apr;18(2):140–8.

13. Okur A, Wickstrom L, Layten M, Geney R, Song K, Hornak V, *et al.* Improved Efficiency of Replica Exchange Simulations through Use of a Hybrid Explicit/Implicit Solvation Model. J Chem Theory Comput. 2006 Mar 1;2(2):420–33.

14. Schaefer M, Karplus M. A Comprehensive Analytical Treatment of Continuum Electrostatics. J Phys Chem. 1996 Jan 1;100(5):1578–99.

15. Still WC, Tempczyk A, Hawley RC, Hendrickson T. Semianalytical treatment of solvation for molecular mechanics and dynamics. J Am Chem Soc. 1990 Aug 1;112(16):6127–9.

16. Cramer CJ, Truhlar DG. Polarization of the nucleic acid bases in aqueous solution. Chem Phys Lett. 1992 Oct 2;198(1):74–80.

17. Ryckaert JP, Ciccotti G, Berendsen HJC. Numerical integration of the cartesian equations of motion of a system with constraints: molecular dynamics of *n*-alkanes. J Comput Phys. 1977 Mar 1;23(3):327–41.

18. Roe DR, Cheatham TE. PTRAJ and CPPTRAJ: Software for Processing and Analysis of Molecular Dynamics Trajectory Data. J Chem Theory Comput. 2013 July 9;9(7):3084–95.

19. Humphrey W, Dalke A, Schulten K. VMD: Visual molecular dynamics. J Mol Graph. 1996 Feb 1;14(1):33–8.

20. Xu W, Su H, Zhang JZH, Mu Y. Molecular dynamics simulation study on the molecular structures of the amylin fibril models. J Phys Chem B. 2012 Dec 6;116(48):13991–9.

Chapter 4: CpHMD Modelling of Aβ40–Amylin Dimer and Trimer Formation: Protonation-Driven Early Aggregation Pathways

4.1 Introduction

Figure 4.1 (data provided by Christelle Hureau; personal communication) summarizes the effect of varying amylin fractions on Amyloidβ-40 (Aβ40) aggregation kinetics as monitored by thioflavin T (ThT) fluorescence. In the fluorescence vs. time graph, 100% amylin rapidly increases in fluorescence and reaches an early plateau, indicating that amylin aggregates much faster than Aβ. The smaller fractions are mixed with Aβ40 and show a slow rise from 0% amylin concentration, which has a long lag-time and lower fluorescence up to 10%, which then increases in intensity and shortens in lag phase compared with pure Aβ. However, beyond this range, the amylin content is of ≥25–50%. The fluorescence plateaus indicate that the aggregation kinetics no longer accelerates and is maximized at low amylin ratios. The normalized half-life vs. Amylin percentage graph reinforces this trend by presenting a sharp drop in normalized $t_1/_2$ from 0–10% amylin followed by stabilization at higher percentages, highlighting that amylin's influence on aggregation is strongly ratio-dependent rather than uniformly accelerating or inhibitory.

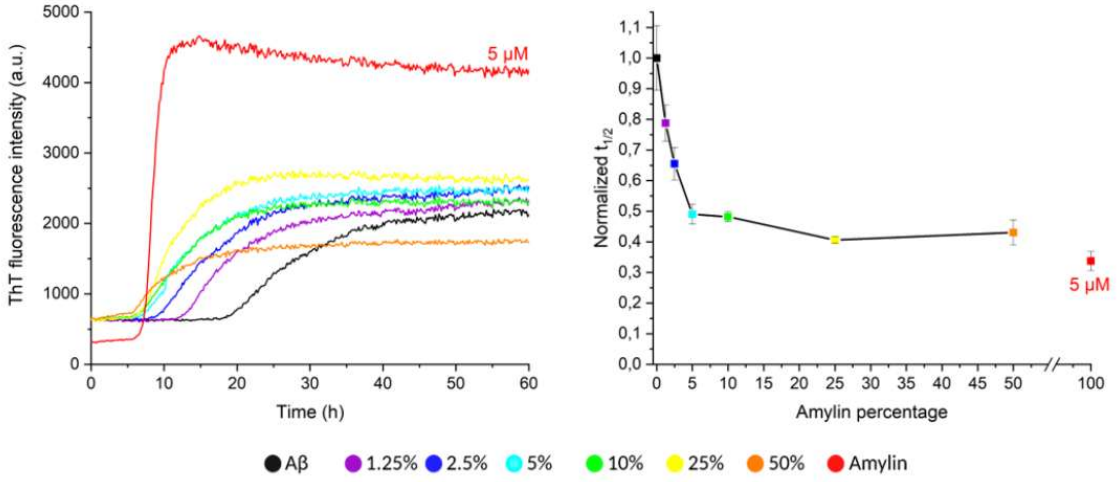

Figure 4.1 Thioflavin T fluorescence intensity and normalized half-time ($t_1/_2$) plots run at pH 7.4 show that small additions of amylin (≤10%) markedly accelerate Aβ40 aggregation,

consistent with a strong cross-seeding effect. The strongest effect occurs between 25% and 50%. I can't represent this exact percentage in a trimer – oligomers require integer counts – so the 1:2 trimer (33%) is a pragmatic discrete mechanistic model of cross-seeding rather than a literal mapping of bulk percentage. I present it as a stoichiometric test case for interfacial mechanisms, not as a concentration-equivalent of the experiment.

Based on Professor Hureau's experimental data, the research presented here is undertaken to analyse the molecular behaviour of amylin and Aβ40 during the nucleation events preceding plaque formation in the brain as part of the aggregation pathway underlying the pathological overlap between type-2 Diabetes and Alzheimer's disease. Accordingly, a baseline was first established for the conformational behaviour of Aβ40 and amylin dimers across multiple pH conditions and then carried forward the more stable complexes into trimer simulations. Trimers were designed with 33% amylin content, as this ratio is intended to capture amylin's influence on early Aβ nucleation, and simulations were run in triplicate to improve reproducibility. Using constant pH molecular dynamics (CpHMD) simulations on these oligomers, shifts in protonation states of titratable residues were examined across physiologically relevant pH ranges to assess how they may influence electrostatic balance and aggregation kinetics (1,2). The latter analysis metrics were determined through CPPTRAJ, Cpinutil.py, and MMPBSA.py programmes.

The first phase of this chapter focuses on dimeric interactions in pH 7.4, representing the healthy brain's physiological environment. Here, the focus is on characterizing the hetero- and homodimer conformational stability , and the self-association tendencies of the protonation-consistent models of both peptides from ClusPro docking results. These dimers were refined under previously established conditions of CpHMD simulations using the AMBER22 framework and analysed with the established parameters of previous experiments. The analysis was expanded to also consider MM/GBSA binding free energy to estimate relative binding affinities (3,4) and solvent accessible surface area (SASA) analysis to quantify hydrophobic exposure over long trajectories (≥100 ns), as longer simulations provide more reliable averages for flexible peptides (5). Both analyses help characterize the peptides based on their protonation-dependent shifts.

To further elucidate the influence of environmental pH on complex stability and aggregation propensity, extended dimer simulations and analyses were also

performed on pH 6, 7, and 8. Such conditions have precedent from the previous experiments and biological relevancy; pH 6 corresponds to the acidic conditions in synaptic vesicles (6) and endosomal compartments (7) where amyloidogenic peptides are known to accumulate; pH 7 reflects the environment of typically healthy intracellular conditions; and pH 8 is a slightly basic stress-test condition beyond physiological neutrality (8).

Finally, building upon the outcomes of the dimer studies, trimeric systems were designed. Trimers are an order above dimers in oligomerization and, thus, represent the transitional species between transient dimers and stable protofibril assemblies. These were similarly generated through ClusPro docking using the table dimers from pH 7 and 7.4 simulations as receptors and their respective amylin or amyloid monomers as ligands. The composition was established based on the physiologically relevant compositions and experimental trends observed in the thioflavin T fluorescence assays provided by C. Hureau through private communication in Figure 4.1. The resulting trimeric assemblies were subsequently refined through 600 ns CpHMD simulations and then analysed.

4.2 Methodology

Four and three conformational ensembles of the highest cluster populations (>10%) were obtained from the cluster models of Aβ40 and amylin peptides simulated and stabilized over 600 ns**.** Together, they make up 62% and 69% of their respective conformations. Boston University's ClusPro server was used for protein-protein docking. ClusPro is an optimized protein-protein docking server, assessed and validated through the global competitive benchmark initiative Critical Assessment of PRedicted Interactions (CAPRI). It provided thousands of poses using rigid-body docking and ranked the results by pose-population size, making it easy to simulate from a low-energy basin conformer start point. The peptides were compatibilized by manually removing all non-standard amino acids such as protonated histidine, aspartate and glutamate residues. After which these peptides were docked into the server employing a Cartesian product approach. Every conformation of Aβ40 cluster set (receptor) was combined with amylin cluster set (ligand). The resulting heterodimeric complexes of sequence illustrated in Figure 4.2 were denoted numerically according to their receptor–ligand pairings and ClusPro's internal naming convention for population sizes as expanded upon further below.

Amyloidβ-40

N-ASP ALA GLU PHE ARG HIS ASP SER GLY TYR GLU VAL HIS HIS GLN LYS LEU VAL PHE PHE ALA GLU ASP VAL GLY SER ASN LYS GLY ALA ILE ILE GLY LEU MET VAL GLY GLY VAL VAL TER

Amylin

N-LYS CYX ASN THR ALA THR CYX ALA THR GLN ARG LEU ALA ASN PHE LEU VAL HIS SER SER ASN ASN PHE GLY ALA ILE LEU SER SER THR ASN VAL GLY SER ASN THR TYR-NHE TER

Figure 4.2. Aβ40 and amylin heterodimer sequence. Titratable residues shown in red and terminal modifications shown in blue.

Only four cluster models were used because of the 10% minimum threshold that was considered for population size when choosing input docking peptides, since this ensured that only the most statistically significant and hence thermodynamically stable regions of the conformational ensemble were used. Otherwise, smaller clusters (<10%) would represent transient or energetically unfavourable conformations with limited contribution to overall dynamics. A risk with this approach is that certain low population clusters with stable and compact structures may be missed out on. ClusPro performs docking with an energy-based clustering system and a physics-derived scoring function that can accurately capture electrostatics, van der Waals interactions and desolvation–dominant forces that govern early peptide aggregation. It maintains a balanced coefficient of these forces to avoid biases towards either electrostatic or hydrophobic dominance as the primary driving force for binding is not specified, producing more balanced and reliable docking predictions (9). This makes it particularly suited to model amyloidogenic systems, where interactions are driven by hydrophobic stacking and charge complementarity rather than lock-and-key binding. Other reasons for its use over other tools like HADDOCK or RosettaDock, include a Fast-Fourier Transform (FFT) based robust rigid-body sampling algorithm (PIPER) that can explore the interaction space between two peptides in depth. It has superior performance in predicting protein–protein interfaces without prior experimental restraints, an unbiased global docking strategy that has compatibility with MD-derived conformations as done in this experiment, and free and efficient evaluating for all cluster pairings (10, 11).

To further assess the influence of molecular orientation and binding roles on complex formation, a reciprocal docking strategy was employed, reversing the receptor–ligand assignments between Aβ40 and amylin. A single docking direction might miss certain interactions depending on molecular orientations due to the flexibility and lack of fixed binding interfaces that these amyloidogenic proteins have. Hence a reversed receptor versus the ligand heterotypic interaction was simulated as well, ensuring that potential asymmetries in binding affinity, stability, or interface composition are identified, and allowing for a more complete understanding of how each peptide's conformational dynamics contribute to complex formation. In parallel, homodimerization analysis was also conducted for all combinations of selected Aβ40 and amylin clusters to establish a baseline for their self-association tendencies. It is essential in understanding whether the formation of Aβ40–amylin complexes represent a cooperative or competitive pathway relative to each peptide's intrinsic aggregation behaviour. This dual approach provides critical insight into whether cross-aggregation between the two peptides is thermodynamically and structurally preferred, or merely a byproduct of their individual propensities for self-assembly.

Although ClusPro provided over 50 clusters for each dimer combination. Owing to time constraints and the lack of knowledge on what forces may dominate in the complex, only the three conformations with higher cluster populations were chosen for further study to maintain focus on the most statistically and energetically relevant conformations. Denoted as *.10*, *.11*, and *.12*. These identifiers were retained for all following experiments for consistency. For example, a dimer formed between Aβ40 cluster 0 and amylin cluster 0, corresponding to ClusPro's top-ranked solution, was labelled 0x0.10.

Each selected dimer sequence was subsequently refined to ensure consistency with the protonation states and functional group assignments used in the pre-docking peptide simulations, with one exception. Titratable residues such as aspartic acid, glutamic acid, and lysine were not included in the pH titration process; they were assigned fixed protonation states as their ionization behaviour remained the same within and near the physiological pH range due to their high or low pKa values. Histidine was selected as the focus of protonation-deprotonation events because of their sensitive imidazole sidechain having a pKa value close to physiological pH. Using the protonated states of these titrated residues, predicted charges were also

calculated to understand the electrostatics of the overall peptide. This approach builds on prior simulation data, and the new model would capture the most biologically relevant pH-responsive behaviour without overcomplicating the system with residues unlikely to change state within the studied pH range.

The finalized dimer sequences, modified through LEaP function of AMBER 22 package were placed in the AMBER ff10 force field for CpHMD simulations in implicit solvent. Using the established methods from previous successful experiments, the topology and coordinate files were simulated in the Generalized Born solvation model with random seeds for initial velocities. The SHAKE algorithm was used to constrain bonds to hydrogen atoms, and a 2-fs integration timestep was used to remove high-frequency bond vibrations. After minimization both types of dimers were heated using Langevin thermostat at a temperature of 300 K, and all simulations were performed within the NVT ensemble.

The first set of production simulations were carried out at pH 7.4 for the three highest cluster populations of each combination of ClusPro dimers for both types – hetero- and homo- dimers. The simulations were visualized using VMD and if the dimers remained together, they were considered successful and further visualized in MOE, PyMol, simulated another 500 ns and analysed from 100 to 600 ns. Those that broke apart were considered failures and reported alongside the successes in Table 4.1 in the results and discussion section. To ensure efficiency and enable iterative refinement, successful simulations of Aβ40 x amylin were analysed first before proceeding with the remaining dimer combinations. For comparison with their monomer counterparts, the cluster of amylin and amyloid monomers from the previous pH 7 simulations were further simulated at up to 600 ns at pH 7.4 and analysed. Analysis of the resulting trajectories was performed using CPPTRAJ, Cpinutil.py, MMPBSA.py and visualized in OriginLab 2025. Specifically, the conventionally quantitative analysis from previous experiments such as RMSD, Rg, SecStruct, and solvent accessible surface area (SASA) to assess pH-dependent exposure that may influence peptide aggregation propensity. Energy analysis was also used but had to be parameterized for both entropy and enthalpy calculations.

Binding energy analysis was carried out for each dimer with the Molecular Mechanics/Generalized Born Surface Area (MM-GBSA) method to determine the

interaction energy between chains, and to identify residues that contribute to this. Since the calculations do not estimate the entropy contribution to binding, the entropy is calculated separately using normal mode approximation, and the Gibbs free energy is then calculated manually. To achieve reliable and efficient enthalpy calculations, a balance of frame count, simulation runtime range, and standard deviation is very important. The data are collected from the end of the 100 ns simulation as it would generally be considered the most stable portion of the simulation as denoted by the RMSD graphs. Excessively long runtimes, or high SD and frame count would produce erratic data points that reduce the reliability of data. Alternatively, a small frame count and runtime would analyse very few data points leading to poor results as well. Dimers with established reliability and consistency were used to determine the best parameters. A range of runtimes (1-10 ns) and frames (6-51 frames) were tested and produced the ideal combination of 51 frames across 5 ns runtime, where each frame is taken at an equal interval. This allowed analysis of a sufficient range of data points and had consistent standard deviations to ensure both efficiency and accuracy. Utilizing the same ranges, another batch of calculations were applied for normal mode entropy. The high computational cost (6 frames per hour) limited the possibilities but a combination of a 5 ns runtime with a total of 6 frames was eventually realized as ideal since it provided the lowest SD range while also overlapping with the entropy values of all other frames. All following enthalpy and entropy calculations for the following experiments in this chapter are set to these parameters.

Another experiment, to investigate the effects of other pH environments on Aβ40-amylin complexes was conducted. Recognizing the large effort that simulating and analysis over 250+ dimers had required in the previous experiments, the scope of this one was reduced to be more manageable. Only the three highest clusters from only the first three matched hetero- and homo- dimer combination, i.e. 0x0, 1x1, and 2x2, from the pH 7 ClusPro conformations was used for triplicate repeats in CpHMD simulation. The Aβ40 x amylin heterodimers were abbreviated to ‘abxam’ and its reciprocal ‘amxab’; similarly, the amyloid and amylin homodimers were abbreviated to ‘abxab’ and ‘amxam’. Following the established simulation parameters for dimers, their sequences were modified to include the positive charge at the N-terminus and an NH_2 cap at the C-terminus, and a double bond between cysteine 2-7 residues.

These dimer conformations were minimized, heated and run at pH 6, 7, and 8 for 100 ns. The resulting peptides were viewed by VMD, and their success-failure data is reported in Table 4.5.2. Of the successfully simulated dimers, only the highest combination, usually 0x0.10, for each homo- and hetero- dimer group was further simulated up to a total of 600 ns, with the early 100 ns taken as equilibration and the later 500 ns used for analysis. If any dimer broke apart after the 100 ns the next highest combination conformation was used instead. Unfortunately, all amylin homo-dimers when simulated to 100 ns mark broke apart, due to a limitation of the implicit solvent model being unable to accurately account for the presence/placement of counterions that in physiological environments help neutralize surface charge buildup and stabilize electrostatic interactions at the dimer interface, preventing such premature dissociation. This was discovered when amylin homodimer simulations were repeated in explicit models for 100 ns in pH 6 with appropriate neutralizing ions of chloride. They presented an 89% success rate with only a single simulation breaking apart. The highest order combination, 0x0.10, was extended to a further 500 ns simulation and analysed to verify the stability of the structure and further highlight the implicit model as a limiting factor to amylin homodimer simulations' success. The analysis, however, is not presented here as it is only a single simulation that took 3 days to complete and in a different solvent model.

A third experiment was conducted, building upon the results from the dimer studies, to investigate the formation and stability of more complex conformations, representing the next stage of oligomerization that precedes fibril growth - trimers. This approach was motivated by the biological relevance of trimer intermediates, which often act as key nuclei in early amyloid aggregation, bridging the transition between transient dimers and larger protofibril assemblies (12-14). Trimers were constructed in ClusPro using the most conformationally and successfully simulated dimers identified from each of the four pools of successful homo- and hetero- dimer simulations under pH 7 and pH 7.4, respectively. These dimers were treated as receptors and docked with the three highest clusters of Aβ40 and amylin monomers, which were treated as ligands, also derived from the previous monomeric experiments in pH 7 and pH 7.4 simulations. Each combination of trimer was first simulated for 100 ns in triplicate, generating conformations labelled .10, .11, and .12, from which the most stable and well-preserved complexes per homo- or hetero-

oligomer type were extended for an additional 500 ns to reach a cumulative 600 ns simulation time. In cases where a trimer complex dissociated during the initial equilibration phase, the next highest-ranking conformer from the same pool was used instead. These simulations, conducted at both neutral, pH 7 in Table 4.3A, and physiological, pH 7.4 in Table 4.3B, conditions. These provided a comparative framework to evaluate how pH shifts modulate multimeric stability, interface formation, and potential aggregation pathways of Aβ40 and amylin assemblies. Finally, to alleviate concerns of different end-point structures producing more stable conformations at the trimers-stage, start points were taken from the most conformationally stable dimers at 40 ns and repeated the trimerization steps. The results suggested no change because, for all parameters, the different values were within the range of their standard deviations, thus further simulations were performed with structures from the 600 ns endpoint.

4.3 Results and Discussion

4.3.1 pH 7.4 Dimer Analysis

4.3.1.1 Analysing Experimental Parameters for Heterodimers; Aβ40 x Amylin Dimers

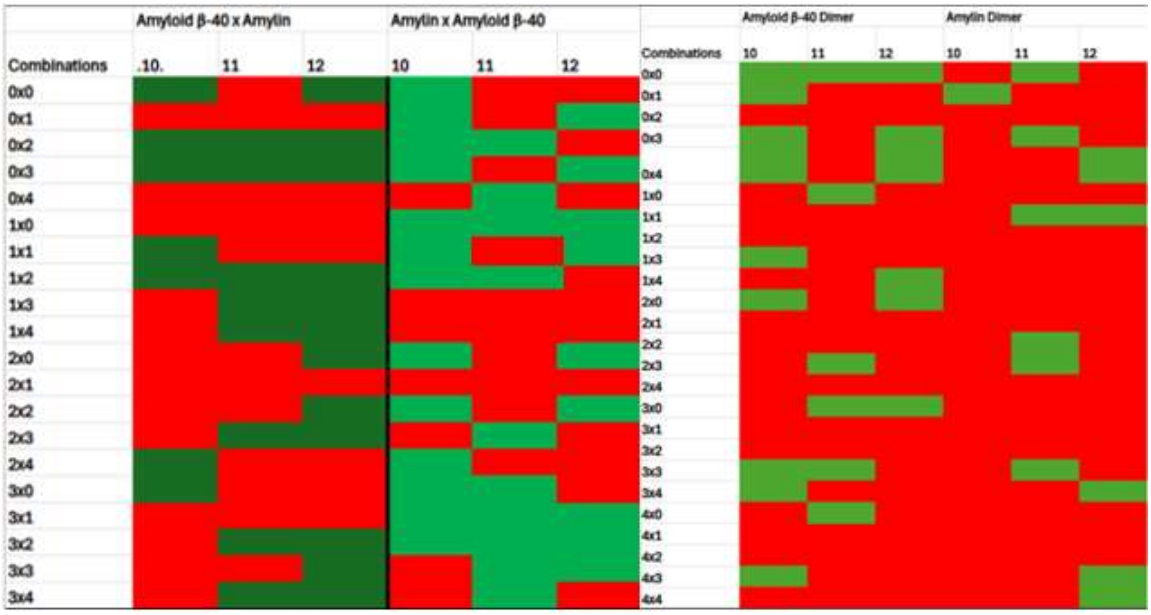

Table 4.1 Simulation results of hetero- and homo- dimers at pH 7.4. Red indicates failures of dimers to remain together while green indicates successes of dimers remaining bonded.

Of the 120 MD simulations of heterodimers, 23.5% of Aβ40 x amylin combinations and 29% of amylin x Aβ40 combinations remained stable over the 100 ns simulation period. In comparison, among the 150 homodimers simulations, 8% of amylin dimers and 14.5% of Aβ40 dimer complexes demonstrated sustained stability under the same conditions in Table 4.1. The lower dimer success rate may be due to a lack of complementary interfacial interactions between the monomers that exist in heterodimers. In heterodimers, the differences in sequence and structure can promote electrostatic and hydrophobic complementarity stabilizing cross-β-like associations and reducing repulsive interactions observed in identical monomer pairings. The homodimers have greater repulsive interactions both physical - both protomers present matching surfaces that do not interlock nor provide as much opportunity for directional interactions, and chemical – identical sidechains mean identical hydrophobic patterns or charges that can destabilize the interface. To alleviate some of these limitations, promising simulations are conducted at a greater 600 ns to allow homodimers more time to find the correct binding register as suggested later. The successful Aβ40 x amylin simulations were analysed first using the root mean square displacement (RMSD) tool of the VMD software providing a rough measurement of their equilibration start points. The simulations reached a plateau after ~20 ns, some of the highest and lowest valued simulations are shown in Figure 4.2. The data for RMSD and Rg analysis was extracted from frames beyond this equilibration point and shown in Table 4.1.1 and 4.1.2 respectively.

RMSD data (Å)

Combinations	**10**	**11**	**12**
0x0	14.8 ± 1.5		11.3 ± 3.4
0x2	10.8 ± 2.2	8.2 ± 1.0	5.4 ± 0.8
0x3	13.7 ± 1.6	13.3 ± 1.6	16.1 ± 1.5
1x1	10.2 ± 3.6		
1x2		13.0 ± 1.6	12.8 ± 1.8
1x3		13.3 ± 1.3	9.4 ± 0.6
1x4		12.7 ± 1.2	14.1 ± 1.7

2x0			11.0 ± 2.8
2x2			11.1 ± 2.0
2x3		8.4 ± 0.8	12.5 ± 1.4
2x4	11.8 ± 1.7		
3x0	11.6 ± 1.8		
3x1			11.7 ± 1.7
3x2		11.9 ± 0.8	
3x3	12.3 ± 2.2	7.9 ± 1.7	
3x4	11.1 ± 1.7	9.7 ± 1.4	

Table 4.1.1. Statistical analysis of RMSD data (Å) of Aβ40 x amylin dimers at pH 7.4. Each combination (0x0, 0x1, 1x2 etc.) denotes the cluster paired in ClusPro.

Most of the RMSD values fall within the 10–16 Å range, implying that the structures underwent a moderate degree of conformational change from their initial ClusPro docked poses. Their relatively low standard deviations (SD), ± 0.60, ± 1.77, indicate that these complexes maintain their conformation stability post-equilibration, fluctuating in a very small range as shown in Figure 4.2. The narrow range of standard deviation values and modest deviations from the starting structures across successful runs indicate that the 100 ns simulation period was sufficient for the complexes to reach equilibrium. The Figure also shows how certain combinations like 0x2.11, 0x2.12, 1x3.12, 2x3.11, 3x3.11 and 3x4.11 have very low RMSD values suggesting a more stable and consistent docking. Alternatively, combinations with higher RMSD values like 0x0.10, 0x3.12, 1x4.12, and 3x2.11 etc. suggests high flexibility that could reflect less stable or more dynamic complexes as show in Figure 4.2. Overall, the clusters involving 0x2, 1x3.12, and 2x3.11 appear among the most promising in terms of sustained binding stability, as evidenced by their low RMSD and SD values. This likely reflects more favourable intermolecular complementarity, possibly driven by stable hydrogen bonding or hydrophobic interactions at the interface. Conversely, complexes exhibiting larger RMSD fluctuations may correspond to weaker or transient contacts that could benefit from extended simulation time or interface refinement. The RMSD behaviour suggests that while

most complexes equilibrated within the 100 ns window, their long-term stability may vary depending on the specific residue interactions governing the dimer interface.

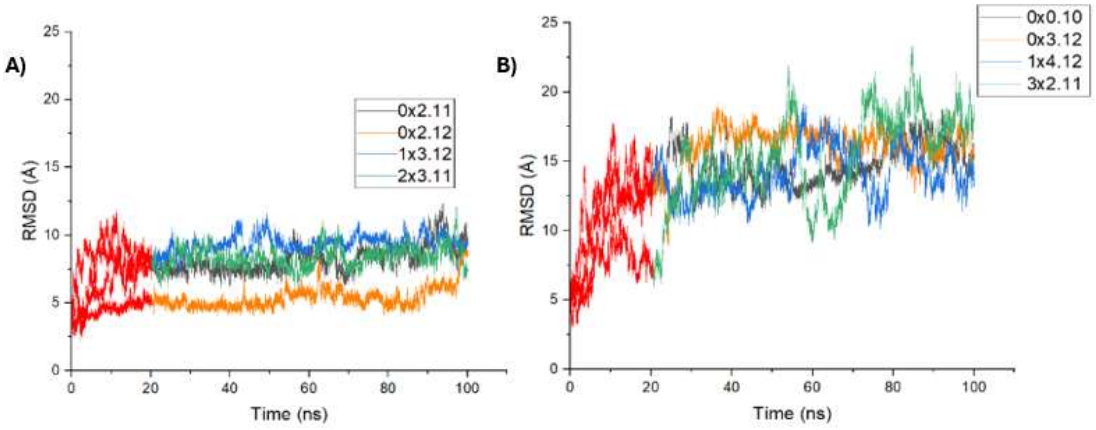

Figure 4.2. RMSD plots of the **A)** least flexible and **B)** most flexible combinations of Aβ-40 x amylin dimer. Red denotes the pre-equilibration data that was discarded.

The post-equilibration Rg data measures the overall molecular size and compactness, indicating whether the dimers adopt tightly packed or more extended conformations. The relatively low SD of Rg values are consistent with the RMSD values ± 0.4, ± 1.8, which further suggests that the peptides' structures remain relatively stable after the first 20 ns of simulation. However, the high Rg value range of 13.05 Å - 17.23 Å suggests that the dimers consistently form a spread-out conformation after 100 ns of simulation. While it was anticipated that lower cluster indices – combinations starting with 0x#, would yield more compact structures due to their higher monomer populations in previous experiments, no consistent pattern can be observed across the different cluster populations (.10, .11, .12) or dimer combinations (e.g., #x#). Only specific combinations of 0x2.11, 0x2.12, 1x1.10, 1x3.12, 1x4.11, and 3x3.11 displayed notably compact structures with Rg values around ~13 Å. Except for 1x1.10 and 1x4.11, these combinations also have the lowest SD values <1.0, suggesting stable conformations with limited fluctuations. By contrast, combinations with higher Rg value range i.e 15-17 Å suggests a more extended structure. Specific combinations like 3x2.11 exhibited a low SD - 0.6, but high Rg value - 15.14 Å, implying that even structurally stable dimers can adopt extended conformations. The absence of a clear pattern across cluster indices or combination pairs indicates that dimer compactness is not primarily governed by cluster order or sequence pairing but rather by the specific orientation and

complementarity of the interacting monomers. As stated previously, variations in side-chain exposure, hydrophobic surface area, and β-strand alignment may play larger roles in determining final stability and compactness of the structure. Notably, Dimer Rg is consistent with a compact associated state and is smaller than what would be expected for two non-interacting peptides separated in space, 10-12 and 12-13 Å for amyloid and amylin respectively, providing evidence consistent with favourable binding interactions in their more compact dimer complexes. The complementary behaviour denoted by RMSD and Rg data reinforces the overall interpretation that most successful simulations have dimers achieving structural equilibrium within 100 ns, while maintaining distinct conformational preferences reflecting the heterogeneity of their binding interfaces.

Rg(Å)

Combinations	**10**	**11**	**12**
0x0	16.5 ± 1.5		15.7±1.8
0x2	14.9 ± 1.9	13.5 ± 0.5	13.2 ± 0.4
0x3	15.2 ± 1.5	15.6 ± 1.8	15.6 ± 1.6
1x1	14.0 ± 1.4		
1x2		14.6 ± 1.7	14.9 ± 1.7
1x3		14.5 ± 1.3	13.1 ± 0.5
1x4		14.0 ± 1.0	16.8 ± 1.8
2x0			14.1 ± 1.2
2x2			14.1 ± 1.9
2x3		14.3 ± 1.1	14.6 ± 1.7
2x4	14.6 ± 1.4		
3x0	15.0 ± 1.0		
3x1			16.1 ± 1.3
3x2		15.1 ± 0.6	
3x3	15.6 ± 1.7	13.4 ± 0.8	

3x4	16.2 ± 1.7	14.7 ± 1.2

Table 4.1.2 Post-equilibration Rg (Å) data for Aβ40 x amylin heterodimers at pH 7.4.

Another measurement often linked to the stability and compactness of a dimer is the Solvent Accessible Surface Area (SASA), which quantifies the extent of atomic and residue exposure to solvent and helps identify interfacial regions critical for aggregation or binding. Table 4.1.3 and 4.3.1 present the SASA values for amyloid x amylin dimers and their monomeric states, respectively. The free monomers show comparable SASA values of approximately 3700 Å². In contrast, the values observed for the dimer combinations are a much lower total, averaging 6156 Å² compared to their monomer's 7428 Å². This 19% reduction is consistent with tighter intermolecular packing and greater residue burial, consistent with the formation of stable binding interfaces. Combinations with the lowest SASA such as 0x2.11, 0x2.12, 1x2.10, 1x3.12, and 3x3.11 - previously identified as having low RMSD and Rg values – also display the most significant reduction in solvent accessibility to binding atoms, reinforcing their classification as the most compact and stable dimers. This is consistent with the previous statistics and could suggest that the heterotypic interface may stabilize secondary structure elements such as β-sheets or helical motifs that drive aggregation.

SASA **(Å²)**

Combinations	**10**	**11**	**12**
0x0	6185 ± 422		6239 ± 509
0x2	6084 ± 521	5807 ± 276	5427 ± 266
0x3	6171± 399	6391 ± 404	6535 ± 356
1x1	6056 ± 500		
1x2		6259 ± 380	6268 ± 389
1x3		6240 ± 331	5737 ± 281
1x4		5993 ± 362	6655 ± 498
2x0			5989 ± 423
2x2			5933 ± 547

2x3			6106 ± 309	6208 ± 474
2x4		6685 ± 540		
3x0		5990 ± 369		
3x1				6527 ± 420
3x2			6003 ± 261	
3x3		6277 ± 507	5759 ± 322	
3x4		6650 ± 531	6027 ± 440	

Table 4.1.3 Post Equilibrium data for Solvent Accessible Surface Area (Å²) for Aβ40 x amylin heterodimer complexes at pH 7.4.

Combinations	***β Sheets %***			***Helices %***		
	10	**11**	**12**	**10**	**11**	**12**
0x0	15		16	12		23
0x2	22	18	17	20	16	22
0x3	14	17	21	21	17	17
1x1	1			33		
1x2		0.9	0.9		35	26
1x3		0.8	3		34	30
1x4		0.3	2		34	30
2x0			1			29
2x2			3			23
2x3		2	2		24	32
2x4	4			22		
3x0	6			21		
3x1			9			19
3x2		11			23	

3x3	6	8	24	25
3x4	8	10	22	27

Table 4.1.4. Statistical data for secondary structures content (%) of Aβ40 x amylin dimers in pH 7.4 implicit environment for 100 ns.

The presence and distribution of secondary structures, including β-sheets (both parallel and anti-parallel forms) and helices (encompassing α-, π-, and 3–10-helices), varies significantly across dimer combinations represented in Table 4.1.4. Combinations like 0x# show greater presence of β- sheets in a range of ~14 – 22%, with 0x2.10 and 0x3.12 exhibiting the highest β-sheet content at 22% and 21%, respectively. Figure 4.4 further illustrates that the 0x2.12 dimer – previously identified as one of the most compact and stable dimers based on Rg and SASA data – also displays a comparatively high β-sheet content. Alternatively, combinations that begin with 1x# and 2x# have very low β- sheets presence at 0.3% - 2% and ~2% - 4% and instead favour helical conformations, with helix content reaching as high as 22–35%. Higher-cluster combinations of 3x# show a mixed pattern, containing moderate β-sheet content ~4 – 10% and slightly lower helical content at 19% - 27%.

Analysis of the corresponding monomeric values can help clarify these trends and suggests how the secondary structures of dimers formed is influenced by the inherent conformational tendencies of their constituent monomers, with limited evidence of structural conversion upon complex formation. Table 4.3.1 shows how amyloid and amylin cluster 0 monomers, which individually exhibit higher β-sheet content at 14% and 0.5% respectively, naturally promote β-rich conformations upon dimerization giving a range of 14-22% in 0x# dimers. A higher proportion of β-sheets may indicate tighter packing between peptide chains and a tendency toward aggregation. However, this trend only weakly correlates to the lower RMSD, Rg, and SASA, since only complexes, 0x2.11 and 0x2.12 showcase higher stability with high sheet content. This suggests structural stability depends not just on secondary structure composition but on how those structural elements are spatially organized at the interface.

At the same time, it is important to note that apparent “stability” in single long trajectories may also reflect kinetic trapping where they’ve fallen into a favourable local energy well rather than because it represents the most robust or reproducible

binding mode. Without independent replicates, low RMSD/Rg/SASA values cannot fully distinguish genuinely preferred interfaces from conformations that are simply trapped on the simulation timescale. A triplicate (or multi-replicate) design with randomized initial velocities would therefore be required to demonstrate that the same stability trends and interface features re-emerge across runs, supporting reproducibility rather than a single “lucky” energy basin.

Alternatively, clusters 1 of both amyloid and amylin show minimal β-sheet, with monomers exhibiting 0.2% and 0.4% sheet content and producing a range of 0.3%-2% in 1x# dimers, and high helical propensities at 31% and 27%, resulting in dimers with predominantly helical secondary structure. Despite having lower sheet content, the structures do not exhibit the expectedly high RMSD, Rg and SASA values, echoing the previous conclusion that β-sheet enrichment alone isn’t the sole determinant of structural stability, their spatially organization also matters.

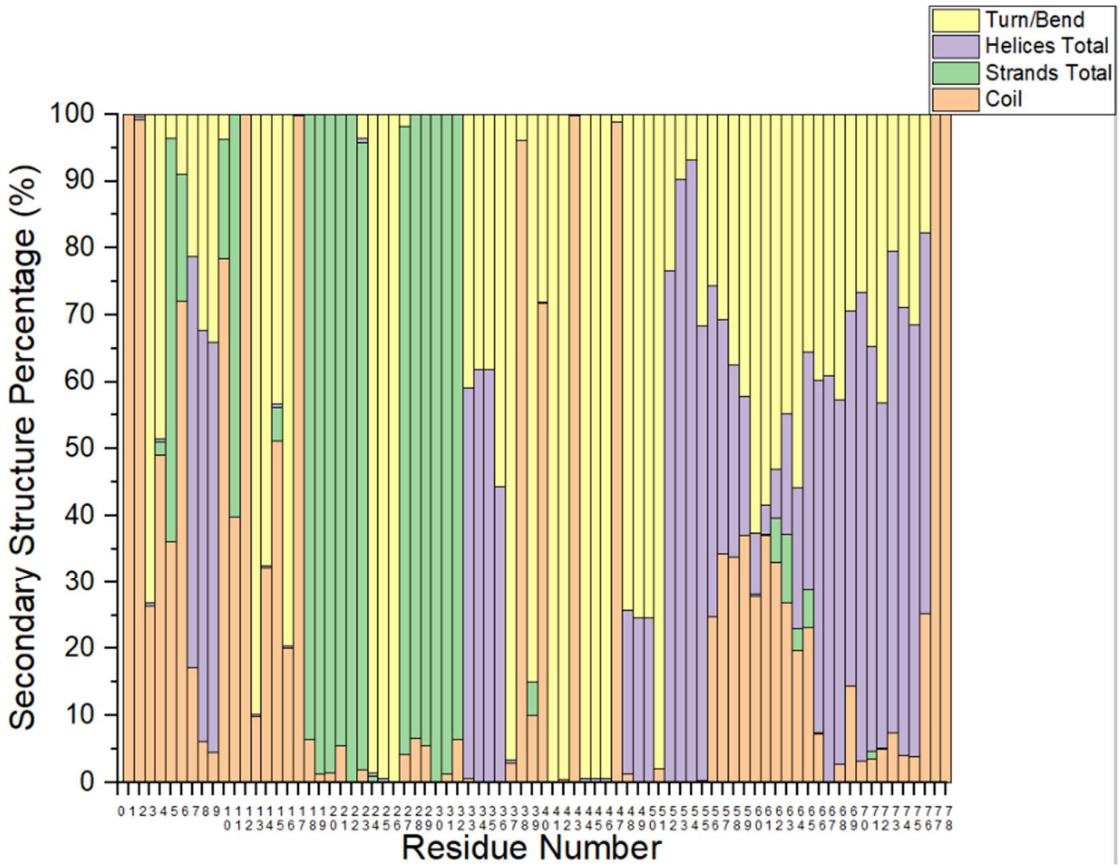

Figure 4.3. Secondary structure composition by residue of the highest β-sheet content (%) as found in the 0x2.12 combination of Aβ40 × amylin dimer at pH 7.4.

The 0x2.12 complex fits the ideal trend of stability mentioned above where the dimers made from the highest population cluster, 0x# dimers, is associated with high β-sheet content because it's the more stable option as reflected by its RMSD, Rg, and SASA values compared to 1x# or 2x#. As it's noted above that observed β-structure alone doesn't guarantee stability, 0x2.12's consistency with providing stable or compact data with all its previous values likely arises from how its secondary structure is localized spatially; hence, its secondary structure analysis per-residue is visualized in Figure 4.3. The composition of various secondary structures in 0x2.12 dimer encompasses the prominent features of each monomer, reflecting the characteristic conformational preferences of both amyloid and amylin peptides. Residues 17-23 and 26-32 of the Central and C-terminal regions, have the highest β-sheets content present, consistent with the aggregation-prone core of Aβ40 that typically drives intermolecular β-sheet stacking during fibril formation. Whereas residues 33-36, and 7-9 of the amyloid peptides have high helical content, suggesting transient helical intermediates that may stabilize early dimeric interfaces before full β-structure conversion. For the amylin component, residues 52–56 and 65–76 also maintain pronounced helical segments, consistent with regions known to preserve secondary structure integrity even under mildly destabilizing pH conditions.

Turn/Bends are more spread out throughout the dimer, showing peaks at residues 12-15, 24-26 and 37-50 which is expected to follow the β-sheets regions. This indicates that these regions are likely flexible hinge points that facilitate conformational rearrangements in the core necessary for nucleation or fibril elongation. Coils mark the N- and C-terminals of each monomer in this dimer, likely arising from the presence of aromatic and non-polar residues like phenylalanine, alanine, valine, and tyrosine etc. that either have neutral charges or hydrophobic side chains, which imparts structural flexibility and prevents them from binding to create rigid complex secondary structures. Additionally, aspartic acid and glutamic acid are negatively charged at pH 7.4 and being present at N-terminus they contribute to electrostatic repulsion, decreasing the ability of other residues from participating in ordered-secondary structures. In the central region residues like non-polar alanine/valine and neutral glycine are prominent which, due to their small side chains and no/few binding regions, gives the central region its high flexibility allowing turns/bends and coils to be formed there.

This structure of 0x2.12 complex, where flexible, unstructured regions are interspersed with β-rich cores suggests that it may adopt a semi-ordered conformation, balancing stability and adaptability. Such conformational heterogeneity may facilitate dynamic rearrangements at the dimer interface, a property essential for subsequent oligomerization or fibril nucleation events. These findings reinforce the notion that local sequence composition, particularly the distribution of charged and hydrophobic residues, plays a key role in modulating the balance between helical and β-sheet content during early stages of amyloid assembly.

Protonation fractions can be used to understand and predict behaviour, reactivity, and function of molecules in different environments where pH plays a critical role. The histidine residues of the dimers situated in a pH 7.4 environment showcase fractional deprotonation in Tables 4.1.5, 4.1.6 and 4.1.7 with each table representing the one of the 3 highest clusters chosen for simulation.

	Protonated Residues				
Combinations	**HIP6**	**HIP13**	**HIP14**	**HIP58**	**Predicted Charge (lel)**
0x0	0.17	0.62	0.16	0.04	1.0
0x2	0.04	0.24	0.09	0.17	0.54
0x3	0.26	0.71	0.30	0.07	1.34
1x1	0.20	0.21	0.06	0.17	0.64
1x2					
1x3					
1x4					
2x0					
2x2					
2x3					
2x4	0.06	0.10	0.13	0.31	0.6
3x0	0.41	0.21	0.50	0.12	1.24
3x1					

3x2					
3x3	0.11	0.09	0.01	0.21	0.42
3x4	0.22	0.20	0.21	0.22	0.85

Table 4.1.5. Protonated Fractions of histidine in successful Aβ40 x amylin dimers combinations of the highest order (.10).

	Protonated Residues				
Combinations	**HIP6**	**HIP13**	**HIP14**	**HIP58**	**Predicted Charge (lel)**
0x0					
0x2	0.10	0.80	0.33	0.17	1.40
0x3	0.32	0.37	0.15	0.26	1.10
1x1					
1x2	0.29	0.04	0.06	0.08	0.47
1x3	0.16	0.15	0.06	0.92	1.29
1x4	0.43	0.12	0.08	0.39	1.02
2x0					
2x2					
2x3	0.67	0.11	0.04	0.04	0.86
2x4					
3x0					
3x1					
3x2	0.44	0.17	0.05	0.16	0.82
3x3	0.26	0.20	0.31	0.16	0.93
3x4	0.55	0.09	0.07	0.35	1.06

Table 4.1.6 Protonated fractions of histidine residues from the 2nd most populated cluster (.11) selected for each Aβ40 x amylin dimers combination.

	Protonated Residues				

Combinations	HIP6	HIP13	HIP14	HIP58	Predicted Charge (Iel)
0x0	0.09	0.77	0.21	0.11	1.18
0x2	0.00	0.57	0.36	0.16	1.09
0x3	0.12	0.96	0.19	0.10	1.37
1x1					
1x2	0.33	0.09	0.04	0.08	0.54
1x3	0.12	0.13	0.20	0.27	0.72
1x4	0.31	0.20	0.14	0.17	0.82
2x0	0.25	0.00	0.11	0.05	0.41
2x2	0.20	0.19	0.17	0.08	0.64
2x3	0.41	0.09	0.13	0.23	0.86
2x4					
3x0					
3x1	0.34	0.06	0.35	0.06	0.81
3x2					
3x3					
3x4					

Table 4.1.7 Protonated fractions of histidine of the 3rd highest cluster population (.12) Aβ40 x amylin dimers.

Analysis of protonated histidine residues is important because it can highlight how these interfacial residues facilitate cation–π and salt-bridge interactions with nearby aspartate or glutamate residues, impacting the structure and stability of the dimers. These interactions are critical for early-stage nucleation and cross-seeding in both Aβ40 and amylin aggregation for when histidine residues become partially deprotonated, these stabilizing interactions weaken, increasing structural flexibility and influencing the peptide's aggregation pathway. The data shows an incomplete protonation of histidine at various points across each complex, while a general partial deprotonation is expected given that pH 7.4 lies close to the imidazole side chain's

pKa (~6.8) the far smaller protonation values in Tables 4.1.7 like 0.09 for complex 0x0.12 or 0.05 for complex 3x2.11 etc. suggests a geometric or environmental contribution to the deprotonation that those histidine residues are experiencing. It suggests unfavourable electrostatics or solvent exposure which contributes to lower protonation. His13 of Aβ40 and His58 of amylin often display high protonation fractions (0.7–0.9) in lower-order dimers (0×# and 1×#), yet these values drop sharply to 0.04–0.1 in higher-order complexes (3×#), indicating an order-dependent shift in microenvironment and electrostatic potential. However, this pattern is weak since there are generally low protonation values across many combinations and other residues that do not reach the same peaks as His13 or His58, likely due to solvent accessibility and altered local dielectric environments evidenced by the predicted charge values, which range roughly from +0.4 to +1.4 across complexes. Such differences likely influence the balance between electrostatic repulsion and attraction within the dimer interface, modulating the strength and frequency of cation–π and salt-bridge interactions with nearby aspartate or glutamate residues. Yet, in configurations where histidine residues remain mostly protonated (e.g., HIP13 in Tables 4.1.5 and 4.1.7, or HIP6 in Table 4.1.6), it is likely that these residues are well positioned to engage in cation–π interactions or form salt bridges with neighbouring carboxylate groups to stabilize β-structured motifs and limit conformational entropy as noted by the greater β-sheet content in higher-order complexes of table 4.1.4.

Dimers	***10***			***11***			***12***		
	ΔH ± SD	**TΔS ± SD**	**ΔG ± SD**	**ΔH ± SD**	**TΔS ± SD**	**ΔG ± SD**	**ΔH ± SD**	**TΔS ± SD**	**ΔG ± SD**
0x0	-23.1 ± 12.7	-24.0 ± 6.2	+0.9 ± 14.1				-25.6 ± 6.7	-24.4 ± 2.5	-1.2 ± 7.1
0x2	-30.2 ± 12.9	-26.1 ± 7.0	-4.1 ± 14.8	-44.3 ± 10.1	-27.5 ± 4.7	-16.9 ± 10.8	-54.0 ± 15.3	-43.2 ± 6.6	-10.8 ± 16.8
0x3	-39.4 ± 8.5	-34.5 ± 6.1	-4.9 ± 10.5	-34.1 ± 8.3	-30.4 ± 10.6	-3.6 ± 13.0	-44.2 ± 11.4	-35.0 ± 18.4	-9.2 ± 19.0
1x1	-53.6 ± 9.8	-43.8 ± 6.7	-9.9 ± 12.3						
1x2				-38.6 ± 10.6	-40.0 ± 5.0	+1.4 ± 11.5	-29.9 ± 7.8	-27.5 ± 7.3	-2.5 ± 10.4
1x3				-67.1 ± 14.2	-55.7 ± 3.8	-11.4 ± 14.9	-75.6 ± 9.3	- 43.0 ± 6.7	-32.6 ± 11.6
1x4				-45.3 ± 13.8	-34.9 ± 8.2	-10.4 ± 16.5	-27.3 ± 5.8	-28.6 ± 7.0	1.3 ± 8.8
2x0							-59.4 ± 10.8	-38.4 ± 4.4	-21 ± 11.9
2x2							-71.6 ± 9.3	-40.9 ± 2.9	-30.7 ± 9.8
2x3				-29.6 ± 10.9	-39.7 ± 12.0	+10.1 ± 16.5	464.2 ± 15.7	36.3 ± 5.9	427.9 ± 16.7
2x4	-46.3 ± 8.1	-30.8 ± 3.1	-15.5 ± 8.9						
3x0	-30.3 ± 8.0	-26.1 ± 4.8	-4.2 ± 9.6						
3x1							-29.6 ± 13.4	-32.7 ± 1.9	3.1 ± 13.5
3x2				-80.7 ± 9.2	-37.2 ± 6.7	-42.9 ± 11.5			

3x3	-25.6 ± 11.5	-33.0 ± 3.9	7.3 ± 12.1	-55.9 ± 10.5	-44.5 ± 9.0	-11.5 ± 13.8
3x4	-56.7 ± 11.1	-41.9 ± 7.0	-14.9 ± 13.2	-62.5 ± 9.0	-41.8 ± 9.3	-20.7 ± 13.4

Table 4.1.8. Binding free energy *ΔG (kcal/mol)* calculations with standard deviations of enthalpic and normal mode entropic contributions to the calculation of Aβ40 x amylin dimer values across 95-100 ns at pH 7.4.

The calculated binding energy in Table 4.1.8 shows many combinations with relatively high Gibbs Free Energy around –1 and –10 suggesting exergonic binding. Meanwhile, combinations like 0x2.11, 1x3.12, 2x2.12, 3x2.11 and 3x4.11 that have the most spontaneous exergonic reactions with very low ΔG of –16 to –43 show how those dimers are among the most thermodynamically favourable. Such negative free energy values are in-line with the previously made assumptions reinforcing the role of hydrophobic interactions and favourable electrostatics at binding interfaces in the formation of this stable structure, reflecting strong complementarity between the peptide surfaces. In contrast, some reactions are unfavourable with positive ΔG representing non-spontaneous endergonic combinations that are less likely to form under physiological conditions. Amongst these, combinations 2x3.12 has the highest positive binding free energy value of 428 kcal mol^{-1} and is considered an anomaly. Cross-referencing the visual details through PyMol with the data of per-residue decomposition revealed that these values arose from ClusPro combining the monomers into a non-physical conformation, where the electrostatic energy is enough to hold them despite very high van der Waals repulsions arising from unfavourable sidechains intersecting each other in the simulated space. For subsequent analysis, these are marked as unsuccessful simulations.

The standard deviations in binding free energy for most combinations are mostly consistent within the 11-19 range, suggesting considerable energetic variation likely reflecting the inherent flexibility of amyloidogenic peptides and the sensitivity of MM/GBSA scoring to conformational sampling. Where ΔG values approach 0, high SD values undermine statistical confidence, indicating that transient or weakly bound dimers may not represent stable interaction states. This variability may be due to the compromises made for computational costs and time-efficiency alongside replicability, discussed later in this chapter. Only 5 combinations have SD values in the 5-10 range, indicating more stable and statistically significant structures where interactions are less sensitive to input variations/noise. Complexes 0x2.11 and 1x3.12 are likely the best combinations to continue analysis on at higher runtimes

because of their values of Gibbs Free Energy and SD values and SASA being low. Backed by their RMSD, Rg, and secondary structure analysis, these dimers likely represent among the most biologically plausible intermediates amongst the 270+ simulations. Their stable and compact configurations may provide nucleation templates conducive to further oligomerization, linking thermodynamic stability to early aggregation pathways relevant to amyloid–amylin cross-seeding.

4.3.1.2 Comparing the Heterodimer Reciprocals Amylin x Aβ40 Dimers

Combinations	*RMSD (Å)*	*Rg (Å)*	*β-Sheet (%)*	*Helices (%)*	*ΔG (kcal/mol)*	*SASA (Å²)*
0x0.10	10.7 ± 3.0	15.6 ± 2.1	10	22	-9.7 ± 12.4	6378 ± 488
0x1.10	9.4 ± 1.4	14.2 ± 1.1	1	27	-7.1 ± 8.1	6164 ± 343
0x1.12	8.1 ± 2.0	15.6 ± 1.8	1	34	+31.8 ± 13.1	6375 ± 382
0x2.10	6.8 ± 1.0	12.9 ± 0.4	0.3	29	-12.5 ± 2.6	5526 ± 249
0x2.11	12.3 ± 2.0	14.9 ± 1.5	1	23	-35.9 ± 1.2	6006 ± 460
0x3.10	10.2 ± 2.1	14.4 ± 1.0	9	23	-20.9 ± 3.4	5870 ± 324
0x3.12	9.0 ± 2.8	14.2 ± 1.1	9	31	-16.1 ± 3.2	5954 ± 333
0x4.11	13.3 ± 2.4	19.1 ± 2.4	0.4	28	-11.5 ± 8.0	6660 ± 442
1x0.10	10.9 ±3.1	14.5 ± 1.01	18	22	+27.8 ± 13.6	6058 ± 332
1x0.11	9.9 ± 1.6	17.1 ± 1.3	15	16	-10.8 ±16.7	6525 ± 326
1x0.12	6.1 ± 1.3	13.1 ± 0.4	17	23	-15.0 ±13.4	5723 ± 254
1x1.10	10.4 ± 1.7	15.6 ± 1.9	1	36	-8.6 ± 6.2	6136 ± 427
1x1.12	13.5 ± 2.1	17.0 ± 1.3	0.3	32	-2.7 ± 7.8	6576 ± 383
1x2.10	12.8 ± 2.9	15.3 ± 1.3	5	21	+12.1 ± 18.6	6254 ± 364
1x2.11	8.2 ± 2.4	13.8 ± 1.7	3	23	-7.8 ± 10.4	5771 ± 406
2x0.10	9.2 ± 3.1	15.0 ± 1.5	19	19	-3.2 ± 14.6	6264 ± 484

2x0.12	5.5 ± 1.2	13.4 ± 0.5	17	21	-19.3 ± 0.9	5696 ± 271
2x2.10	34.1 ± 7.2	16.0 ± 7.2	3	19	-52.2 ± 8.7	5920 ± 641
2x2.12	11.2 ± 3.4	16.6 ± 1.5	7	20	-25.4 ± 0.2	6539 ± 455
2x3.11	8.0 ± 3.7	14.8 ± 1.7	8	23	-8.8 ± 17.9	6007 ± 411
2x4.10	12.4 ± 2.9	15.0 ± 1.7	3	32	-2.5 ± 12.6	6133 ± 407
3x0.10	9.2 ± 1.5	15.1 ± 1.6	10	24	-8.0 ± 10.7	6104 ± 380
3x0.11	6.7 ± 1.1	13.1 ± 0.3	13	19	-6.8 ± 9.1	5611 ± 239
3x1.10	12.0 ± 4.5	17.4 ± 3.5	1	32	+3.8 ± 11.1	6527 ± 627
3x1.11	9.0 ± 1.3	17.2 ± 1.7	1	29	+13.5 ± 8.4	6435 ± 305
3x1.12	10.4 ± 1.9	13.6 ± 1.1	1	34	+5.3 ± 12.8	5856 ± 442
3x2.10	7.4 ± 1.2	14.0 ± 1.1	4	26	-20.2 ± 4.3	6011 ± 420
3x2.11	10.2 ± 2.2	14.8 ± 1.0	4	25	-6.8 ± 7.1	6217 ± 364
3x2.12	9.2 ± 2.8	14.0 ± 1.2	3	26	-7.5 ± 10.6	5777 ± 412
3x3.11	8.9 ± 2.1	13.6 ± 0.7	2	23	-1.9 ± 8.5	5869 ± 325
3x3.12	11.3 ± 2.5	15.6 ± 1.2	12	21	-2.7 ± 11.6	6507 ± 457
3x4.11	14.0 ± 4.3	17.0 ± 3.4	2	25	-4.8 ± 9.0	6334 ± 524

Table 4.2.1 Statistical Results of RMSD (Å), Rg (Å), secondary structure content (%), solvent accessible surface area and Gibbs Free energy (binding free energy) for amylin x Aβ40 heterodimer at pH 7.4.

Notably, all combinations involving Aβ40 cluster 0 exhibited elevated β-strand content (≥10%), reinforcing earlier conclusions that Aβ40's cluster 0 monomer contributes a strong structural bias toward β-rich aggregation motifs, even upon dimerization. The prevalence of β-structure also suggests that the intrinsic secondary structure preferences of the monomers may continue to dictate the behaviour and structure of the dimer complex. The coexistence of both β- and α-regions across multiple combinations, aligns with previous Aβ40 x amylin dimer data, indicating that dimerization does not induce large-scale structural conversion but instead stabilizes a hybrid architecture where both elements remain partially retained as backed by the

data presented by *Abedini A. et al.* and *Qi R. et al* (15, 16) and illustrated in Figure 4.5.2 for my simulations.

The low SASA values for the reciprocal simulations reflect in the structure compact interfaces with limited solvent exposure; yet none have achieved the exceptionally low SASA values observed in the reciprocal heterodimers, reinforcing the previously espoused trend of directional asymmetry in binding efficiency. When molecular orientation is reversed, steric complementarity and side-chain electrostatics are optimized differently, leading to tighter interfacial packing in one docking direction compared to the other.

Finally, the binding free energy (ΔG) distribution mirrors previously reported results, most clusters have low ΔG values (-8 kcal mol^{-1}) with a few outliers (–35 to –52 kcal mol^{-1}) suggesting highly exergonic, potentially aggregation-nucleating conformations. These energetically favourable dimers correspond closely to those previously identified as most stable 0x2.11, 0x3.10, confirming the robustness of earlier conclusions across independent simulations. However, just like before high SD values (11 - 19) persist across much of the dataset as well, consistent with the flexible and disordered nature of both peptides. This is consistent with the earlier conclusion that the Aβ40 cluster 0 monomer contributes a structural bias, with only a subset of orientations achieving the structural complementarity and electrostatic balance required for long-lived complexes.

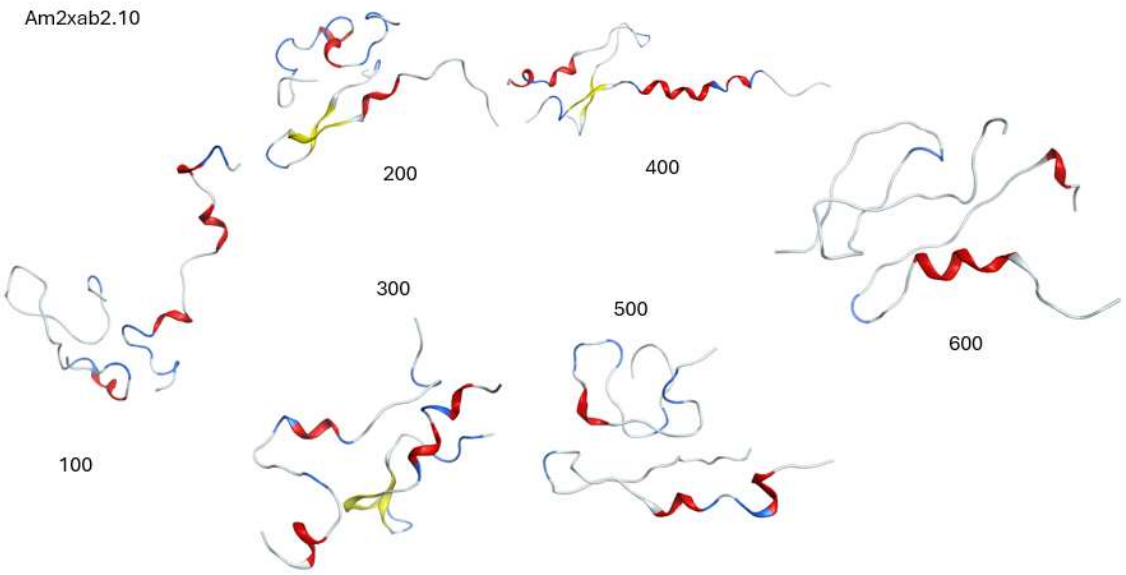

Figure 4.4 Snapshots of the “bad” heterodimer complex 2x2.10 at 100 ns intervals for 600 ns CpHMD.

Certain complexes, specifically 2x2.10 and 3x1.10 are considered anomalous because their extremely high SD values for Rg or RMSD, being twice as large as the average SD, suggests increased flexibility or influence of partial dissociation events during the simulation as suggested in Figure 4.4 at the 200 ns, 500 ns and 600 ns mark. Other “bad” dimers are 1x2.10, 3x1.11-3x.1.12, 1x0.10 and 0x1.12, that have high standard deviations alongside positive Gibbs free energy values, indicating structural instability and poor binding affinity. The positive ΔG values and large standard deviations in these outliers underscore weak or nonspecific interactions likely driven by steric mismatch or charge repulsion at the interface. Their unfavourable values also suggests that these dimers likely occupy transient, weakly associated states that are less likely to persist under physiological conditions or contribute meaningfully to aggregation pathways. Contrastingly, previously noted complexes 0x2.10, 0x2.11, and 2x2.12 are considered “good” exhibiting a balance between moderate flexibility (RMSD ~7–10 Å), compactness (Rg ~13–15 Å), and consistently low binding energy (ΔG values; –12.5, –35.9, and –25.4 kcal mol^{-1} , respectively), illustrated in Figure 4.5.1. The relatively low SASA (5500–6000 $Å^2$) of these stable dimers further supports this interpretation, indicating compact, well-buried interfaces which could be carried forward into later simulations.

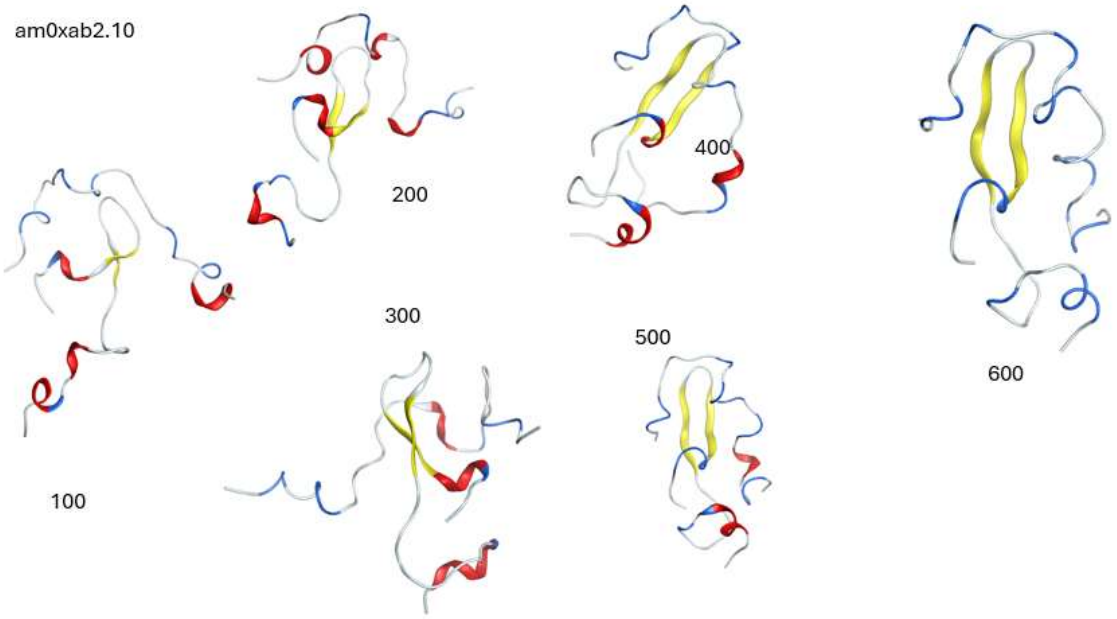

Figure 4.5.1 Snapshots of “good” heterodimer complex 0x2.10 at 100 ns intervals across 600 ns CpHMD.

Table 4.2.2 shows that histidine residues are mostly partially deprotonated at pH 7.4, with occasional higher protonated fractions depending on the local microenvironment, consistent with their ionization states near physiological pH. Nonetheless, occasional instances of partially protonated histidine residues persist across several combinations, albeit inconsistently. Such heterogeneity may introduce localized electrostatic instability, subtle modulation of inter-chain attraction and contributing to the observed conformational variability among dimers. Further analysis below expands upon this point.

	Protonated Residues				
	HIP18	**HIP44**	**HIP51**	**HIP52**	**Predicted Charge (Iel)**
0x0.10	0.12	0.12	0.66	0.37	1.27
0x1.10	0.04	0.35	0.16	0.07	0.62
0x1.12	0.47	0.03	0.17	0.07	0.74
0x2.10	0.08	0.52	0.00	0.12	0.72
0x2.11	0.28	0.12	0.07	0.13	0.6
0x3.10	0.11	0.49	0.10	0.21	0.91
0x3.12	0.30	0.38	0.14	0.46	1.28
0x4.11	0.20	0.30	0.01	0.04	0.55
1x0.10	0.04	0.04	0.22	0.03	0.33
1x0.11	0.05	0.17	0.34	0.30	0.86
1x0.12	0.03	0.07	0.82	0.34	1.26
1x1.10	0.16	0.47	0.10	0.12	0.85
1x1.12	0.12	0.54	0.10	0.06	0.82
1x2.10	0.02	0.17	0.04	0.22	0.45
1x2.11	0.09	0.14	0.01	0.09	0.33

2x0.10	0.35	0.26	0.87	0.24	1.72
2x0.12	0.12	0.18	0.17	0.02	0.49
2x2.10	0.03	0.46	0.02	0.10	0.61
2x2.12	0.07	0.48	0.03	0.14	0.72
2x3.11	0.23	0.33	0.15	0.34	1.05
2x4.10	0.15	0.15	0.02	0.07	0.39
3x0.10	0.18	0.12	0.39	0.11	0.8
3x0.11	0.01	0.02	0.93	0.03	0.99
3x1.10	0.11	0.16	0.11	0.10	0.48
3x1.11	0.10	0.12	0.06	0.40	0.68
3x1.12	0.10	0.17	0.00	0.03	0.3
3x2.10	0.01	0.13	0.16	0.18	0.48
3x2.11	0.05	0.41	0.07	0.06	0.59
3x2.12	0.14	0.24	0.02	0.14	0.54
3x3.11	0.03	0.23	0.12	0.34	0.72
3x3.12	0.13	0.22	0.15	0.18	0.68
3x4.11	0.07	0.22	0.09	0.08	0.46

Table 4.2.2 Protonation dataset for amylin x amyloid dimers at pH 7.4**.**

Amylin × amyloid dimer dataset reveals partial and variable protonation of histidine residues (HIP18, HIP44, HIP51, HIP52), with fractional protonation values ranging from ~0.01 to ~0.87, highlighting the dynamic equilibrium between protonated (cationic) and neutral forms of histidine, consistent with the previously established chemical behaviour of the imidazole side chain. The average predicted charge values (~+0.7) indicates that most dimers sustain only moderate net protonation, consistent with a moderately charged system and a potentially dynamic interface. The charge may be low enough to limit strong long-range repulsions and while still allowing cation–π interactions and salt-bridge formation where geometrically accessible. The positive charge and the lower protonation states compared to the

other heterodimer also aligns with their differences in secondary structures; the amylin × Aβ40 heterodimer's lower beta sheets in this context could indicate a more dynamic, solvent exposed interface that has greater tolerance for conformational change which could make them more permissive intermediates for cross-aggregation. While higher protonation fractions (0.87, 0.82), as seen in dimers such as 2×0.10 or 1×0.12, likely arise from favourable electrostatic and hydrogen-bonding interactions, particularly at buried or electrostatically shielded histidine residues that be stabilized by hydrogen bonding and/or salt-bridge interactions, favouring proton retention. As a result, they also have elevated positive charges (1.27, 1.72) that may also introduce repulsion effects yet coincide with some of the more compact structures present with strong β-sheet presence potentially due to stronger hydrogen bonding and aromatic interactions. Conversely, clusters with lower protonation fractions (~0.3) suggest a solvent-exposed histidine environment, where proton competition from surrounding water molecules promotes partial neutralization and increased conformational flexibility.

A weak order-dependent trend is apparent with previous findings from the amyloid × amylin dataset (Table 4.2.1). Lower-order dimers (0x#, 1x#) include several cases with higher protonated fractions (~0.66–0.85), which may reflect greater compactness and stability with those complexes. Conversely, higher-order clusters (2×# and 3×#) show slightly reduced protonation, consistent with extended, solvent-accessible geometries where protonated residues experience dielectric screening and diminished cation–π or salt-bridge potential. Overall, the trends reinforce the trends observed in Aβ40 × amylin systems: histidine residues function as sensitive electrostatic modulators, adjusting their charge states to stabilize early-stage interfaces or promote flexibility during aggregation transitions. These protonation shifts underscore the interplay between structure compactness, electrostatic balance, and solvent exposure in modulating histidine protonation.

4.3.1.3 Monomers at pH 7.4

	RMSD (Å)	***Rg (Å)***	**β *Sheets (%)***	***Helices (%)***	***SASA (Å²)***
Amc0	7.1 ± 1.1	13.5 ± 2.3	0.5	26	3611 ± 247

Amc1	8.2 ± 1.3	12.2 ± 1.7	0.4	27	3414 ± 249
Amc2	10.1 ± 2.3	14.2 ± 3.2	0.3	21	3652 ± 326
Amc3	8.8 ± 1.8	12.2 ± 1.8	2	22	3460 ± 268
Amc4	8.2 ± 1.2	13.0 ± 1.7	0.2	26	3593 ± 248
Abc0	9.8 ± 2.0	13.0 ± 2.4	14	9	3817 ± 362
Abc1	9.1 ± 3.4	13.0 ± 2.8	0.2	31	3768 ± 379
Abc2	5.0 ± 1.5	10.3 ± 0.4	3	27	3431 ± 202
Abc3	3.2 ± 1.0	10.6 ± 0.5	8	24	3261 ± 193

Table 4.3.1. Results of RMSD (Å), Rg (Å), secondary structure content (%) and solvent accessible surface area for pH 7.4.

	Deprotonation			
	HIP6	**HIP13**	**HIP14**	**Average Predicted Protonation**
Abc0	0.695	0.644	0.805	6.99
Abc1	0.587	0.830	0.772	6.95
Abc2	0.770	0.958	0.858	6.51
Abc3	0.158	0.797	0.635	7.36
	HIP18		**Average Predicted Protonation**	
Amc0	0.862		6.61	
Amc1	0.920		6.34	
Amc2	0.910		6.34	
Amc3	0.917		6.36	
Amc4	0.933		6.26	

Table 4.3.2 Fractional Deprotonation results for the amyloid and amylin monomers

Table 4.3.1 helps assess if the previously established idea that dimers retain their intrinsic conformational tendencies established in their monomers is true or not and

instead dimerization induces new structural and energetic characteristics. The results of the highest monomer cluster simulations are represented via a numerical rank based on the clusters population size and denoted with an abbreviation for whether it is an Aβ40 cluster (i.e Abc) or amylin cluster (i.e Amc). Amylin exhibits high helical content (21-27%) and low β sheets (≤ 2%), while Aβ40 monomers show variable β-sheet content (3–14%) and a broader yet on-average higher range of helical content (9–31%). These values and trends are reflected in the heterodimers – combinations involving amyloid cluster 0 consistently yields β-rich dimers, while amylin-containing regions contributed more α-helical organization at ~25%, suggesting that dimer secondary structures are largely inherited rather than newly formed. This is also consistent with Figure 4.3 where the amylin subunit has a higher helical content than the amyloid, and the latter more β-sheets. This is backed by the SASA values, where amyloid monomers exhibit higher SASA (3430–3817 Å²) than amylin (3410–3650 Å²), which may correlate with differences in secondary structure content and more extended configurations. The deprotonated fractions of individual proteins, represented in Table 4.3.2, are also consistent with the dimer's data indicating that the behaviour of the individual monomers and their protonation equilibria may be broadly maintained upon dimer formation, reinforcing that their fundamental electrostatic profiles persist upon dimerization.

From a structural perspective, the 3-10 Å and 10-14 Å RMSD and Rg respective values for monomers are noticeably lower than their dimer counterparts. These differences are consistent with what is expected of larger and more conformationally diverse dimers. The standard deviations remaining similar (≈ 1–3 Å), perhaps correlates another intrinsic value between the structures, it may be highlighting the range within which stable amyloid and amylin conformations achieve stable equilibria. Finally, SASA values of monomers upon dimerization, typically decreases, indicating a burial of binding sites and hydrophobic residues, which can be associated to aggregation-prone behaviour. These findings back the previously established point of cross-aggregation being cooperative between the two peptides rather than transformative, where native conformational preferences dominate the resulting structural ensemble.

4.3.1.4 Comparing Amylin and Amyloid Homodimers

Amylin Combination	*RMSD (Å)*	*Rg (Å)*	*β Sheets (%)*	*Helices (%)*	*ΔG (kcal mol⁻¹)*	*SASA (Å²)*
0x0.11	11.7 ± 1.6	17.07 ± 1.9	6	22	-8.6 ± 9.7	6145 ± 337
0x1.10	11.5 ± 2.4	15.7 ± 1.5	1	30	+0.3 ± 11.7	6389 ± 395
0x3.11	10.5 ± 1.7	14.4 ± 1.1	1	20	-25.6 ± 11.3	5860 ± 447
0x4.12	10.6 ± 2.2	14.7 ± 1.2	1	28	-92.9 ± 10.5	5992 ± 282
1x1.11	10.8 ± 5.3	16.4 ± 2.4	0.2	34	+9.5 ± 12.3	6166 ± 523
1x1.12	11.9 ± 1.7	16.0 ± 1.5	0.2	24	-14.8 ± 9.7	6153 ± 444
2x2.11	5.7 ± 1.1	12.1 ± 0.3	0.8	17	-22.4 ± 13.7	4997 ± 263
2x3.11	13.5 ± 2.3	15.4 ± 1.8	3	19	+16.7 ± 16.3	6197 ± 519
3x3.11	10.8 ± 3.8	15.5 ± 1.7	0.7	27	-6.4 ± 24.1	6098 ± 432
3x4.12	13.0 ± 2.5	16.3 ± 1.8	4	24	-14.6 ± 13.1	6413 ± 453
4x3.12	15.0 ± 5.5	18.4 ± 4.1	0.7	29	+0.2 ± 11.5	6659 ± 538
4x4.12	10.2 ± 3.1	15.2 ± 1.3	3.5	29	-7.0 ± 19.1	5985 ± 431

Table 4.4.1 Statistical results of RMSD (Å), Rg (Å), secondary structure content (%), solvent accessible surface area, and binding free energy for amylin homodimers at pH 7.4.

Abxab Combination	*RMSD (Å)*	*Rg (Å)*	*β Sheets (%)*	*Helices (%)*	*ΔG (kcal mol-1)*	*SASA (Å²)*
0x0.10	7.00 ± 1.3	14.54 ± 0.8	23	10	-14.12 ± 12.2	6158 ± 277

0x0.11	7.10 ± 1.5	16.03 ± 1.0	30	12	-18.03 ± 11.2	6545 ± 337
0x0.12	7.10 ± 1.6	14.37 ± 1.1	30	14	-11.19 ± 10.2	6089 ± 391
0x1.10	10.08 ± 2.2	15.27 ± 1.0	11	28	-14.32 ± 6.8	6380 ± 303
0x3.10	8.70 ± 1.9	15.19 ± 1.0	19	20	-24.39 ± 10.1	6430 ± 420
0x3.12	9.40 ± 1.9	14.41 ± 1.0	21	16	+8.40 ± 11.0	6428 ± 344
0x4.10	6.92 ± 1.4	13.98 ± 0.6	19	18	-15.45 ± 9.1	6233 ± 305
0x4.12	10.63 ± 1.9	15.98 ± 1.1	20	13	+0.45 ± 16.3	6691 ± 374
1x0.11	12.6 ± 4.2	16.4 ± 2.6	15	23	+2.94 ± 17.3	6780 ± 539
1x3.10	14.01 ± 3.0	18.59 ± 3.0	5	23	-29.06 ± 10.3	7422 ± 494
1x4.12	12.93 ± 1.9	16.39 ± 1.8	4	24	-7.40 ± 13.9	6839 ± 441
2x0.10	11.72 ± 2.9	15.35 ± 1.3	17	17	-0.12 ± 12.7	6473 ± 440
2x0.12	9.13 ± 2.3	15.04 ± 0.8	12	19	+0.45 ± 8.2	6430 ± 342
2x3.11	5.50 ± 1.1	14.39 ± 0.7	15	27	-4.04 ± 9.9	6087 ± 261
3x0.11	6.28 ± 1.4	14.57 ± 0.8	15	21	-9.45 ± 13.0	6487 ± 388
3x0.12	7.67 ± 2.6	14.23 ± 0.7	15	18	+0.38 ± 6.2	6243 ± 342
3x3.10	3.8 ± 0.8	13.00 ± 0.3	14	25	-25.78 ± 14.5	5385 ± 351

3x3.11	9.56 ± 2.8	14.55 ± 1.0	14	20	+6.12 ± 11.0	6582 ± 380
3x4.10	7.97 ± 1.3	13.39 ± 0.4	11	22	-25.41 ± 17.8	5810 ± 281
4x0.11	25.62 ± 12.9	36.30 ± 14	17	10	-7.90 ± 2.5	7154 ± 381
4x3.10	13.36 ± 2.2	14.29 ± 1.6	8	22	-25.72 ± 17.3	6280 ± 487

Table 4.4.2 Statistical results of RMSD (Å), Rg (Å), secondary structure content (%), solvent accessible surface area and binding free energy for amyloid homodimers at pH 7.4.

Comparative analysis of amylin and amyloid homodimer data, presented in Tables 4.4.1 and 4.4.2, reveals clear differences in their structural behaviour and stability profiles as expected. Amyloid homodimers display lower RMSD values (~7-10 Å) and Rg values (~14-15 Å) than their amylin counterparts (RMSD at 10–14 Å and Rg values at 15–17 Å), suggesting greater conformational stability and compactness, which is consistent with amylin remaining highly flexible near physiological pH (pH 7.4) in these simulations. Amyloid dimers also have higher β-sheet content (averaging ~18–23%) than amylin (β-sheet presence at < 4%). These results reaffirm that amyloid dimers are inherently more ordered and aggregation-prone, whereas amylin adopts more flexible, transient conformations. This is backed up by the energetics data which highlights amyloid homodimers with greater average negative ΔG (-13.8) than amylin homodimers (-6.6). Stable amyloid configurations such as 3×3.10, 3×4.10, and 1×3.10, with binding free energy as low as -24 to -29 kcal/mol and a low standard deviation (~±10), combined with low Rg, strong β-structure, and reduced SASA (<5900 Å²) indicate efficient packing and energetically favourable interfacial interactions. As with previous data points there are several other complexes in less stable or favourable configurations characterized by higher energies and standard deviations, which weaken these trends and suggest towards an alternate approach. A few outlier combinations include complexes 1x3.10, 1x4.12 and 4x3.10 that have favourable energetics but minimal β-sheet presence which correlates with their high SASA values at ~7000 Å as the structure is favourable to extended conformations not aggregation-prone structures like β-sheets. Most amylin dimers are moderately stable but select complexes such as 2×2.11 (ΔG = –22.4 kcal

mol⁻¹ , RMSD = 5.7 Å, Rg = 12.1 Å) stand out for their unusually favourable energetics and compact geometries. Amylin complex 0x4.12 (ΔG = −92.9 kcal mol⁻¹) appears anomalous given its moderate structural parameters, indicating it may be anomalous. This discrepancy likely arises from an anomalous TΔS total contribution, suggesting entropic compensation or overfitting in the MM/GBSA calculation, as it was the only positive value in the energy calculations. Some amylin dimers i.e 2×3.11 (+16.7 kcal mol⁻¹) and 4×3.12 (+0.2 kcal mol⁻¹), have poor aggregation potential – exhibiting higher SASA (>6400 Å²) and low β-sheet content of expanded and weakly interacting conformations.

Both homodimers include a larger fraction of unfavourable or weakly bound cases than the heterodimers which may reflect greater steric clashes between homogeneous clusters, particularly for amylin than amyloid. The superior stability of amyloid homodimers is further evidenced by their higher number of successful 100 ns simulations compared to amylin. Among amylin clusters, clusters 1 and 3 are particularly unstable, with complexes 1x1.11, 4x3.12, 0x1.10, and 2x3.11 showing greater positive binding energy values than amyloid's cluster 3 complexes (3x3.11, 3x0.12, and 0x3.12). Despite this, amyloid dimers have more significantly low energy combinations that are very favourable than amylin, with values down to ~−26 kcal mol⁻¹ in the more favourable cases.

Amyloid homodimers such as 3x3.10 and 3x4.10, along with amylin complexes 2x2.11, 0x4.12, and 0x3.11, demonstrate greater compactness (low RMSD and Rg), higher structural stability (more negative binding free energies), and stronger association with aggregation-prone conformations (elevated β-sheet content) among their respective successful peptide pools. These tendencies appear to be highly dependent on specific inter-cluster compatibilities which warrant further exploration as done in Table 4.4.3.

Comparing them to the monomeric data reinforces the same results of the heterodimers; that dimerization largely preserves the intrinsic secondary structure tendencies of each peptide rather than inducing major conformational shifts. The small differences between monomeric and dimeric RMSD and Rg values largely stem from the increased molecular size and conformational space accessible to dimers, rather than a fundamental change in structure. These structures also have

lower SASA upon dimerization, thereby confirming burial of hydrophobic residues and binding surfaces. Yet, amyloid dimers show more pronounced solvent exclusion, while amylin dimers only partially bury their interfaces which suggests that amyloid dimerization is more cooperative in promoting β-sheet stabilization, whereas amylin dimerization remains comparatively adaptive and transient. This may also reinforce the previous experiment's point of amylin transiently pausing elongation driven by amyloid by introducing conformational heterogeneity and altering fibril morphology.

	Protonated Residues		
Amylin Combinations	**HIP18**	**HIP56**	**Predicted Charge *(lel)***
0x0.11	0.06	0.15	+6.2
0x1.10	0.04	0.02	+6.1
0x3.11	0.01	0.02	+6.0
0x4.12	0.04	0.14	+6.2
1x1.11	0.12	0.02	+6.1
1x1.12	0.17	0.02	+6.2
2x2.11	0.07	0.00	+6.1
2x3.11	0.04	0.08	+6.1
3x3.11	0.02	0.02	+6.0
3x4.12	0.02	0.09	+6.1
4x3.12	0.11	0.08	+6.2
4x4.12	0.15	0.14	+6.3

Table 4.4.3. Deprotonation values of amylin homodimer at pH 7.4.

	Protonated Residues						
Amyloid Combinations	**HIP6**	**HIP13**	**HIP14**	**HIP46**	**HIP53**	**HIP54**	**Predicted Charge (lel)**
0x0.10	0.05	0.76	0.27	0.10	0.76	0.41	-3.65
0x0.11	0.20	0.30	0.26	0.24	0.83	0.28	-3.89
0x0.12	0.06	0.89	0.57	0.14	0.87	0.36	-3.11
0x1.10	0.28	0.26	0.45	0.55	0.18	0.14	-4.14
0x3.10	0.36	0.34	0.22	0.38	0.35	0.08	-4.27
0x3.12	0.22	0.76	0.43	0.47	0.23	0.11	-3.78
0x4.10	0.12	0.94	0.19	0.45	0.15	0.49	-3.66
0x4.12	0.29	0.33	0.39	0.21	0.19	0.06	-4.53

1x0.11	0.27	0.39	0.10	0.08	0.06	0.17	-4.93
1x3.10	0.37	0.24	0.15	0.42	0.18	0.26	-4.38
1x4.12	0.56	0.19	0.10	0.36	0.26	0.41	-4.12
2x0.10	0.84	0.02	0.22	0.16	0.18	0.18	-4.4
2x0.12	0.37	0.18	0.29	0.08	0.39	0.45	-4.24
2x3.11	0.33	0.03	0.31	0.34	0.31	0.25	-4.43
3x0.11	0.42	0.23	0.45	0.17	0.29	0.14	-4.3
3x0.12	0.45	0.23	0.38	0.30	0.25	0.12	-4.27
3x3.10	0.83	0.65	0.41	0.98	0.37	0.32	-2.44
3x3.11	0.48	0.14	0.28	0.38	0.40	0.05	-4.27
3x4.10	0.68	0.46	0.29	0.34	0.00	0.11	-4.12
4x0.11	0.41	0.02	0.04	0.14	0.40	0.13	-4.86
4x3.10	0.36	0.10	0.04	0.55	0.75	0.06	-4.14

Table 4.4.4 Deprotonated values of amyloid homodimer at pH 7.4.

The titration values for both homodimers, presented in Tables 4.4.3 and 4.4.4, highlight the electrostatic basis for the previously observed conformational differences between the amylin and amyloid monomers. Amyloid homodimers exhibit moderate or partial deprotonation across a wide range of fractional values (0 – 0.92) with an average predicted charge of ~-4.1, reflecting highly variable electrostatic environments within and across clusters. This broad dispersion could be due to greater solvent exposure, as suggested by the higher SASA values relative to amylin in Table 4.4.1-2. It also reinforces the importance of geometric and environmental factors on the protonation or structure of these dimers since these homodimers have identical sequences yet provide variable protonation values across the dimer and in different complexes. Similar to the heterodimer in tables series 4.1 and 4.2, the residues HIP13 and HIP53 have on average a higher protonation range (0.76-0.94) than the HIP6 and HIP46 values. This suggests that the prior residues are likely in buried or hydrogen-bond-rich regions that stabilize their protonated states while the latter are more exposed to solvent. The differing distributions may create electrostatic gradients that sustain hydrogen-bonds network and reduces the repulsion effects the high negative charge might provide, supporting β-sheet-rich, cohesive assemblies. The more stable Aβ40 dimers… suggest that moderate histidine protonated fractions (~0.3–0.8), alongside favourable binding energies (ΔG

≈ −25 kcal mol⁻¹), can coincide with higher β-sheet alignment and compactness without excessive electrostatic strain.

In contrast, amylin homodimers show low histidine protonated fractions for His18 and His56 (0.00–0.17), consistent with predominantly neutral imidazole states at pH 7.4. With predicted charges of +6.1 ± 0.1, these dimers remain strongly cationic overall (driven mainly by Lys/Arg), which may favour flexible, helix/turn-rich assemblies rather than β-sheet-dominated interfaces. As such amylin is shown to promote compact, yet flexible conformations in table 4.4.3. They're likely stabilized via intra-chain hydrophobic shielding rather than inter-chain β-sheet stacking. The resulting assemblies remain dynamically adaptable and less prone to rigid aggregation, aligning with their higher helical content and greater conformational mobility. The most stable amylin complexes 2x2.11, 0x4.12, and 0x3.11 in Table 4.4.2, display very low protonation levels (≥0.2), indicating near-complete neutralization of imidazole sidechains. Yet they retain only moderate compactness (Rg ~14 Å, SASA ~6100 Å²), and low β-sheet content. This suggests that electrostatic neutrality alone is insufficient to maintain tertiary compactness. Instead, amylin's stability may arise from hydrophobic side-chain interactions and secondary-structure adaptability as highlighted by the higher helical content and reduced β-structure.

4.3.1.5 Expanding Simulations to 600 ns

The dimers selected for extended simulation represent the most stable configurations from the earlier screening. The systems that remained associated through 600 ns are summarized in Table 4.20. The comparative dynamics reveal that, over time, amylin homodimers evolve toward a more compact and conformationally restricted ensemble (RMSD = 6.7 ± 1.0 Å; Rg = 12.52 ± 0.5 Å) than their amyloid counterparts. This structural tightening likely reflects enhanced intramolecular hydrogen bonding and hydrophobic collapse, consistent with amylin's intrinsically disordered yet solvent-adaptive character.

For amyloid homodimers, which in the earlier 100 ns screening showed weaker association energies (ΔG ≈ −11.6 kcal mol⁻¹ vs. −13.8 kcal mol⁻¹ for amylin), a stronger binding signal is observed after extended sampling, reaching –35.0 ± 8.9 kcal mol⁻¹ against –18.5 ± 9.9 kcal mol⁻¹ for amylin. However, this shift is accompanied by a decrease in both β-sheets and helical content and an increase in

non-specific packing with turns/bends and coils which is a progression away from the fibril-like, β-enriched nucleus formation. This indicates that this energetic stabilization is not due to increased structural order but may instead reflect side-chain rearrangement and improved nonbonded complementarity (e.g., van der Waals packing and electrostatics). Despite a lack of organized secondary structure formation, the side chains of these dimers still found a way to pack together efficiently, either by minimizing steric clashes, maximizing van der Waals contacts, or stabilizing the interface through shape and charge complementarity. The lower standard deviations across the 600 ns trajectories – after treating the first 100 ns as equilibration thanks to RMSD plateau and Rg block analysis – suggest reduced conformational noise and dampened fluctuations/ limited set of contact patterns. This is consistent with both systems settling into a metastable state that is stable against small perturbations. In this regime, the interfaces remain persistent but still fluctuate around a limited set of contact patterns. However, this does not necessarily imply the complexes have reached the globally most thermodynamically stable conformation.

A persistent trend is that amyloid homodimers retain greater secondary-structure order (higher β-sheet and α-helical content), whereas amylin homodimers maintain lower SASA values, consistent with compact yet flexible states. This supports earlier observations that amylin's structural stability is caused due to greater hydrophobic shielding and intra-chain compaction contributions than from inter-strand β-networking.

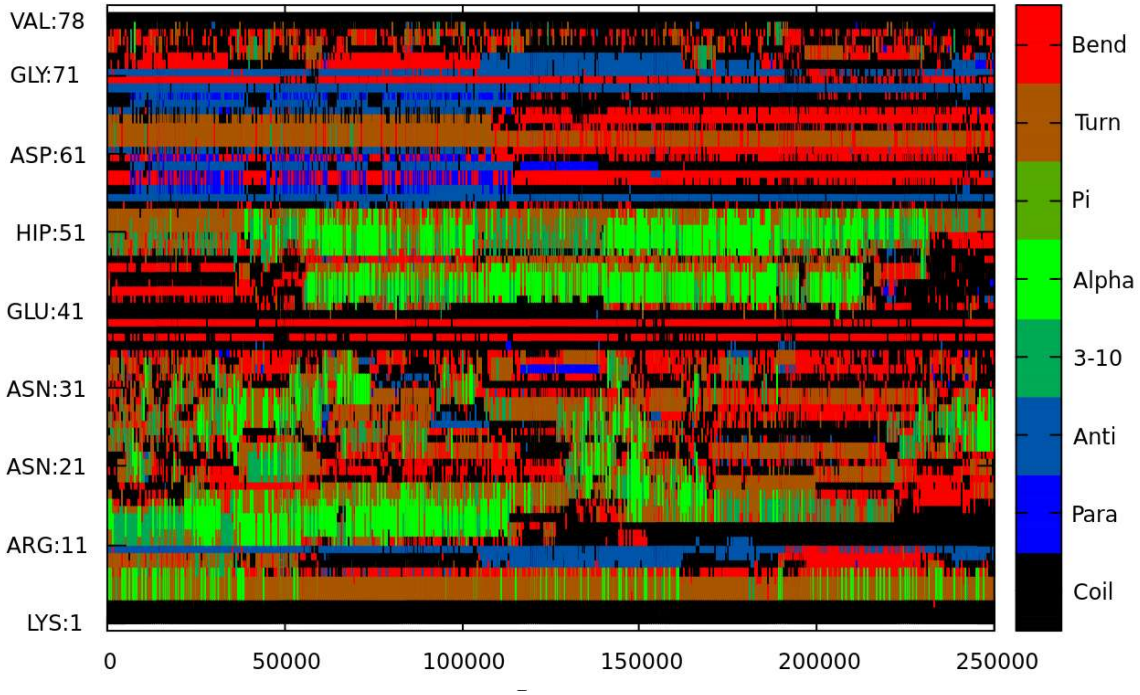

Figure 4.5.2 Evolution of secondary structures over the span of 500 ns post-equilibration in pH 7.4.

The heterodimers, which initially appeared with fewer differences also diverge significantly after extended sampling. The amylin × Aβ40 heterodimers show, on average, stronger binding energies and tighter packing than the Aβ40 × amylin orientation, compared to the Aβ40 x amylin orientation, which are slightly more flexible and variable in stability. This asymmetry may be due to orientation-dependent destabilization effects, suggesting that the two docking orientations optimize steric and electrostatic complementarity differently. When simulated for an extended period, the organized structures like β-sheet and helices relax into bends, turns or coil conformations indicating the short temporal window the dimers exist in an aggregation-competent state, capable of assembling into more complex oligomers as presented by amylin-led heterodimer 2x2.12 in Figure 4.5.1. Most alpha helices and parallel β-sheets in Aβ40 Arg11-Asn21 segment and the corresponding interface region (His51 – Gly71) region deteriorate into bends and coils after 200 ns. The emergence of α-helical propensity at the Aβ40 N-terminus is consistent with interfacial contacts with amylin stabilizing local structure, even as β-rich motifs relax elsewhere In conclusion, prolonged simulation may lead to a loss of ordered secondary structures (helices and β-sheets), despite improved energetic stability.

The stability likely arises from side-chain rearrangement rather than continued fibril-oriented organization. A schematic representation of the overall dimer formation, showcasing exemplar rearrangements is highlighted in Figure 4.5.3.

Combination	*RMSD (Å)*	*Rg (Å)*	*β-Sheet (%)*	*Helices (%)*	*Δ G (kcal mol⁻¹)*	*SASA (Å²)*
Amxam 2x2.11	6.7 ± 1.0	12.52 ± 0.5	4	8	-18.45 ± 9.9	5143 ± 290
Abxab 3x3.10	10.3 ± 2.0	13.74 ± 1.0	6	26	-35.0 ± 8.9	6058 ± 397
Amxab 0x3.10	9.0 ± 1.3	12.9 ± 0.3	16	13	-28.5 ± 10.1	5118 ± 217
Amxab 2x2.12	12.6 ± 2.0	14.9 ± 1.5	9	15	-28.0 ± 14.0	5997 ± 418
Abxam 0x2.11	13.4 ± 2.7	15 ± 1.6	13	14	-8.2 ± 6.4	6083 ± 364
Abxam 1x3.12	12.6 ± 2.3	15.12 ± 1.9	8	16	-24.0 ± 16.1	5737 ± 281

Table 4.20 Statistical results of RMSD (Å), Rg (Å), secondary structure content (%), solvent accessible surface area and binding free energy for homo- and heterodimers at pH 7.4 simulated for 600 ns.

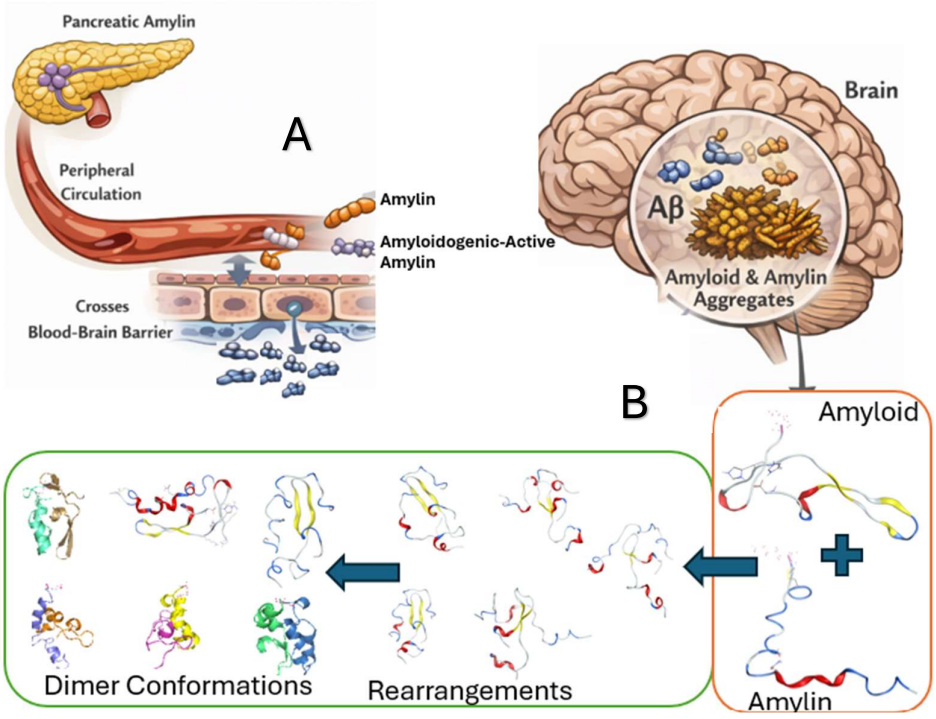

Figure 4.5.3 An Overview of the Aβ-amylin aggregation pathway: **A)** Amylin's transport towards an already present Amyloid in the brain via crossing of the Blood Brain Barrier. **B)**

Amyloid and Amylin's binding rearrangements during first nucleation steps. The resulting various dimers are representative of the many different conformational wells that the peptides can occupy.

4.3.2 Comparing Heterodimer and Homodimer Simulations at pH 6, 7, and 8

	pH 6			pH 7			pH 8		
amxam	10	11	12	10	11	12	10	11	12
0X0									
1X1									
2X2									
abxam									
0x0									
1x1									
2x2									
abxab									
0x0									
1x1									
2x2									
amxab									
0x0									
1x1									
2x2									

Table 4.6.1 Simulation results of hetero- and homo- dimers in pH 6 environment after 100ns. Red indicates failures to remain together. Green shows dimers that remained bonded.

Previous experiments at pH 7.4 explored over 120 dimeric combinations, producing broad but weakly correlated stability trends due to the wide range of starting conformations and limited trajectory length. Accordingly, the pH 6–8 experiments use a narrower sampling scope (0x0, 1x1, and 2x2) from both homo- and heterodimer systems as noted in Table 4.6.1. A narrower selection targets the most statistically relevant and energetically favourable conformations, facilitating controlled comparisons, and allows for more efficient long trajectory protonation–conformation coupling analysis for the more computationally expensive CpHMD. The smaller, triplicate-based approach would also reduce variability arising from structural heterogeneity and facilitate direct assessment of how pH-dependent protonation influences interfacial stability over extended simulation times.

Amylin homodimer simulations performed very poorly in acidic conditions (pH 6), resulting in complete structural dissociation by the 100 ns mark (0% success rate), consistent with increased protonation at pH 6 amplifying electrostatic repulsion

between the positively charged chains and destabilizing the positively charged amylin monomers. Neutral conditions, pH 7, sees a modest improvement with a 34% success rate at 100 ns, though none of these complexes survived beyond 500 ns, indicating only transient stability near physiological pH. Even at pH 8, where the initial 100 ns success rate rose to 56%, all amylin dimers eventually disassociated during extended 500 ns runs. This pattern demonstrates that while deprotonation initially reduces repulsive interactions, the lack of complementary physical and chemical features at the interface ultimately prevents long-term dimer maintenance.

Of the 9 MD simulations of amyloid β-40 homodimers in each pH, pH 6 saw a higher portion of dimers remaining bound (56%) at 100 ns to pH 7's success rate (45%), and both saw success after 500 ns as well. This suggests that amyloid dimers are most stable under mildly acidic to neutral conditions, where partial histidine protonation supports cohesive hydrogen-bonding and limits solvent disruption. However, stability sharply declined at pH 8; the only successful combination at 100 ns simulation broke early-on during the further 500 ns simulation. This can be attributed to the near-complete histidine deprotonation, which disrupts inter-chain electrostatic complementarity and is consistent with reduced stabilization of β-associated hydrogen bonding patterns. Moreover, fully deprotonated amyloid monomers carry an approximate net charge of –3 under these conditions, meaning that amyloid homodimers experience the greatest electrostatic repulsions which further destabilizes inter-peptide packing and prevents sustained aggregation. Collectively, these results indicate an inverse relationship where amyloid dimers are most stable at lower or slightly acidic to neutral conditions, where partial protonation would enhance hydrogen-bond cooperativity and minimizes solvent-driven or charge-based disruption.

For amyloid–Amylin heterodimers, the success rates or stability for simulations at 100 ns progressively improved with increasing pH. Dimers in pH 6 saw a 22.5% success rate for the 100 ns benchmark, the lowest compared to pH 7's 33.5 % and pH 8's 44.5%, with the top-performing clusters (e.g., 0x0.10 at pH 6 and pH 7, and 2x2.10 at pH 8) maintaining stability up to 600 ns. These results highlight the greater resilience of heterodimers compared to either homodimer type. In higher-pH environments, heterodimer formation likely mitigates the electrostatic repulsion that destabilizes amylin by pairing it with a more negatively charged amyloid subunit.

Amylin’s positive charge and inherent destabilizing repulsions are partially neutralized by the amyloid chain producing a more even electrostatically favourable landscape at the interface. In addition, the alignment of their hydrophobic regions supports closer packing and stronger hydrogen-bond networks, leading to complexes that are denser, more cooperative, and better able to tolerate shifts in protonation.

Interestingly, this stability advantage is asymmetrical: Aβ40 × amylin (AbxAm) heterodimers consistently outperform the reciprocal amylin × Aβ40 (AmxAb) orientation, with the former’s 12 successful simulations against the latter’s 5. This preference points to a functional polarity in which amyloid acts as the structural receptor, its β-sheet framework forming a firm docking surface, while amylin, rich in helical segments, serves as the more flexible ligand. Such a relationship fits well with earlier reports that helically biased peptides generally produce less ordered interfaces when they initiate binding, whereas β-sheet-dominated partners tend to create flatter, more cohesive contact regions that stabilize the overall complex (17–21).

pH	Combinations	RMSD (Å)	Rg (Å)	β-Sheet (%)	Helices (%)	Δ G (kcal mol⁻¹)	SASA (Å²)
pH 6	*Abxab 2x2.11*	8.1 ± 1.0	14.2 ± 0.7	18	20	-11.3 ± 5.5	5963 ± 278
	Abxam 0x0.10	10.4 ± 4.3	14.9 ± 2.0	6	21	-11.4 ± 6.7	5891 ± 588
pH 7	*Abxam 0x0.10*	10.9 ± 2.0	14.6 ± 1.9	17	12	-9.5 ± 7.2	5928 ± 409
	Abxab 2x2.10	5.8 ± 0.8	14.2 ± 0.3	20	16	-42.8 ± 10.7	6049 ± 216
	Amxab 0x0.10	12.4 ± 1.9	15.6 ± 2.2	11	29	-22.6 ± 12.8	6203 ± 508
pH 8	*Abxam 0x0.10*	10.7 ± 2.6	14.6 ± 2.4	3	28	-35.0 ± 7.6	5906 ± 568
	Amxab 2x2.10	12.9 ± 1.6	14.2 ± 1.9	5	17	-22.1 ± 6.1	5921 ± 574

Table 4.6.2 Statistical results of RMSD (Å), Rg (Å), secondary structure content (%), solvent accessible surface area and Gibbs Free energy (binding free energy) for selected homo- and heterodimers of amylin x amyloid at pH 6, 7, and 8.

All dimers compared together, as represented by Table 4.6.1, indicate a preference for the near neutral environment. The systems in pH 6 display a slightly flexible heterodimer conformation with 8-10 Å RMSD and ~14.5 Å Rg values. These flexible structures are consistent with weaker binding ($\Delta G \approx -11$ kcal mol^{-1}) and modest β-sheet content (6–18%). This may reflect higher histidine protonated fractions at pH 6 (Table 4.6.3), which can increase electrostatic repulsion, reduce interfacial hydrogen-bond stabilization, and diminish overall structural compactness, a hallmark of systems optimized for transient interactions (22,23).

Structural stability is much more variable in pH 7 environments, with homodimer 2x2.10 complex maintaining a more rigid and stable structure with RMSD, Rg, ΔG values at 5.8 Å, 14 Å and –42.8 kcal mol^{-1} , respectively, while the heterodimers are

less so. They maintain higher RMSD and Rg values with less β-sheets than the amyloid beta homodimer, consistent with amylin's intrinsic conformational flexibility and weaker β-aggregation propensity noted earlier. At this intermediate pH, protonation averages differ markedly between complex types, heterodimers exhibit lower histidine protonation (~0.26) than amyloid homodimers (~0.46), indicating that partial deprotonation improves charge balance at the interface and stabilizes neutral electrostatic environments. This selective charge moderation likely contributes to the enhanced energetic stability observed at the near-physiological pH.

Amylin x amyloid complex 0x0.10 illustrates a two-phase trajectory in Figure 4.6A an initial rise in RMSD up to ~20 Å within the first 100 ns, followed by a sharp fall to 13-17 Å that it maintains for the rest of the 600 ns simulation. This behaviour consists with a flexible but stable structure, as demonstrated by its high SASA values at ~6100 *Å²,* and the relatively high RMSD plateau suggests partial unfolding or rearrangement at the interface, perhaps driven by uneven partial protonation of histidine residues (0.11–0.76, Table 4.6.2) and a positively predicted net charge (+1.04). Despite this, the RMSD fluctuations do stabilize toward the final 300 ns, perhaps the system settles into a metastable conformation as with the extended pH 7.4 simulations. Orientation also plays a significant role: amyloid homodimers consistently exhibit more balanced deprotonation and greater negative charge (–3.78) than their Aβ40 x amylin counterparts, which show asymmetrical charge distributions that destabilize interface geometry. A similar amylin-receptor heterodimer in pH 8 environment shows the peptide undergoing more fluctuations within a 10-15 Å range with 2 or 3 Å deviations for 100 ns at a time after it reached a plateau in Figure 4.6B, reflecting moderate but persistent stability. Under basic conditions, the successful heterodimers have lower β-sheet content (3–5%) and greater helical character (17–28%), combined with a moderately negative binding energy (-35.0 – -22.1 kcal mol^{-1}), and lower still SASA values (~5900) this supports the interpretation that mostly deprotonated (0.0–0.2) systems lose charge-mediated cohesion but compensate through compact hydrophobic and π-stacking rearrangements, which maintain compactness but hinder further β-sheet aggregation.

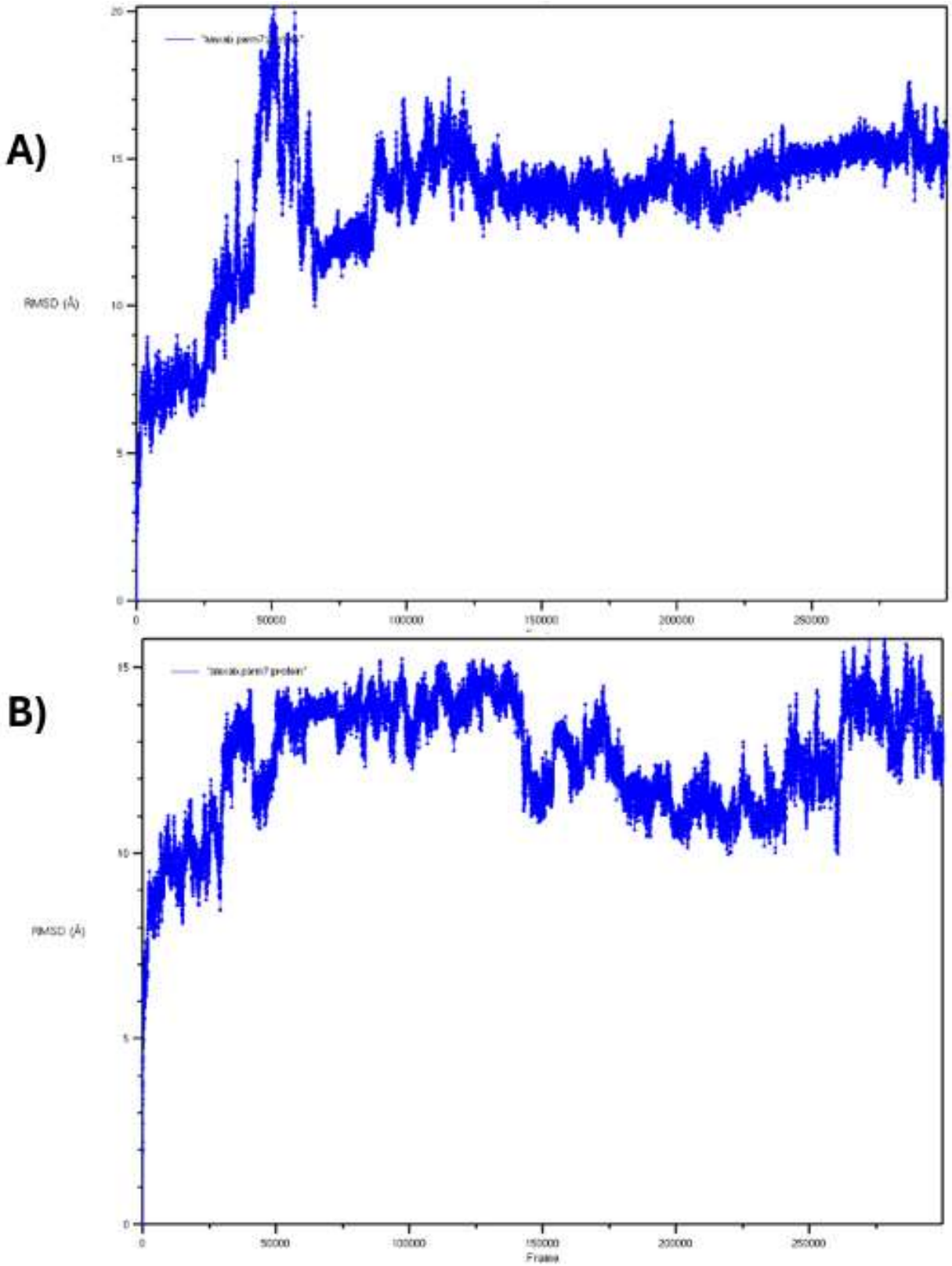

Figure 4.6 RMSD graph of amylin x Aβ40 heterodimer combination **A.** 0x0.10 in pH 7 and **B.** 2x2.10 in pH 8 simulated for 600 ns.

pH	Combination	HIP 6	HIP 13	HIP 14	HIP 18	HIP 44	HIP 46	HIP 51	HIP 52	HIP 53	HIP 54	HIP 58	Predicted Charge (lel)
6	**Abxam 0x0.10**	0.71	0.77	0.84								0.91	3.23
	Abxab 1x1.10	0.95	0.88	0.80			0.89			0.83	0.89		-0.75
7	**Abxam 0x0.10**	0.58	0.21	0.15								0.11	1.04
	Abxab 2x2.10	0.76	0.47	0.46			0.22			0.27	0.55		-3.78
	Amxab 0x0.10				0.28	0.51		0.35	0.28				1.42
8	**Abxam 0x0.10**	0.02	0.01	0.01								0.00	0.04
	Amxab 2x2.10				0.02	0.19		0.02	0.00				0.20

Table 4.6.3 Protonation dataset and predicted charge of successful dimers in pH 6, 7 and 8. Blank entries indicate residues are not present in that peptide/complex.

The data of dimers in Table 4.6.2-.3 being linked to the monomeric data in Table 4.6.4 reinforce the previously established trends; structural dynamics of monomers influence the early conformation of their dimers. Amyloid monomers possess higher intrinsic β-sheet content (5–10%) and smaller Rg (11–12 Å) than amylin (β-sheets <3%, Rg ~13 Å), predisposing amyloid-first dimers to greater compactness and order. This inheritance effect may explain why, across both RMSD plots and tabulated data, amyloid-dominant heterodimers (AbxAm) appear more structurally stable than amylin-dominant ones (AmxAb). The differences are largely contained to how compact or flexible the dimers are compared to their constituents. As referenced above, the sum of monomer's SASA value (7200 Å²) is far larger than what structure the dimers adopt after 600 ns MD simulation. The heterodimers cover a broad range of exposed structures, with most remaining consistently compact, SASA at ~5950 Å² ± 203 average, and some like the heterodimer (Amxab 0x0.10) at pH 7 exhibiting the

most flexible and exposed conformation (Rg = 15.6, SASA = ~6203 Å²), that is also very stable (MM/GBSA ΔG = -22.6 kcal mol⁻¹), suggesting entrapment into a low energy well. The homodimers are also consistent with the energy well trapped conformation with a very flexible and loose structure (Rg = 14.2, SASA = 6029 Å²) that also is the most stable at pH 7 (MM/GBSA ΔG = -42.8 kcal mol⁻¹), correlating with it properties as the least flexible and displaced dimer. Though most other conformations display moderately favourable energetics (–10 to –35 kcal mol⁻¹), with consistently compact structures (Rg = <10), reflecting stable yet dynamic interfacial interactions.

pH	Combination	*RMSD (Å)*	*Rg (Å)*	*B- Sheet (%)*	*Helices (%)*	*SASA (Å²)*
6	**Amyloid - 40**	8.9 ± 1.5	12.0 ± 1.7	5	23	3700 ± 310
	Amylin	9.3 ± 1.6	12.9 ± 2.2	0.8	24	3571 ± 287
7	**Amyloid - 40**	9.1 ± 2.2	11.6 ± 1.7	10	22	3625 ± 277
	Amylin	9 ± 1.5	13.2 ± 2.3	1	23	3586 ± 295
8	**Amyloid - 40**	8.7 ± 2.1	11.4 ± 1.6	9	17	3600 ± 303
	Amylin	8.5 ± 1.4	13.1 ± 2.2	3	20	3556 ± 285

Table 4.6.4 Simulation results of amyloid and amylin monomer's RMSD, Rg, SASA, and secondary structures data in pH 6, 7 and 8 environments.

In conclusion, the tabulated data indicates that neutral pH yields the most stable conformations due to balanced charge states that favour β-sheet alignment, with higher and lower pH conditions promoting more flexible structures where, in theory, hydrophobic interactions and interfacial repulsions would be competing for and against stability. As expected from simulations not reproduced and validated in triplicates comparisons, extremely stable structures appear to have extended conformations, a combination that is consistent with being trapped in energy wells. Expanding this investigation to trimers would allow evaluation of whether the stabilizing trends observed in dimers persist as structural complexity increases. The trimer stage marks the beginning of cooperative aggregation, where molecular interfaces and sequence heterogeneity begin influencing overall conformational stability. Considering Hureau's observations that 25–50% amylin content modifies Aβ

aggregation dynamics in Figure 4.1, conducting trimer experiments with a 33% amylin ratio provides a controlled model to explore how mixed interfaces might alter early oligomer formation and disrupt aggregation routes linked to AD.

4.3.3 Extending Established Testing Parameters to Trimer Simulations

A)

Abxam 1x3.12	10	11	12
ab0			
ab1			
ab2			
Amxab 0x3.10			
ab0			
ab1			
ab2			
Abxab 3x3.10			
am0			
am1			
am2			

B)

Abxab 2x2.10	10	11	12
am0			
am1			
am2			
Abxam 0x0.10			
ab0			
ab1			
ab2			
Amxab 0x0.10			
ab0			
ab1			
ab2			

Table 4.7.1 Simulation results of trimers with combinations of 2 amyloid peptides and 1 amylin peptide in **A)** pH 7.4 and **B)** pH 7 environment after 100ns. Red indicates trimers that failed to remain together while green is reserved for those trimers that successfully remained together.

Combination	*RMSD (Å)*	*Rg (Å)*	*B- Sheet (%)*	*Helices (%)*	*SASA (Å²)*
Abxamxab0.11	8.7 ± 0.9	15.1 ± 0.6	13	8	7828 ± 379
Amxabxab0.11	7.7 ± 1.5	16.0 ± 0.8	23	15	7695 ± 455
Abxabxam1.10	11.4 ± 3.0	17.2 ± 1.7	5	23	8293 ± 622

Table 4.7.2 Statistical results of RMSD (Å), Rg (Å), secondary structure content (%), solvent accessible surface area for heterotrimers at pH 7.4.

Table 4.7.1A and Table 4.7.1B suggest amyloid-led trimers are more successful in docking and aggregation dynamics; however, when the structural trends established in earlier experiments are considered (Tables 4.6.2–4.6.4), the amylin-led simulations appear to form the most conformationally preferred assemblies. At pH 7.4, the trimeric systems highlight greater stability for amylin-led trimers, with the amylin × amyloid × amyloid complex (Am×Ab×Ab_0.11) exhibiting a compact structure (SASA = 7695 ± 455 Å²; Rg = 16.0 ± 0.8 Å). Its combination of high β-sheet content (23%) with moderate helicity (15%), alongside low RMSD (7.7 ± 1.5 Å), is consistent with a semi-ordered yet still adaptable complex that maintains structural integrity while permitting limited conformational rearrangement. The mean histidine protonated fraction (~0.21 across the listed His sites) and corresponding net charge (–1.4) are also consistent with reduced interchain electrostatic repulsion, which can facilitate tighter hydrophobic packing and π–π stacking at the interface and thereby support β-sheet stabilization. However, it is important to note that apparent “stability” in a single long trajectory can also reflect kinetic trapping in a favourable local energy well rather than a uniquely preferred binding mode; therefore, this interpretation would be strengthened by independent replicate simulations showing that the same compact, β-enriched interface repeatedly emerges from different initial velocities or starting poses. Finally, the outlying HIP44 protonation fraction (0.95) may reflect a site-specific microenvironment, such as localized solvent exposure or stabilization by nearby negatively charged residues (Asp/Glu), which can shift histidine protonation even within an otherwise more deprotonated complex.

In contrast, Ab×Am×Ab0.11 demonstrated moderate compactness (Rg = 15.1 ± 0.6 Å; SASA = 7828 ± 379 Å²), characterized by uneven protonation (0-0.45) that produced local electrostatic asymmetry and disrupted tertiary stabilization (β-sheets = 13% and helices = 8%) Although it maintained structural integrity throughout the simulation, its relatively higher SASA and less negative ΔG values indicate weaker interfacial cohesion, consistent with the hypothesis that uneven histidine protonation compromises charge complementarity, leading to localized destabilization. The least stable configuration, Ab×Ab×Am1.10, exhibited the highest solvent exposure (SASA = 8293 ± 622 Å²), largest Rg (17.2 ± 1.7 Å), and minimal β-sheet formation (5%) and pronounced helicity (23%). Here, terminal amylin placement introduced excessive

flexibility and electrostatic repulsion from multiple protonated histidine residues (0.01-0.76), leading to unstable tertiary packing and poor interfacial cohesion.

	Protonated Residues																
Combinations	***HIP 6***	***HIP 13***	***HIP 14***	***HIP 18***	***HIP 44***	***HIP 46***	***HIP 51***	***HIP 52***	***HIP 53***	***HIP 54***	***HIP 58***	***HIP 84***	***HIP 86***	***HIP 91***	***HIP 92***	***HIP 98***	**Predicted Charge (Iel)**
Abxamxab0.11	0	0	0.45								0.01	0.07		0.12	0.05		-2.3
Amxabxab0.11				0	0.95		0.11	0.22						0.21	0.13		-1.4
Abxabxam1.10	0.53	0.02	0.42			0.10			0.76	0.01						0.07	-1.1

Table 4.7.3 Protonated values with predicted charge of trimers at pH 7.4

Combination	***RMSD (Å)***	***Rg (Å)***	***B- Sheet (%)***	***Helices (%)***	***SASA (Å²)***
Abxabxam 0x0.10	8.2 ± 1.6	16.3 ± 1.2	14	21	8266 ± 386
Abxamxab 0x0.10	8.5 ± 2.1	16.4 ± 0.8	17	16	8441 ± 469
Amxabxab 0x0.10	10.0 ± 1.4	15.0 ± 1.0	16	20	7709 ± 483

Table 4.7.4. Statistical results of RMSD (Å), Rg (Å), secondary structure content (%), solvent accessible surface area for heterotrimers at pH 7.

	Protonated Residues															
Combination	**HIP 6**	**HIP 13**	**HIP 14**	**HIP 18**	**HIP 44**	**HIP 46**	**HIP 51**	**HIP 52**	**HIP 53**	**HIP 54**	**HIP 58**	**HIP 84**	**HIP 91**	**HIP 92**	**HIP 58**	**Predicted Charge (Iel)**
Abxabxam 0x0.10	0.71	0.41	0.38			0.29			0.31	0.44					0.29	-0.2
Abxamxab 0x0.10	0.48	0.01	0.39								0.03	0.63	0.53	0.28		-0.7
Amxabxab 0x0.10				0.17	0.66		0.30	0.04				0.42	0.61	0.13		–0.7

Table 4.7.5 Protonation data and predicted charge of histidine residues in successful trimers for pH 7.

At pH 7, the trimer simulations once again revealed a pronounced orientation dependence in structural stability, with trimers produced from amylin x amyloid

dimers outperforming amyloid-led ones despite having higher overall failure rate (five failed trajectories compared to four in the other groups) as shown in Table 4.6.1B, consistent with the charge imbalance and interfacial incompatibility previously observed in amylin-led dimers under near-neutral conditions. Among the successful constructs, Am×Ab×Ab_0.10 emerged as the most stable and compact trimer, exhibiting a low solvent exposure (SASA = 7709 ± 483 Å²), and an Rg value of 15 ± 1 Å. Its balanced secondary structure composition (β-sheets ≈ 16%, α-helices ≈ 20%), moderate RMSD (~10 Å) and low protonation levels (0.1–0.4) yielding a somewhat negative predicted charge (≈ −0.2 to −0.7, depending on the construct) point to a semi-flexible yet cohesive architecture perhaps stabilized through hydrophobic and π–π stacking interactions than extensive charge pairing, mirroring the stabilization mechanisms inferred for amylin-dominated dimers.

In contrast, Abxabxam and Abxamxab trimers exhibit slightly higher SASA values (8266 ± 386 Å² and 8441 ± 469 Å²) and a more extended structure (Rg = 16.3± 1.2 Å and –16.4 ± 0.8 Å, respectively), implying looser packing and greater solvent exposure. These two systems also showed more uneven, heterogeneous histidine protonation profiles; Ab×Ab×Am shows clusters of strongly protonated sites (HIP6 = 0.71, HIP13/14 ≈ 0.4) alongside more weakly protonated positions (HIP51/54/58 ≈ 0.29–0.44; predicted charge –0.2), while Ab×Am×Ab and Am×Ab×Ab span almost fully deprotonated to strongly protonated states (HIP13 ≈ 0.01; HIP46/92 ≈ 0.6–0.66; predicted charge ≈ –0.7). The data suggests electrostatic asymmetry across the trimer interfaces that likely frustrates optimal hydrogen-bonding and salt-bridge pairing, in line with the observed poor tertiary packing and higher RMSD and Rg values (~8.4 Å and ~16.4 Å, respectively).

4.4 Conclusion

CpHMD exploration of Aβ40 and amylin, homomeric and heteromeric assemblies across near-physiological pH (6–8) conditions suggests that early aggregation behaviour arises from a finely balanced interplay of electrostatics, protonation, and structural complementarity rather than sequence homology alone. Overall, heterodimers show the highest success rate for dimer formation, although they are not, on average, as structurally compact and stable as amyloid homodimers, which consistently display the most favourable energetic and structural parameters. When

Aβ40 served as the receptor and amylin as the ligand, the heterodimers were, on average, more successful at remaining associated, whereas the reciprocal orientation sometimes produced tighter packing but with reduced β-sheet content. Overall, the two docking directions appear to favour different trade-offs between compactness, persistence, and secondary-structure organization.

As identified in previous chapters using shorter peptide counterparts, Aβ's bias toward β-sheet formation—localized primarily to residues 17–32 within the hydrophobic core—confers greater conformational order and thermodynamic stability to its dimers and trimers, enabling cohesive, aggregation-prone conformations under near-neutral conditions (pH 7.4). By contrast, amylin dimers remain structurally flexible/extended, with broader RMSD and Rg ranges, higher solvent exposure, and a strong preference for helical or coil states. In heterodimers, this conformational adaptability supports a transient stabilizing or distorting influence on β-structured Aβ40 interfaces, consistent with amylin's experimentally observed role as both a co-aggregate and modulator of amyloid fibril growth. Reciprocal comparisons indicate a directional preference: when Aβ40 acts as receptor and amylin as ligand, more "successful" dimers are formed (i.e., complexes that do not dissociate during simulation) and, on average, more organized conformations emerge with higher combined strand and helix content. The reciprocal orientation yields complexes that are often more compact and stable, but typically with reduced β-sheet content, suggesting that orientation influences the efficiency of interfacial hydrogen bonding and charge pairing. This directional preference persists in trimeric systems, indicating that binding polarity is likely an intrinsic feature of the co-aggregation mechanism rather than solely an artefact of initial docking geometry.

Extending simulations to 600 ns further showed that energetic stabilization over time appears primarily associated with side-chain rearrangement and nonbonded packing, rather than progressive β-enrichment. Amyloid homodimers reached lower-fluctuation regimes consistent with improved van der Waals packing and hydrophobic optimization, while interpretations of amylin homodimer behaviour were limited by the implicit-solvent framework; the single explicit-solvent reference run suggested behaviour closer to the heterodimer class, with comparatively lower stability and greater flexibility than implied by the implicit model alone. Though an acknowledgement to the risks from this method is needed here; the long simulations

may still be trapped in energy wells since the structure is not validated for reproducibility *via* triplicates like Aβ16 in chapter 3. Such is evident with the most stable structure of pH 7 hetero- homodimer assemblies, which despite occupying a low-energy well exist in very extended conformations. Together, these results suggest that mixed Aβ–amylin assemblies form semi-ordered intermediates can persist long enough to seed further oligomerization. The pH comparison is also consistent with this conclusion: amyloid dimers achieved highest stability under mildly acidic to neutral conditions (pH 6–7), where partial histidine protonation reduced solvent disruption and strengthened hydrogen-bond cooperativity, consistent with more favourable binding free energies (< −20 kcal mol^{-1}). Heterodimers, by contrast, showed a gradual increase in stability from pH 6 to 8, consistent with cross-charge compensation in which amylin's positive character offsets amyloid's negative potential and produces a more balanced interfacial electrostatic landscape. This same mechanism plausibly explains why heterodimers tolerate pH shifts better and retain association longer than either homodimer system.

Protonation analysis identifies histidines as key electrostatic modulators of stability. Moderate protonation states produce the most stable and compact structures, plausibly by enabling salt-bridge and cation–π interactions that reduce electrostatic strain while maintaining hydrogen-bond cooperativity. By contrast, near-complete protonation or near-complete deprotonation disrupts this balance, increasing flexibility and solvent exposure. The wide spread of protonation values (0.00–0.99) observed even within nominally similar complexes further indicates that local geometry and microenvironment can influence titration behaviour as strongly as residue identity alone. Accordingly, pH 7 systems most frequently yielded compact and thermodynamically favourable conformations, whereas pH 6 and 8 produced more dynamic, less ordered ensembles. While residue-level titration data provides mechanistic insight into charge-state fluctuations, global descriptors such as RMSD, Rg, SASA, and ΔG remain the most reliable indicators of overall assembly stability in these simulations.

Trimeric assemblies, representing the next stage of oligomerization, extend these trends. Amylin-led trimers (Am×Ab×Ab) produced the most compact and structurally balanced configurations at pH 7–7.4 (Rg ≈ 15–16 Å; β-sheet ≈ 23%), accompanied by moderate histidine deprotonation (~0.2) and a moderately negative net charge

(~−1.4), which is expected given the contribution of deprotonated Asp/Glu residues on Aβ at neutral pH. Notably, unlike amylin-led heterodimers, these trimers showed comparable β-strand and helical content, consistent with a mixed, semi-ordered interface rather than a purely β-core architecture. By contrast, amyloid-led trimers were generally larger and more solvent-exposed (SASA ≈ 8200 Å²) and displayed more irregular protonation, consistent with increased electrostatic asymmetry and weaker tertiary packing. Overall, the trimer data support a cooperative model in which amylin promotes compact association while maintaining conformational heterogeneity, potentially facilitating further amyloid recruitment and subsequent β-core development rather than locking the assembly immediately into an amyloid-homomer-like, β-rich state. This interpretation aligns with experimental observations that intermediate amylin fractions (25–50%) alter amyloid aggregation kinetics and fibril morphology.

A key limitation of the long (600 ns) simulations is that, while they better map the conformational space accessible to a given starting pose and allow slow interfacial rearrangements to emerge, they do not by themselves demonstrate reproducibility. A single long trajectory can still reflect residence in a “lucky” energy basin determined by the initial docking orientation and velocity assignment. Therefore, stronger validation would come from a Chapter 3–style replicate design in which multiple independent simulations (with randomized initial velocities and/or alternative starting interfaces) converge on the same ensemble-level trends in stability, protonation behaviour, and secondary-structure balance.

Together, these findings establish a coherent mechanistic picture of early Aβ40–amylin co-aggregation: (1) stability is governed by partial histidine protonation that balances interfacial charge without eliminating adaptive flexibility; (2) heterotypic assembly provides greater thermodynamic and geometric complementarity than homotypic aggregation, generating intermediates conducive to further oligomerization; and (3) aggregation efficiency depends not on rigid fibril-like ordering at the earliest stage, but on adaptable, semi-ordered β–α hybrid architectures capable of dynamic rearrangement under changing electrostatic conditions. Overall, the results support a model in which Aβ40–amylin cross-seeding is cooperative but self-limiting: heterodimer and trimer formation can enhance early association and nucleation while moderating runaway fibril propagation through

maintained conformational heterogeneity. Such assemblies may represent physiologically relevant intermediates that contribute to the molecular intersection of Alzheimer's disease and Type II diabetes.

4.5 References

1. Tarus B, Straub JE, Thirumalai D. Dynamics of Asp23-Lys28 salt-bridge formation in Abeta10-35 monomers. J Am Chem Soc. 2006 Dec 20;128(50):16159–68.

2. Wu C, Bowers MT, Shea JE. Molecular Structures of Quiescently Grown and Brain-Derived Polymorphic Fibrils of the Alzheimer amyloid Aβ9-40 Peptide: A Comparison to Agitated Fibrils. PLOS Comput Biol. 2010 Mar 5;6(3):e1000693.

3. Wang Q *et al.* Computational Investigation of Coaggregation and Cross-Seeding between Aβ and human amylin Underpinning the Cross-Talk in Alzheimer's Disease and Type 2 Diabetes. J Chem Inf Model. 2021;61:5341–55.

4. Wang X, Wu X, Brooks BR, Wang J. Accurate Free Energy Calculation via Multiscale Simulations Driven by Hybrid Machine Learning and Molecular Mechanics Potentials. J Chem Theory Comput. 2025 July 22;21(14):6979–87.

5. Singh A *et al.* Lid opening and conformational stability of T1 Lipase is mediated by increasing chain length polar solvents. Proteins Struct Funct Bioinforma. 2020;88:1401–12.

6. Decker Y, Németh E, Schomburg R, Chemla A, Fülöp L, Menger MD, *et al.* Decreased pH in the aging brain and Alzheimer's disease. Neurobiol Aging. 2021 May 1;101:40–9.

7. Zheng L, Cedazo-Minguez A, Hallbeck M, Jerhammar F, Marcusson J, Terman A. Intracellular distribution of amyloid beta peptide and its relationship to the lysosomal system. Transl Neurodegener. 2012 Sept 26;1(1):19.

8. Jha S, Snell JM, Sheftic SR, Patil SM, Daniels SB, Kolling FW, *et al.* pH dependence of amylin fibrillization. Biochemistry. 2014 Jan 21;53(2):300–10.

9. Genheden S, Ryde U. The MM/PBSA and MM/GBSA methods to estimate ligand-binding affinities. Expert Opin Drug Discov. 2015 May;10(5):449–61.

10. Kozakov D, Hall DR, Xia B, Porter KA, Padhorny D, Yueh C, Beglov D, Vajda S. The ClusPro web server for protein-protein docking. Nat Protoc. 2017 Feb;12(2):255-278.

11. Pagadala NS, Syed K, Tuszynski J. Software for molecular docking: a review. Biophys Rev. 2017 Apr;9(2):91-102.

12. Jana MK, Cappai R, Pham CL, Ciccotosto GD. Membrane-bound tetramer and trimer Aβ oligomeric species correlate with toxicity towards cultured neurons. J Neurochem. 2016 Feb;136(3):594-608

13. Kreutzer AG, Yoo S, Spencer RK, Nowick JS. Stabilization, Assembly, and Toxicity of Trimers Derived from Aβ. J Am Chem Soc. 2017 Jan 18;139(2):966-975

14. Nguyen HL, Linh HQ, Matteini P, La Penna G, Li MS. Emergence of Barrel Motif in amyloid-β Trimer: A Computational Study. *J. Phys. Chem. B.* 2020 Nov 25;124(47):10617-10631

15. Abedini A, Raleigh DP. A role for helical intermediates in amyloid formation by natively unfolded polypeptides? Phys Biol. 2009 Feb 10;6(1):015005.

16. Qi R, Luo Y, Ma B, Nussinov R, Wei G. Conformational distribution and α-helix to β-sheet transition of human amylin fragment dimer. Biomacromolecules. 2014 Jan 13;15(1):122-31.

17. Watkins AM, Arora PS. Anatomy of β-Strands at Protein–Protein Interfaces. ACS Chem Biol. 2014 Aug 15;9(8):1747–54.

18. Jochim AL, Arora PS. Systematic Analysis of Helical Protein Interfaces Reveals Targets for Synthetic Inhibitors. ACS Chem Biol. 2010 Oct 15;5(10):919–23.

19. Khramushin A, Marcu O, Alam N, Shimony O, Padhorny D, Brini E, *et al.* Modeling beta-sheet peptide-protein interactions: Rosetta FlexPepDock in CAPRI rounds 38-45. Proteins. 2020 Aug;88(8):1037–49.

20. Sun Y, Kakinen A, Xing Y, Pilkington EH, Davis TP, Ke PC, *et al.* Nucleation of β-rich oligomers and β-barrels in the early aggregation of human islet

amyloid polypeptide. Biochim Biophys Acta Mol Basis Dis. 2019 Feb 1;1865(2):434–44.

21. Qi R, Luo Y, Ma B, Nussinov R, Wei G. Conformational distribution and α-helix to β-sheet transition of human amylin fragment dimer. Biomacromolecules. 2014 Jan 13;15(1):122–31.

22. Nooren IMA, Thornton JM. Structural characterisation and functional significance of transient protein-protein interactions. J Mol Biol. 2003 Jan 31;325(5):991–1018.

23. Chaudhury S, Ripoll DR, Wallqvist A. Structure-based pKa prediction provides a thermodynamic basis for the role of histidines in pH-induced conformational transitions in dengue virus. Biochem Biophys Rep. 2015 Dec;4:375–85.

Chapter 5: Protonation-Dependent Effects of Zinc Binding on Aβ40 and Amylin Early-Stage Aggregation

5.1 Introduction

Alzheimer's disease (AD) is associated with the gradual accumulation of amyloid-β (Aβ) peptides produced from amyloid precursor protein (APP), and when the balance between Aβ production and clearance is disrupted, Aβ can self-associate into oligomers and ultimately deposit as plaques (1–3). As aggregation proceeds, intermolecular hydrogen bonding, hydrophobic packing, and electrostatic interactions stabilize these assemblies and can reduce their effective clearance, potentially contributing to accumulation (4–6). Amylin is relevant because it can co-assemble with Aβ40 and may modulate early aggregation behaviour by stabilizing mixed intermediates and altering β-structure formation during nucleation. A further layer of regulation is metal homeostasis: Zn(II) can influence amylin conformational behaviour (for example, by suppressing β-sheet conversion in secretory-granule-like environments), and perturbations in Zn(II) availability can therefore alter both amylin self-assembly and its cross-interaction with Aβ40. In earlier chapters of this thesis, peptide–peptide interactions were examined across increasing complexity and controlled pH ranges – from pH-driven conformational shifts in the Aβ40 N-terminus, where titratable residues dominate structural response, to full-length Aβ40 dimers and trimers with amylin across a physiologically relevant pH window (6 – 8) where protonation equilibria can meaningfully modulate interfacial electrostatics. In parallel, post-mortem studies of AD tissue report that amyloid deposits, including mixed Aβ40-amylin deposits, are often associated with elevated levels of transition metals, particularly Zn(II) (as well as Cu(II) and Fe(III)) (7–10), supporting the relevance of incorporating metal coordination into mechanistic models of early assembly. Accordingly, this chapter extends the established oligomer framework by introducing Zn(II) binding into Aβ40 and Aβ40–amylin early-stage assemblies and explicitly focusing on how Zn(II) alters protonation-dependent electrostatics and structural outcomes at the earliest stages of association. The central question is whether Zn(II) promotes persistent oligomer formation by anchoring or cross-linking coordination sites within the N-terminal binding region, while simultaneously redirecting the pathway toward, or away from, β-rich fibrillar order by reshaping charge distribution,

interfacial packing, and secondary-structure propensity under near-neutral pH conditions.

The data presented in previous chapter suggests that low concentrations of amylin binding accelerate Aβ aggregation by possibly positioning and stabilizing intermediate oligomers to accept other proteins more readily and reach a plateau at higher concentration. This behaviour is reminiscent of the modulatory effects observed for certain transition metals, in the context of this Chapter, Zn(II). Zinc ions are known to bind to the Aβ N-terminal domain (residues 1–16), altering its conformational ensemble and aggregation behaviour (11–13). Different experimental and theoretical studies have investigated Aβ-metal interactions and proposed the binding sites Asp1, His6, Glu11, His13, His14 (14–18). Parallel spectroscopic and computational investigations have also highlighted a coordination environment on amylin peptides for Zn(II) ions, on residue His18 and in some conditions, potentially also via the amino terminus (Lys1) (19,20).

Zn(II) coordination can alter Aβ conformational equilibria and inter-peptide contacts. In some contexts, Zn(II) binding is consistent with increased early association, potentially by stabilizing transient interfacial geometries, leading to greater propensity for aggregation at early-stage oligomerization(21,22). However, **Zn(II)** can also delay fibril formation, effectively redirecting the aggregation pathways towards non-fibrillar intermediates(23). Properties such as hydrogen bonding, structural packing and secondary structure content are affected by the Zn(II) interactions in addition to the folding of the peptide, which reflects the degree of stability leading to aggregation. Examining these changes through the previously established analysis parameters using CPPTRAJ provides a mechanistic link between metal-induced charge redistribution to the modulation of Aβ-amylin aggregation, clarifying how electrostatics interactions and local coordination geometry govern the balance between oligomer stabilization and fibril inhibition in both single- and dual-metal environments.

5.2 Methodology

The structures were selected based on the consistent metrics RMSD/Rg/SASA/Secstruct and a good ranking from the energetics but not so compact that the resulting structures would not be able to rearrange if needed when

Zn(II) was added. Taken from the equilibrated amylin and amyloid monomers clusters at pH 7, the structures were dimerized *via* docking through ClusPro. Post-ClusPro modifications like adding the disulphide bond between Cys2 and Cys7 residues on amylin, protonating the N-terminals of both peptides, capping the amylin C-terminus as an amide ($–CONH_2$) and addition of Zn(II) ions near titratable residues, were made to the selected highest balanced coefficient clusters before they were simulated. Only Aβ structures were homodimerized because previous experiments revealed that amylin homodimers only produced viable structures in explicit solvent models and thus required more computational cost than was efficient. These homodimers were simulated at pH 7 with fixed protonation states, focusing on validating the formation of these residues with unprotonated histidine residues, whereas heterodimers were simulated using CpHMD at pH 7 to enable residue-level protonation statistics (pK_a-related behaviour).

The results are reported in a comparative computational investigation into the effects of zinc binding on full-length dimeric Aβ against those absent of a metal centre across the same pH environment of 7. Although enhanced-sampling approaches can improve exploration of disordered ensembles, CpHMD was used here to maintain methodological consistency with earlier chapters and to capture protonation–conformation coupling. CpHMD allows protonation states to change in residues as they react to the environment throughout the simulation. It uses Monte Carlo calculations to determine protonation change, while also running cMD around those calculations. The monomer clusters which produced the most aggregation competent dimers in pH 7 were used for zinc(II) simulations and subsequent analysis in this chapter. Zn(II) ions were initially placed near N-terminal donor residues (based on literature coordination motifs) and coordination was monitored during simulation. This method may produce a selection bias, but choosing the highest population cluster also allows reduction of conformational noise.

All simulations were performed in AMBER22. Systems were built in LEaP (24) and minimized before running molecular dynamics using protonation states consistent with pH 7; three independent simulations were conducted for 100 ns with randomized initial velocities (ig = −1). Simulations used an implicit-solvent GBSA model under the NVT ensemble with SHAKE constraints at 300 K (25–32) and a 2 fs timestep, and an effectively unlimited non-bonded cut-off (cut = 999 Å) to avoid

truncation of van der Waals and electrostatic interactions. Because implicit-solvent electrostatics can over-stabilize charged contacts and metal–ligand interactions (i.e., “overbinding”) due to the absence of explicit water competition and ion screening, this stage is treated as a comparative screen under consistent conditions rather than an absolute binding-affinity assessment; Zn coordination was therefore validated using Zn–donor radial distribution functions (RDFs) and time-averaged coordination numbers, with trajectories checked for nonphysical overcoordination. The most stable and compact clusters from each homo- and heterodimer class (Tables 5.1–5.3) were then extended to 500 ns and analysed in CPPTRAJ using RMSD, radius of gyration (Rg), secondary structure, SASA, and RDF-derived coordination metrics to quantify how Zn binding modulates compactness, flexibility, and interfacial structure in Aβ and amylin assemblies.

A)

Combinations	0	1	2
asp1xrep2			
glu11xrep2			
his13xrep2			
his14xrep2			

B)

Combinations	0	1	2
asp1xcl0			
glu11xcl0			
his13xcl0			
his14xcl0			

C)

Combinations	0	1	2
asp1xcl0			
glu11xcl0			
his13xcl0			
his14xcl0			
asp1xcl1			
glu11xcl1			
his13xcl1			
his14xcl1			

Table 5.1 Simulation results of **A)** Aβ homodimer with one Zn^{2+} ion, **B)** Aβ-amylin heterodimer with one Zn^{2+} ion **C)** Aβ-amylin heterodimer with two Zn^{2+} ion in pH 7

environment after 100ns. Red indicates dimers that failed to remain together while green is reserved for those dimers that successfully remained together. The combinations naming convention denotes the location of the zinc on a residue of the amyloid first. The suffix '.0', '.1', and '.2' denotes replicate index (three independent runs). Cluster labels (cl0, cl1, cl2) indicate the monomer cluster used from prior CpHMD clustering.

5.3 Results and Discussion

5.3.1 Single Metal Homodimer Validation

Zinc Starting Placement	*RMSD (Å)*	*Rg (Å)*	*β - Sheet (%)*	*Helices (%)*	*Coordination #*	*SASA (Å²)*
Near Asp1	9.9 ± 1.2	14.1± 1.0	12	33	6	5959 ± 298
Near Glu11	8.9 ± 1.7	16.0 ± 1.2	1	39	6	6096 ± 327
Near HIS13	12.1 ± 3.8	14.8 ± 1.1	27	16	6	6138 ± 354
Near HIS14	12.4 ± 2.4	13.4 ± 0.7	4	35	6	6026 ± 318

Table 5.2 Statistical Results of RMSD (Å), Rg (Å), secondary structure content (%), solvent accessible surface area and zinc's coordination number in homodimers at pH 7.

There is an extensive body of prior research performed on amyloid-β homodimers and its chelation with Zn(II) ions. The present analysis was designed to focus primarily on its impact on structural dynamics, electrostatic behaviours and protonation states. The most stable amyloid β-40 homodimer structure is determined in the previous chapter as 3x3.10 and 3x4.10 complexes and considering the former complex had more successful simulations at 100 ns, its constituent monomers were chosen for simulation.

By comparing the Zn(II)-bound homodimers (Table 5.2) against the metal-free states (Tables 4.4.1–4.4.2), the results are consistent with Zn(II) altering interfacial packing and promoting a more heterogeneous ensemble. Across the Zn-start placements, the dimers show RMSD = 8.9–12.4 Å, Rg = 13.4–16.0 Å, and SASA = ~5960–6140 Å², consistent with compact-but-dynamic association states rather than a single rigid β-core arrangement. In contrast, several metal-free dimers reach lower RMSD and, in some cases, lower Rg values, suggesting tighter peptide–peptide packing when a metal centre does not compete with interchain contacts; however, SASA values

overlap between the two datasets, so differences in compactness should be interpreted comparatively.

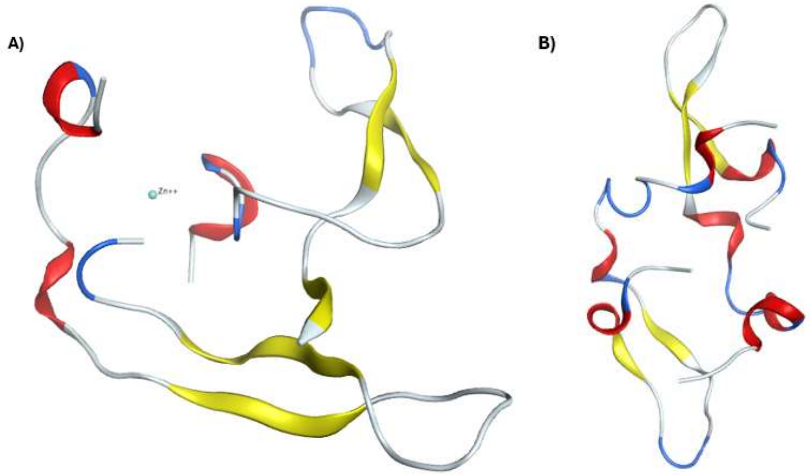

Figure 5.1 Secondary structure focused representation of complex 3x3.10 in a **A)** zinc-bound and **B)** zinc free state within MOE. Where yellow represents β-sheet content, the red represents the helices, the blue represents the turns/bends, and the white shows the coils content.

As expected, the homodimer complex 3x3.10 from the previous experiment had moderate content for both sheets and helices (14% and 25% respectively), a balance lost in its zinc-bound counterparts, which favours the helical structure (33-39%) far more than the sheets (1-12%) across all binding sites, with the single exception of the combination where zinc was placed near histidine at position 13. Although the structural parameters present a loose peptide structure (RMSD ~12 Å, Rg ~14 Å, SASA ~6138 Å²), a closer view at its secondary structure highlights a substantial β-sheet content (27%) and a decreased helicity (16%) – as shown in Figure 5.1A compared to its zinc-free counterpart in 5.1B, yielding a more ordered interfacial arrangement than other zinc-bound states. This may reflect a more favourable local coordination geometry when Zn(II) is placed near His13, which sits in the N-terminal metal-binding region alongside His6, His14, and nearby Asp/Glu donors. In this configuration, the average coordination number remains near six, consistent with a distorted octahedral-like first-shell environment, while peptide–peptide contacts can still support a higher β-sheet fraction than in the other Zn-start placements.

5.3.2 Single Metal Heterodimer

Combination	*RMSD (Å)*	*Rg (Å)*	β *- Sheet (%)*	*Helices (%)*	*Coord #*	*SASA (Å²)*
Asp1xcl0.0	8.0 ± 2.3	12.4 ± 0.5	10	22	7	5320 ± 299
Glu11xcl0.1	11.2 ± 2.0	12.8 ± 0.4	3	37	8	5563 ± 240
His13xcl0.0	9.3 ± 1.3	12.7 ± 0.4	9	38	6	5490 ± 279
His14xcl0.0	13.9 ± 2.1	13.5 ± 0.8	9	30	6	5660 ± 401

Table 5.3 Statistical Results of RMSD (Å), Rg (Å), secondary structure content (%), solvent accessible surface area and zinc's coordination number in heterodimers at pH 7.

	Protonated Residues				
Combinations	**HIP6**	**HIP13**	**HIP14**	**HIP59**	**Predicted Charge (lel)**
Asp1xcl0.0	0.01	0.32	0.05	0.05	-0.61
Glu11xcl0.1	0.09	0.00	0.01	0.04	-0.94
His13xcl0.0	0.13	0.02	0.01	0.15	-0.73
His14xcl0.0	0.04	0.02	0.03	0.27	-0.60

Table 5.4 Protonation and predicted charge data of the single zinc bound heterodimer at pH 7.

Patterns of disrupted peptide packing and reduced histidine protonation fractions associated with Zn(II) coordination are observed in the Aβ40–amylin heterodimers (Tables 5.3–5.4). The combinations are denoted as exemplified with Asp1xcl0.0; the zinc ion is near aspartate at position 1 of the heterodimer from highest cluster amyloid and amylin. The numerical values at the end denote which independent triplicate run was used. In the single-metal systems, the complexes become more compact in the presence of zinc yet remain comparably flexible to zinc-free dimers reported in Chapter 4 (Tables 4.6.2-4.6.3). Structurally, the zinc-bound heterodimers show a stronger bias toward helices over β-sheet (≈30% helix; ≈7% β-sheet) than the zinc-free counterparts, consistent with Zn^{2+} favouring non–β-rich conformations and aligning with its proposed role in suppressing amylin β-sheet conversion in secretory-granule-like environments. By contrast, zinc-free heterodimers display a more balanced secondary-structure profile (β-sheets ≈18%; helices ≈16%), highlighting the contribution of direct Aβ-amylin contacts when metal perturbation is absent.

The protonation data further indicate that Zn^{2+} perturbs the local electrostatic landscape in a site-dependent manner. For example, in Glu11-bound complexes, histidine protonation decreases with proximity to the metal (HIP6 = 0.09, HIP13 = 0.00, HIP14 = 0.01, HIP18 = 0.04), whereas the relatively high HIP13 value (0.32) in the Asp1-bound complex is consistent with that residue being more distal from the Zn^{2+} site. These shifts coincide with a more negative net charge overall (≈ −0.6 to −0.9), consistent with a more deprotonated and electrostatically diffuse ensemble. Mechanistically, Zn^{2+}–histidine coordination observed in Aβ40 homodimers may not translate directly to heterodimers because the mixed interface alters both geometry and donor availability: when histidines are protonated, the imidazole nitrogens are poorer ligands and less able to sustain strong Zn–His coordination. Consequently, Zn^{2+} is more likely to rely on carboxylate donors (Asp/Glu) and nearby backbone carbonyl oxygens, producing a looser and more heterogeneous coordination environment.

This behaviour is consistent with Zn^{2+} coordination flexibility at the Aβ N-terminus. Zn^{2+} commonly adopts a four-coordinate, tetrahedral-like arrangement when supported by a limited set of strong donors, but it can shift toward distorted higher coordination when additional oxygen donors enter the first coordination shell, particularly at solvent-exposed or crowded interfaces. In this study, Octahedral-like coordination can emerge when fewer strong imidazole donors are available (e.g., when histidines are protonated and thus poorer ligands), prompting Zn(II) to recruit additional oxygen donors (Asp/Glu carboxylates and backbone carbonyls) via transient ligand exchange for anchorage. Apparent coordination numbers approaching ~8 may also be inflated by bidentate carboxylate binding (two oxygens from a single Asp/Glu) and by transient ligand exchange. In such chelating cases, subsets of donors can adopt a more planar arrangement, making some snapshots appear more planar or square-pyramidal-like due to transient donor arrangements in Figure 5.2 even though Zn^{2+} does not intrinsically prefer strict square-planar geometry. Overall, these distorted, exchangeable coordination states reflect ligand availability and steric constraints rather than a single well-defined binding mode, and they are less effective at enforcing persistent β-sheet interfacial contacts.

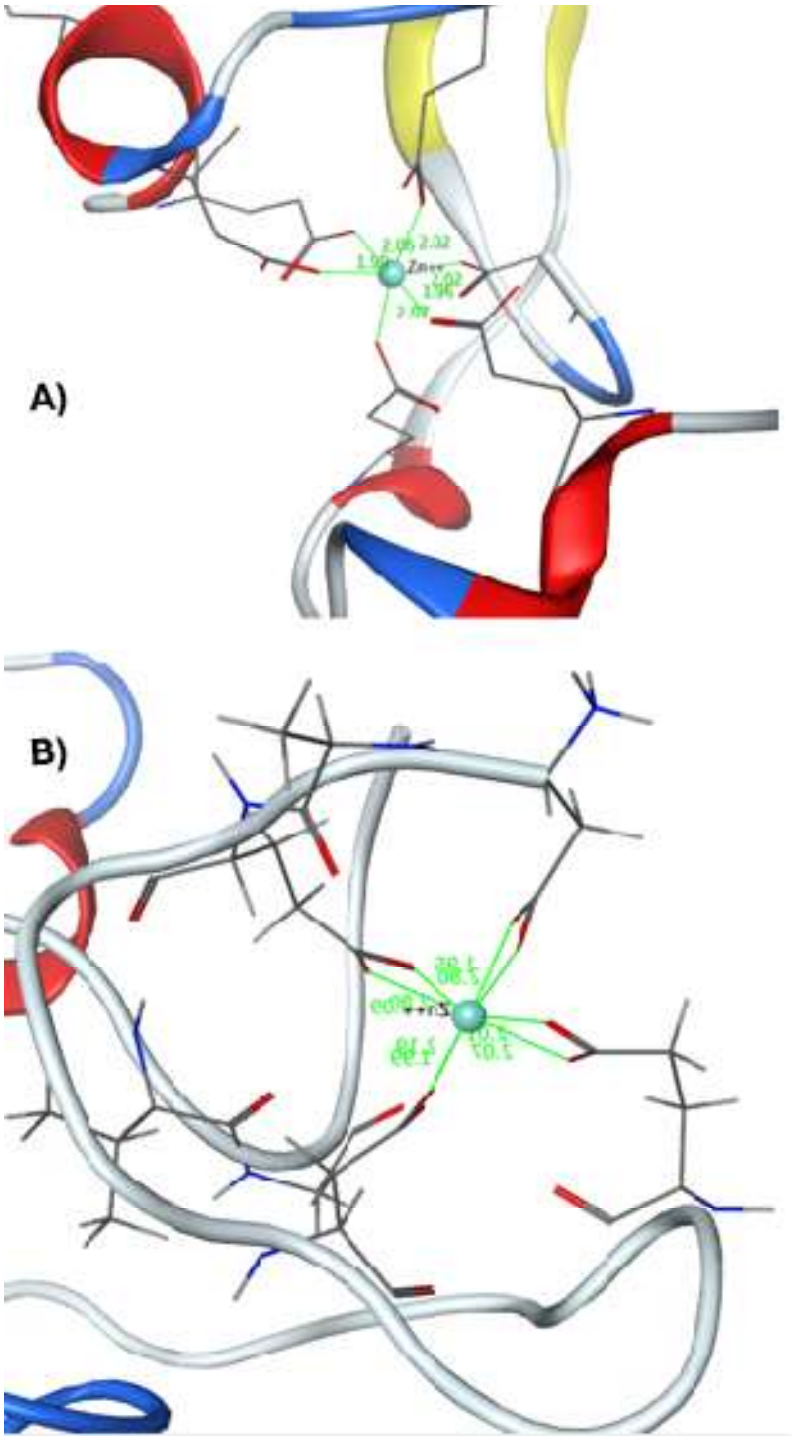

Figure 5.2. Displayed geometries for amylin and amyloid heterodimers with Zn^{2+} present near **A) Histidine** 13 (octahedral-like) and **B)** Glutamine 11 (tetrahedral/Planar-like) position through MOE.

5.3.3 Dual Metal Heterodimer

Table 5.5 illustrates the trade-off often observed between compactness (lower Rg/SASA) and conformational variability (RMSD), although the relationship is not strictly monotonic across all constructs. The larger range of combinations analysed for the dual-metal heterodimers provides a broader distribution to establish structural values. Overall, the dual-metal peptides are slightly more rigid and compact in comparison to the single (RMSD = 3.4–12.1 Å, Rg = 12.5–15.5 Å, SASA = 5277–6130 Å²). They also show a structural shift towards helices (~26–34%) and away from β-sheets (3–8%), which may be due to the influence of dual Zn(II) ions disrupting the local charge and further weakening inter-peptide β-contacts, consistent with zinc's known ability to modulate aggregation pathways by interfering with backbone hydrogen-bonding patterns.

This perturbation of the microenvironment is reflected in the low protonation values and comparatively lower complex charge, as noted in Table 5.6. Zinc-free heterodimers have broad and high protonation probabilities (0.20-0.90) indicative of a heterogeneous and positively polarized electrostatic environment in which many imidazole rings fluctuate between protonated and neutral states due to local pH and residue-residue interactions rather than any predisposition for metal coordination. Upon zinc introduction, however, the overall charge of the heterodimer system becomes slightly more negative on average (-0.72 vs. -0.89) driven by a modest but consistent histidine deprotonation across all sites (0–0.3). Dual Zinc coordination in heterodimer complexes behaves similarly to its single metal counterpart; both Zn(II) ions bind to few ligands with multi-atomic contacts with the same 3-4 residues, producing a higher coordination average without crowding the binding region. Both metal heterodimer systems (single and dual) follow the same trends; they produce lower protonation states and favour helical transitions over β-sheets, consistent with zinc's known tendency to disrupt aggregation-competent β-structures.

Combinations with Amyloid-amylin cluster 0	*RMSD (Å)*	*Rg (Å)*	*β - Sheet (%)*	*Helices (%)*	*Coord. #*		*SASA (Å²)*
					First Zinc	*Second Zinc*	
Asp1xcl0.1	7.4 ± 1.8	13.3 ± 0.5	2	27	7	7.5	5668 ± 279
Glu11xcl0.0	4.1 ± 0.6	12.88 ± 0.2	0.2	28	8	7	5371 ± 200
His13xcl0.0	7.3 ± 1.6	12.6 ± 0.3	5	26	8	7	5299 ± 199
His14xcl0.1	3.4 ± 0.3	12.5 ± 0.1	0.1	30	6	7	5277 ± 155
Asp1xcl1.0	10.1 ± 1.8	14.6 ± 1.0	13	32	7	7	5755 ± 248
Glu11xcl1.0	12.1 ± 1.6	15.5 ± 0.8	3	34	8	8	6130 ± 225
His13xcl1.2	9.0 ± 1.8	13.5 ± 0.6	10	32	7	7	5482 ± 285
His14xcl1.0	10.26 ± 0.8	15.2 ± 0.5	8	26	6	7	5717 ± 274

Table 5.5 Statistical Results of RMSD (Å), Rg (Å), secondary structure content (%), solvent accessible surface area and zinc's coordination # in dual metal heterodimers at pH 7.

	Protonated Residues				
	HIP6	**HIP13**	**HIP14**	**HIP59**	**Predicted Charge (lel)**
Asp1xcl0.1	0.010	0.017	0.014	0.008	-0.95
Glu11xcl0.0	0.003	0.013	0.016	0.009	-0.96
His13xcl0.0	0.025	0.029	0.031	0.005	-0.91
His14xcl0.1	0.015	0.01	0.013	0.004	-0.96
Asp1xcl1.0	0.12	0.36	0.011	0	-0.51
Glu11xcl1.0	0.029	0.013	0.018	0.009	-0.93
His13xcl1.2	0.024	0.053	0.025	0	-0.90
His14xcl1.0	0.017	0.007	0.015	0	-0.96

Table 5.6 Protonation and predicted charge data of dual zinc bound heterodimers at pH 7.

5.4 Conclusion

An extension of the dimeric studies in chapter four, this chapter focuses on evaluating the structural and protonation effects of Zn(II) coordination within Aβ40-

Aβ40and Aβ40–amylin systems. Previous literature establishes zinc as a modulator in amyloid aggregation; the present work validates and extends this experiment to focus on protonation and charge distribution across the single and dual metal heterodimers.

Simulation of zinc–amyloid homodimer in implicit-solvent models confirmed the accuracy of the systems in reproducing established analytical parameters for Aβ–Zn(II) coordination behaviour within the N-terminal region (across residues like Asp1, His6, Glu11, His13, His14). The configuration with zinc near the His13 residue demonstrated near-native compactness, preserved β-content, which is consistent with chemically plausible Zn(II) coordination in this configuration. When zinc was introduced into the Aβ–amylin heterodimer, it produced a similar compact complex but was more flexible, steering its structure toward helical arrangements and away from β-sheets. When two zinc ions were bound – one to Aβ's N-terminal site and the other to amylin's His18 – the resulting complexes became more compact and moderately flexible, dominated by helices rather than β-sheets. This pattern reflected how the shared electronic charge between two Zn^{2+} sites redistribute the electrostatic landscape by introducing additional localized positive centres. These interactions also displayed how these complexes' structural conformations and electrostatic interactions rely on the localization of the metal. These patterns make clear that zinc's role is not a simple matter of promoting or blocking aggregation; instead, it disrupts the fibril-like order of peptide-peptide contacts with metal-mediated, disordered interactions as they begin to cluster. This keeps the chains together (producing more successful dimers in simulations), but they lack the β-rich, fibril-like states seen in zinc-free systems. With the homodimer simulations validating the zinc parameters and the heterodimer systems extending them in protonated states, our study offers a new perspective on how weaker coordination interactions can still produce compact and flexible Aβ–amylin assemblies under physiological conditions.

References

1. Chen G, Xu Hai, Yan Y, Zhou Y, Jiang Y, Melcher K, *et al. Amyloid* beta: structure, biology and structure-based therapeutic development. Acta Pharmacol Sin. 2017 Sept;38(9):1205–35.

2. Masters CL, Simms G, Weinman NA, Multhaup G, McDonald BL, Beyreuther K. Amyloid plaque core protein in Alzheimer disease and Down syndrome. Proc Natl Acad Sci U S A. 1985 June;82(12):4245–9.

3. Glenner GG, Wong CW. Alzheimer's disease: initial report of the purification and characterization of a novel cerebrovascular amyloid protein. Biochem Biophys Res Commun. 1984 May 16;120(3):885–90.

4. Nasica-Labouze J, Nguyen PH, Sterpone F, Berthoumieu O, Buchete NV, Coté S, *et al. Amyloid* β Protein and Alzheimer's Disease: When Computer Simulations Complement Experimental Studies. Chem Rev. 2015 May 13;115(9):3518–63.

5. Klein WL. Abeta toxicity in Alzheimer's disease: globular oligomers (ADDLs) as new vaccine and drug targets. Neurochem Int. 2002 Nov;41(5):345–52.

6. Selkoe DJ. Soluble oligomers of the amyloid β-protein impair synaptic plasticity and behavior. Behav Brain Res. 2008 Sept 1;192(1):106–13.

7. Alies B, Eury H, Bijani C, Rechignat L, Faller P, Hureau C. pH-Dependent Cu (II) Coordination to amyloid-β Peptide: Impact of Sequence Alterations, Including the H6R and D7N Familial Mutations. Inorg Chem. 2011 Nov 7;50(21):11192–201.

8. Alghrably M, Czaban I, Jaremko Ł, Jaremko M. Interaction of amylin species with transition metals and membranes. J Inorg Biochem. 2019 Feb; 191:69–76.

9. Rana M, Sharma AK. Cu and Zn interactions with Aβ peptides: consequence of coordination on aggregation and formation of neurotoxic soluble Aβ oligomers. Met Integr Biometal Sci. 2019 Jan 23;11(1):64–84.

10. Atrián-Blasco E, Gonzalez P, Santoro A, Alies B, Faller P, Hureau C. Cu and Zn coordination to amyloid peptides: From fascinating chemistry to debated pathological relevance. Coord Chem Rev. 2018 Sept 15; 371:38–55.

11. Pan L, Patterson JC. Molecular Dynamics Study of Zn(Aβ) and Zn(Aβ)2. PLOS ONE. 2013 Sept 27;8(9): e70681.

12. Zirah S, Kozin SA, Mazur AK, Blond A, Cheminant M, Ségalas-Milazzo I, *et al.* Structural changes of region 1-16 of the Alzheimer disease amyloid beta-peptide upon zinc binding and in vitro aging. J Biol Chem. 2006 Jan 27;281(4):2151–61.

13. Alies B, Conte-Daban A, Sayen S, Collin F, Kieffer I, Guillon E, *et al.* Zinc (II) Binding Site to the amyloid-β Peptide: Insights from Spectroscopic Studies with a Wide Series of Modified Peptides. Inorg Chem. 2016 Oct 17;55(20):10499–509.

14. Wineman-Fisher V, Miller Y. Insight into a New Binding Site of Zinc Ions in Fibrillar amylin. ACS Chem Neurosci. 2017 Sept 20;8(9):2078–87.

15. Rezaei-Ghaleh N, Giller K, Becker S, Zweckstetter M. Effect of zinc binding on β-amyloid structure and dynamics: implications for Aβ aggregation. Biophys J. 2011 Sept 7;101(5):1202–11.

16. Cheignon C, Tomas M, Bonnefont-Rousselot D, Faller P, Hureau C, Collin F. Oxidative stress and the amyloid beta peptide in Alzheimer's disease. Redox Biol. 2017 Oct 18;14:450–64.

17. Miller Y, Ma B, Nussinov R. Zinc ions promote Alzheimer Aβ aggregation via population shift of polymorphic states. Proc Natl Acad Sci. 2010 May 25;107(21):9490–5.

18. Watt NT, Whitehouse IJ, Hooper NM. The Role of Zinc in Alzheimer′s Disease. Int J Alzheimer's Dis. 2011;2011(1):971021.

19. Salamekh S, Brender JR, Hyung SJ, Nanga RPR, Vivekanandan S, Ruotolo BT, *et al.* A two-site mechanism for the inhibition of IAPP amyloidogenesis by zinc. J Mol Biol. 2011 July 8;410(2):294–306.

20. Rowińska-Żyrek M. Coordination of Zn2+ and Cu2+ to the membrane disrupting fragment of amylin. Dalton Trans. 2016 May 10;45(19):8099–106.

21. Lee MC, Yu WC, Shih YH, Chen CY, Guo ZH, Huang SJ, *et al.* Zinc ion rapidly induces toxic, off-pathway amyloid-β oligomers distinct from amyloid-β derived diffusible ligands in Alzheimer's disease. Sci Rep. 2018 Mar 19;8(1):4772.

22. Mannini B, Habchi J, Chia S, Ruggeri FS, Perni M, Knowles TPJ, *et al.* Stabilization and Characterization of Cytotoxic Aβ40 Oligomers Isolated from an Aggregation Reaction in the Presence of Zinc Ions. ACS Chem Neurosci. 2018 Dec 19;9(12):2959–71.

23. Milardi D, Gazit E, Radford SE, Xu Y, Gallardo RU, Caflisch A, *et al.* Proteostasis of Islet amyloid Polypeptide: A Molecular Perspective of Risk Factors and Protective Strategies for Type II Diabetes. Chem Rev. 2021 Feb 10;121(3):1845–93.

24. Maier JA, Martinez C, Kasavajhala K, Wickstrom L, Hauser KE, Simmerling C. ACS Publications. American Chemical Society; 2015 [cited 2025 Sept 27]. ff14SB: Improving the Accuracy of Protein Side Chain and Backbone Parameters from ff99SB. Available from: https://pubs.acs.org/doi/full/10.1021/acs.jctc.5b00255

25. Case DA, Aktulga HM, Belfon K, Cerutti DS, Cisneros GA, Cruzeiro VWD, *et al.* AmberTools. J Chem Inf Model. 2023 Oct 23;63(20):6183–91.

26. Case DA, Cheatham III TE, Darden T, Gohlke H, Luo R, Merz Jr. KM, *et al.* The Amber biomolecular simulation programs. J Comput Chem. 2005 Dec 1;26(16):1668–88.

27. Lang EJM, Baker EG, Woolfson DN, Mulholland AJ. Generalized Born Implicit Solvent Models Do Not Reproduce Secondary Structures of De Novo Designed Glu/Lys Peptides. J Chem Theory Comput. 2022 July 12;18(7):4070–6.

28. Onufriev AV, Case DA. Generalized Born Implicit Solvent Models for Biomolecules. Annu Rev Biophys. 2019 May 6;48:275–96.

29. Paravastu AK, Leapman RD, Yau WM, Tycko R. Molecular structural basis for polymorphism in Alzheimer's beta-amyloid fibrils. Proc Natl Acad Sci U S A. 2008 Nov 25;105(47):18349–54.

30. Okur A, Wickstrom L, Layten M, Geney R, Song K, Hornak V, *et al.* Improved Efficiency of Replica Exchange Simulations through Use of a Hybrid Explicit/Implicit Solvation Model. J Chem Theory Comput. 2006 Mar 1;2(2):420–33.

31. Cornell WD, Cieplak P, Bayly CI, Gould IR, Merz KM, Ferguson DM, *et al.* A Second-Generation Force Field for the Simulation of Proteins, Nucleic Acids, and Organic Molecules. J Am Chem Soc. 1995 May 1;117(19):5179–97.

32. Rappe AK, Casewit CJ, Colwell KS, III WAG, Skiff WM. ACS Publications. American Chemical Society; 2002 [cited 2025 Sept 27]. UFF, a full periodic table force field for molecular mechanics and molecular dynamics simulations. Available from: https://pubs.acs.org/doi/abs/10.1021/ja00051a040

Chapter 6: Conclusion and Future Research

The work presented in this thesis investigates how amylin co-assembly and Zn(II) coordination influence the structure and dynamics of Aβ40, a peptide centrally implicated in Alzheimer's disease aggregation and plaque formation. Although these peptides and their interactions have been extensively studied, integrating constant-pH molecular dynamics to examine how electrostatics, protonation equilibria, directionality, and metal coordination shape mixed early assemblies introduces practical and conceptual challenges, in part because histidine protonation near physiological pH can amplify repulsive interactions and broaden the conformational landscape. By simulating these systems over hundreds of nanoseconds across monomeric, dimeric, and trimeric states under multiple pH conditions, this thesis shows that early nucleation-stage behaviour is dictated by a finely balanced interplay of local charge, protonation state, interfacial complementarity, and transition-metal effects, rather than peptide sequence alone. A distinctive feature of this thesis is the coherent pipeline used to build this mechanistic picture—from single peptides to dimers and then trimers—so that pH effects are mapped first, heterodimers are evaluated against homodimer baselines, and Zn(II) is then introduced on top of that pH-defined landscape to determine how coordination chemistry reshapes the same early interfaces. A key interpretive point carried through this pipeline is that persistent association ("staying together") does not necessarily imply formation of a β-sheet-rich fibrillar nucleus: early assemblies can remain compact and long-lived while still occupying mixed or heterogeneous secondary-structure states.

The initial experiments were performed on a truncated Aβ16, which is computationally inexpensive and can help save calculation time for modelling similar systems in constant pH with the full-length Aβ40. The Aβ16 fragment was first modelled to validate the feasibility and consistency of the implicit-solvent CpHMD over the explicit solvent. Then it was simulated in a wide range of environments (pH 1-10) using AMBER ff10 forcefield. Due to the time constraints, our methods were limited to only one previously validated calibration strategy throughout the research phase, otherwise more computationally intensive alternatives (e.g., QM/MM or semiempirical QM for metal-binding motifs, and enhanced sampling such as replica-exchange or metadynamics) could be tested to cross-validate key conclusions on efficiency versus accuracy.

The interplay of computational costs vs. accuracy was also important to consider wherever binding free energies were analysed. While the rigorous MM/PBSA is more accurate, MM/GBSA trades some solvation-model fidelity for computational speed relative to MM/PBSA. Accordingly, binding free energies were interpreted comparatively (across systems and conditions) rather than as absolute affinities - trading PBSA's accuracy for computational speed. Therefore, we interpret energies comparatively rather than as absolute affinities. To mitigate the loss of accuracy we compared the averages of binding free energies across various snapshot frames taken from converged segments of the trajectories and took forward the parameters that most consistently resembled the PBSA results across 10 different trajectories.

Furthermore, considering our research was in collaboration with Dr. Hureau's experimental studies we set our temperatures to a more experimentally replicable scale at 300 K using the Langevin thermostat, after a comparative study with the physiological 310 K setting revealed insignificant difference in results. Langevin dynamics was used for temperature control to match earlier chapters and to stabilize sampling for flexible peptides. Longer trajectories were used to improve time-averaged estimates and reduce sensitivity to short-timescale fluctuations. Testing the truncated peptides under these conditions nonetheless allowed us to calibrate analysis and solvent choices before scaling to Aβ40.

Later, full-length Aβ40 peptides alongside the newly constructed amylin monomer were simulated in narrower pH ranges with the previous simulation parameters being carried forward. These revealed that near-neutral environments (pH 6–8) consistently favoured compactness, reduced structural fluctuation, and more organized secondary structure in Aβ40, consistent with the stabilizing effect of partially protonated histidine residues on intra-chain hydrogen bonding. In contrast, amylin remained markedly more conformationally flexible across the same pH interval, displaying broader RMSD distributions, larger Rg values, and a persistent bias toward helical and turn-rich motifs as opposed to the Aβ40 favoured β-sheet formation. Despite these differences, both peptides retained signatures of intrinsic disorder, dominated by coil and bend structures. Having established the conformational behaviour of each peptide individually allowed us to better determine a pattern of behaviour amongst higher order complexes like dimers and trimers.

In Chapter 4, hundreds of amyloid-led or amylin-led homo/hetero dimers and trimers were simulated across pH 6, 7, 7.4 and pH 8 using ClusPro and the previously established CpHMD parameters. While ClusPro provided the challenge of sometimes producing occasional non-physical docking poses (e.g., severe steric overlaps or unrealistic side-chain interpenetration), running the larger sample sizes allowed us to treat those few examples without significance to the larger resulting dataset. Another challenge was meeting the charge and water requirements of consistently unsuccessful implicit solvated amylin homodimers set in pH 6 and 8. While pH 7 and 7.4 produced viable structures, the homodimers at the fringes of the pH range required explicit solvent as it added the counterions required to keep the homodimers stable. Due to time-constraints and computational costs of running several dozens of long simulations in explicit solvent, the data for those simulations were not addressed.

The successful simulations revealed that organisational patterns within dimeric complexes depend strongly on which peptide acts as receptor versus ligand: Aβ-driven assemblies consistently formed more β-enriched and compact structures, whereas amylin-led configurations produced semi-ordered but more flexible interfaces dominated by helical and turn-rich motifs. The differing outcomes between reciprocal assemblies highlighted the importance of polarity and protonation balance in shaping interface stability and aggregation propensity. Furthermore, mixed Aβ–amylin dimers supported a cooperative but self-limiting mechanism, in which amylin's intrinsic flexibility modulates Aβ's β-structuring tendencies without necessarily locking the system into uncontrolled fibril-like growth. Importantly, these results also emphasise that "staying together" is not equivalent to forming a β-sheet-rich fibrillar nucleus: many stable assemblies persist in mixed or heterogeneous conformations that may represent pre-nucleation intermediates rather than committed β-core structures.

In contrast, trimeric assemblies in pH 7 or 7.4 showcase that this early-stage flexibility does not persist indefinitely. Despite increasing system size to 117 residues, trimers exhibited lower SASA per residue, consistent with increased compactness and stronger interfacial cooperativity than dimers. The trimers suggested that β-enrichment becomes less sensitive to initial orientation than in dimers, although orientation still influenced overall compactness and solvent

exposure; while amylin-led trimers create tighter and rigid conformations and the amyloid-led trimers produce larger and more extended structures, both exhibited similarly β-sheet favoured organisations at their core regions.

Together, these results support a coherent nucleation pathway: dimeric forms behave as structurally plastic intermediates shaped by protonation equilibria and electrostatic complementarity, whereas trimers represent the first stage at which persistent, aggregation-competent β-architectures begin to emerge. This progression aligns with literature models in which Aβ–amylin co-aggregation is cooperative at early stages but becomes increasingly ordered and fibril-prone as oligomers grow, capturing the mechanistic transition from flexible precursors to structured nuclei. However, while long simulations are useful for mapping the conformational space accessible to individual poses, they are less effective at validating reproducibility because a single long trajectory can remain trapped in a “lucky” energy basin. The best way to validate pH-influenced behaviours would therefore be independent replicates, as used in Chapter 3: once three simulations converge on a shared ensemble, interface persistence analysis across successful poses can identify which residue contacts consistently mediate binding and how protonation balance stabilizes (or destabilizes) those contacts. To expand this work quantitatively, enhanced sampling (e.g., metadynamics or replica-exchange) could then be applied selectively to the most relevant interfaces identified here, rather than broadly across the full docking landscape.

In Chapter 5, the investigation was extended to include the coordination of Zn(II) with both peptides, first validating its behaviour through reproductions of experimentally supported coordination preferences in non-protonated homomeric Aβ40 conformations and then analysing residue-level protonation behaviour (CpHMD protonation fractions and inferred pK_a shifts) in heteromeric Aβ40–amylin assemblies. The approach in Chapter 5 was deliberately narrow in scope owing to a greater literature-inspired confidence in Zn(II) binding to the amyloid-amylin oligomers than other bioavailable metals (e.g. Cu^{2+}, $Fe^{2+/3+}$, Co^{3+}) metals that may require more specialised treatment (e.g., redox chemistry, multiple spin states, or stronger polarization effects), the computational and temporal costs of switching from classical force fields and familiar constant-pH MD methods to the higher-level QM/MM treatments, and the desire to preserve direct comparability with the

protonation-governed dimer systems established in Chapter 4. We wanted to remain within the practical limits of sampling, computational cost, and methodological complexity.

For homomeric assemblies, the His13-adjacent configuration preserved native-like compactness and β-structure. Introducing Zn(II) into heteromeric structures prepared for protonation analysis (CpHMD statistics; cphstats) revealed additional complexity, as local deprotonation and charge redistribution altered the conformational pathways accessible to these peptides. More broadly, Zn(II) binding reshapes local electrostatics and competes with interpeptide contacts; this often stabilizes overall association while potentially disrupting the interchain registry needed for persistent β-sheet alignment. Accordingly, Zn-bound heteromeric assemblies shifted toward more helical, flexible conformations, an effect that was amplified when two Zn(II) ions were present—one positioned near Aβ40 His13/14 and the other near amylin His18. Consistent with this, placing Zn(II) across a wider set of candidate residues at pH 7 produced complexes that were generally more compact yet still moderately flexible, and that diverged from the more β-enriched trajectories observed for the corresponding metal-free dimers.

Overall, these results support the interpretation that Zn(II) behaves as a subtle chemical modulator that may reroutes the early nucleation pathways for Aβ-amylin co-aggregation by altering protonation equilibria, coordination geometry, and the balance between helical and β-structural tendencies. Future studies should prioritise replicate-based reproducibility as the main validation step for both pH- and Zn-modulated behaviours. Once reproducible ensembles are established, the next quantitative step is to probe the coordination interface with higher-level methods—such as hybrid DFT or QM/MM focused on representative binding motifs—because classical force fields cannot fully capture charge transfer and polarization effects central to metal coordination chemistry. In parallel, explicit-solvent simulations should be used for broader conformational exploration and for systems that are unreliable in implicit solvent (notably amylin homodimers), using specialized metal and ion parameters where required. Zinc behaviour can also be broadened by pursuing mix-metal studies (e.g. Zn(II)/Cu(II) or Zn(II)/Fe(II)), incorporating higher-level electronic structure methods (i.e. LFMM) for key coordination motifs, to capture with greater accuracy; coordination geometry changes, charge-transfer contributions

etc. Finally, integrating experimental observables (e.g., NMR, EPR, SAXS, cryo-EM restraints) would further constrain the models and strengthen the bridge between simulation-derived mechanisms and observable pathology in Alzheimer's disease.

7 APPENDICES

Aβ-40	**Amylin**
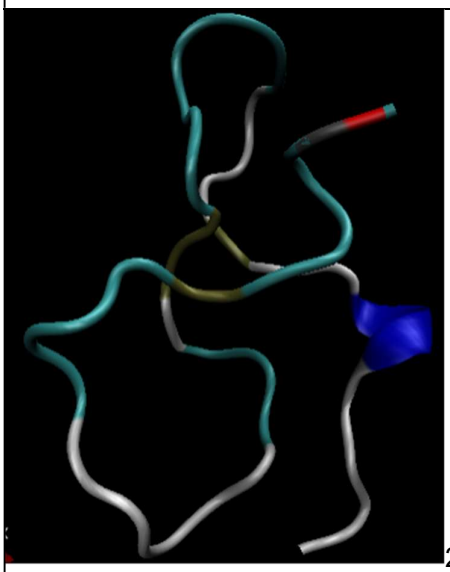 20%	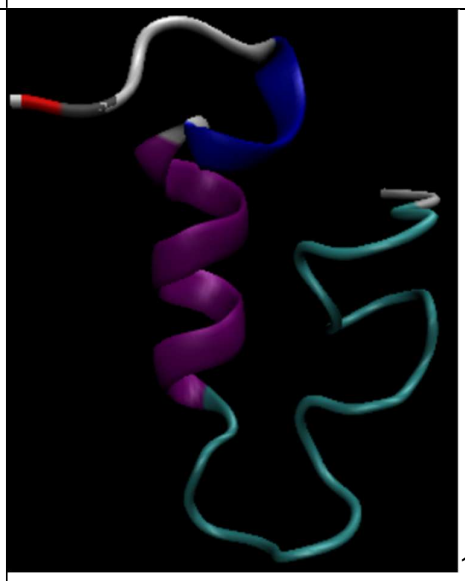 18%
pH 5	pH 5
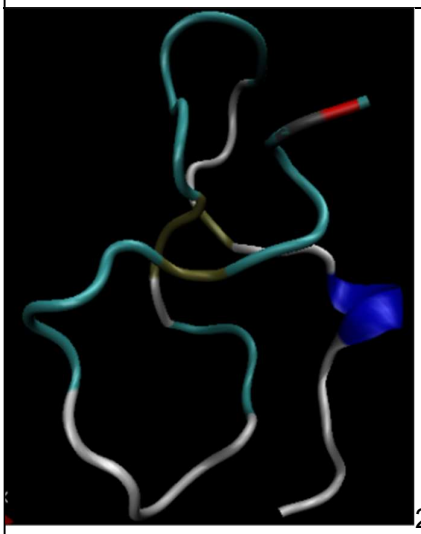 25%	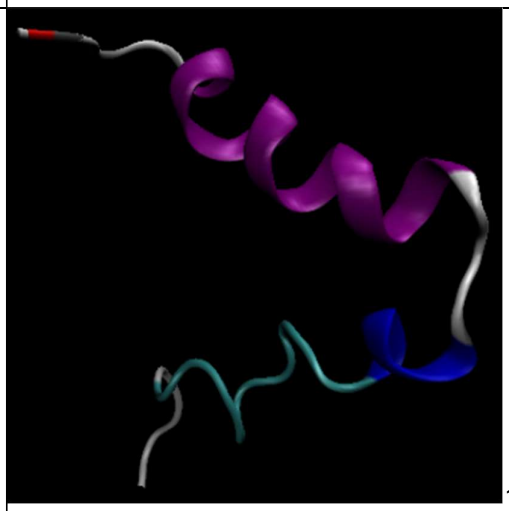 14%
pH 6	pH 6

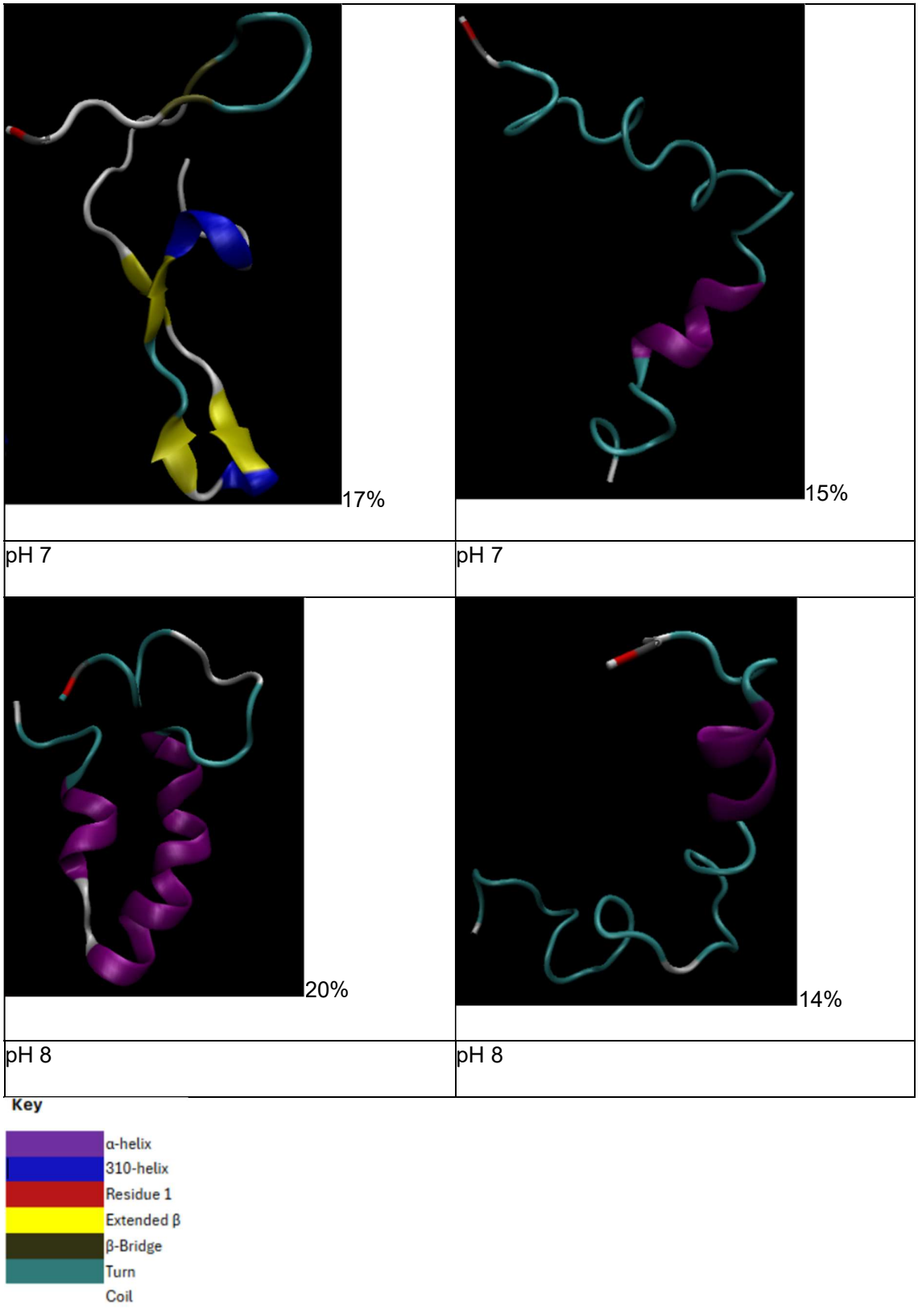

Figure A1. Representative structures of highest populated clusters from the average of all over 300,000 frames across 3 parallel runs at comparable pH 5-8 range. The most

populated cluster in all trajectories was found in pH 6 at 25% for Aβ40 as noted in Figure 4. The highest-populated amylin cluster was found at 18% in pH5. Amylin also had the least populated percentage cluster at pH 6 and 8 each at 14%. Amylin clusters have a smaller population at each pH compared to Aβ40 indicating that Aβ40 simulations yield more similarly structured conformations.